THE UNIVERSITY OF CALGARY

Modelling the Deformation of the Alberta Foreland Basin Using Finite Elements

by

Richard R. Spiteri

A THESIS
SUBMITTED TO THE FACULTY OF GRADUATE STUDIES
IN PARTIAL FULFILLMENT OF THE REQUIREMENTS FOR THE
DEGREE OF MASTER OF SCIENCE

Department of Geology and Geophysics

CALGARY, ALBERTA
AUGUST, 1991

ISBN 0-315-71167-1

THE UNIVERSITY OF CALGARY
FACULTY OF GRADUATE STUDIES

The undersigned certify that they have read, and recommend to the Faculty of Graduate Studies for acceptance, a thesis entitled "Modelling the Deformation of the Alberta Foreland Basin Using Finite Elements" submitted by Richard R. Spiteri in partial fulfillment of the requirements for the degree of Master of Science.

Supervisor, Dr. P. P. Wu,
Department of Geology and Geophysics

Dr. R. J. Brown,
Department of Geology and Geophysics

Dr. L. Hills,
Department of Geology and Geophysics

Dr. M. Epstein,
Department of Mechanical Engineering

Date: 11th Sept., 1991

Abstract

The finite element method was shown to be applicable to the investigation of Earth deformation problems. The main advantages of this technique are that thin-plate theory does not have to be assumed and that lateral variations in the Earth's properties can easily be taken into account.

The characteristic pattern of foreland basins due to advancing thrust loads was then analyzed for the Alberta Foreland Basin using the finite element method. The effects of a viscoelastic lithosphere resting over a relaxed mantle and supported purely by buoyancy was considered for this area. By applying a load history $L(x,t)$ for the advancing thrust sheets of the Rocky Mountain Fold and Thrust Belt, the stratigraphy of the adjacent foreland basin was related to the structure through the deformation of the lithosphere. Both uniformly thick models and eastward thickening models were considered. The preferred model was found to have an eastward thickening lithosphere with a thickness of >200 km beneath the craton which supports the tectosphere model proposed by T.H. Jordan. The model also correctly predicts the absence of any appreciable present-day peripheral bulge within Alberta and Saskatchewan which is usually associated with other (uniform) flexural models. This is consistent with current observations of the stratigraphy which do not support the existence of a prominent forebulge within the basin.

One implication of this work has been to support a new and profound understanding of the dynamics of plate-plate interaction for continental tectonics. A thick-lithosphere model has significant implications in the study of plate-plate interaction and crustal

dynamics. In order to have continental lithospheres with cold deep roots extending to depths greater than 200 km, it was necessary to postulate a model consisting of continental plates actually *sitting* on the denser mantle. The oceanic lithosphere was still envisaged as a rigid plate floating on a fluid asthenosphere. The cold roots of the continents, however, are dragged through the more viscous lower mantle and are consequently impeded from moving at the same plate velocities observed for their oceanic counterparts. This hypothesis is further supported by observations of three-dimensional inversion (tomography) of surface-wave data by J.H. Woodhouse and A.M. Dziewonski.

Résumé

La méthode des éléments finis se révèle particulièrement adaptée à la résolution des problèmes de déformation de la Terre. Les principaux avantages de cette technique sont d'une part son indépendance par rapport à la théorie de la déformation d'une plaque mince et d'autre part la prise en compte aisé des variations latérales des propriétés de la Terre.

Ainsi, l'évolution caractéristique d'un bassin d'avant-pays créé sous l'effet du poids de nappes chevauchantes qui s'avancent a été analysée dans le cas du Bassin d'Avant-pays de l'Alberta à l'aide de la méthode des éléments finis.

Le cas d'une lithosphère viscoélastique reposant sur un manteau fluide et supportée purement par flottabilité a été retenu pour cette région. En appliquant une histoire de charge $L(x,t)$ pourles nappes charriées formant la ceinture de *Plis et Chevauchements des Montagnes Rocheuses* , la stratigraphie dubassin d'avant-pays adjacent est reliée à l'activité structurale à travers la déformation de la lithosphère.

Des modèles à lithosphère d'épaisseur constante ou bien à épaississement vers l'Est ont été testés. Le modèle retenu se trouve avoir une lithospère s'épaississant vers l'Est avec une épaisseur supérieure à 200 km sous le craton, choix qui s'accorde avec le modéle de tectosphère proposé par T. H. Jordan.

En outre, le modèle a prédit correctement l'absence d'un bombement pèriphérique actuel sensible en Alberta et en Saskatchewan qui habituellement est associé avec les modèles flexuraux uniformes. De plus, ce résultat est cohérent avec l'analyse

stratigraphique qui dément l'existence d'un tel bombement dans les bassin.

Ce travail entre autres conséquences, propose une vision nouvelle et une compréhension plus profonde de la dynamique des interactions plaque-plaque et de leur influence sur la tectonique intracontinentale. En effet un modèle à lithosphère épaisse a d'importantes implications sur la dynamique crustale et les interactions entres plaques. Afin de représenter des lithosphères continentales possédant des racines froides et profondes jusqu'à plus de 200 km, il faut postuler un modèle à où les plaques continentales sont littéralement *échouées* sur un manteau inférieur plus dense. La lithosphère océanique est cependant toujours considérée comme plaque rigide flottant sur le manteau supérieur, l'asthenosphère fluide. En revanche, les froides racines des plaques continentales labourent le manteau inférieur plus visqueux qui, par conséquent les empèche de se déplacer à la même vitesse observée chez leur homologues océaniques.

Cette hypothése est renforcée par des observations de données d'inversion tri-dimensionelle (tomographie) éstablies à partir des ondes de surfaces par J.H. Woodhouse et A.M. Dziewonski.

traduit par M. Villéger.

Acknowledgements

I would like to give my thanks to my supervisor, Dr. P. Wu, for introducing me to geodynamics and for his patience and understanding throughout my Master's program. Without his insight and guidance this work would not have been possible.

Mary-Ann was always there to offer support without pressure throughout my studies and was understanding on those nights when I came home late. Young Michael cheerfully sat on my lap some evenings as I typed portions of this thesis. Stéphane Labonté and Wayne Geis were true companions during those stressful times. Robert Osika was politely persistent in reminding me to "do my thesis".

Nixtieq nizzik ħajr lil ommi u lil missieri li għamlu ħafna għalija biex inkun nista inkompli l-iskola... dejjem kienu hemm meta kelli bzonn xi ħaga. Inroġħod il-ħajr lil Alla talli taghni l-ħila u s-saħħa biex nagħmel xogħol bħal dan!!

Financial assistance from Dr. P. Wu and the University of Calgary is gratefully acknowledged. Technical support for the CYBER 205 supercomputer was provided by Prem Domingo from Super Computing Services.

Table of Contents

List of Tables

List of Figures

"Neither you nor anyone else knows with any certainty what is going on inside the Earth"

Jules Verne (1864),
Journey to the Centre of the Earth

1. Deformation of the Earth

Geodynamics is the study of global Earth movements and the forces driving them. The science aims at explaining present-day surface features which are presumably caused by internal forces. This thesis focuses on an aspect of geodynamics where the forces are due to externally applied surface loads.

The Earth is continuously being deformed by surface loads. Some examples of these loads include: those caused by pluvial lakes, glaciers and continental ice sheets which are all related to major climatic changes; tidal loading and oceanic islands; and sedimentary basin fills which are related to adjacent orogenic events. Our main concern was the latter type of surface load and the Alberta Foreland Basin will be considered in detail.

One important aspect in the modelling of these deformations is what constitutes an appropriate model for the rheology of the planetary interior. The Earth is known to respond elastically to short period loads but it also has an anelastic (*i.e.* creep) response. Direct evidence for anelastic behaviour is abundant for both short characteristic timescales (dispersion of body wave velocities, spatial attenuation of surface waves, seismic attenuation in seismic field measurements) as well as longer characteristic timescales (post-glacial rebound, secular deformation of the Earth, crustal bending). Another manifestation of creep processes in the mantle is plate tectonics. This process could not occur unless it was possible for mantle material to deform continuously in a fluid-like fashion over long periods of time. Although there has been considerable debate as to what constitutes a sensible working model of viscoelastic behaviour (Peltier *et al.*, 1981), the usefulness of linear viscoelastic models for surface loading problems has long been recognized. These types of models have been fully exploited in the context of analyses of the post-glacial rebound

problem (Peltier, 1974). The simplest rheological model is the Maxwell body and such a model was assumed throughout this work.

In the past, viscoelastic deformation modelling was limited by the assumption that the Earth is laterally homogenous (Farrell, 1972; Wu, 1978; Passey, 1981; Beaumont, 1981; Cant and Stockmal, 1989). To a second order, this limiting factor constrained the hypotheses and the rigour with which they could be tested against observation. In this text the effects of modelling a continental lithosphere that allows lateral in-homogeneities will be explored. The finite element method will be used in this modelling.

Chapter 2 provides a review of some pertinent theoretical foundations of deformation problems in geodynamics. The purpose of this review is twofold: to state clearly the assumptions underlying the theory; and to provide the basis for a comparison of the finite element method. By starting with the elastic and viscous equations of motion, the differences between them are first pointed out and then the viscoelastic equation is derived using the correspondence principle. The concepts of flexure, flexural parameter and peripheral bulge were also introduced in this section.

In chapter 3, the finite element method is given credibility by comparing finite element results with the analytical results derived in the previous chapter. This provides the confidence necessary to move on to other, yet untried, laterally heterogeneous models. Having clearly established both the advantages and limitations of this numerical method, the next step was to apply it using relevant geological data. This brings us to the primary purpose of this study.

The objective of chapter 4 was to describe a more realistic representation of basin evolution through lithospheric flexure. Flexure can be described as "regional isostacy" which takes the strength of the lithosphere into account. It is this lithospheric flexure that distributes the subsidence associated with orogenesis and glacial, sediment and eustatic loading over an area. Flexural modelling allowed us to simulate this regional isostatic response to loading for a given set of lithospheric parameters. Data from the

Alberta Foreland Basin were used to probe the characteristic properties of the North American cratonic lithosphere. The outputs of this model include: a predictive model of the paleogeography of the Alberta Foreland Basin; an estimate of the burial history which is necessary to calculate hydrocarbon maturation; a better understanding of the load history of the Rocky Mountain Fold and Thrust Belt; and, most importantly, a working rheological model showing lateral inhomogeneities in cratonic lithospheres. From this study, it is shown that the lithospheric model of the North American plate must thicken to the east to satisfy best the observed data. This hypothesis was tested in detail and forms the bulk of this work.

Final conclusions are then drawn in chapter 5 where the ideas are integrated into a larger geodynamic context. Future work where the finite element method can be used for different types of geodynamic modelling is also suggested as a direct result of this study.

Throughout this work, S.I. units were used except in some instances of time, where millions of years (Ma) were used for relaxation time as this was considered more meaningful than seconds. Large distances associated with cross-sections were also given in kilometres instead of metres. An attempt was also made to use different symbols for different notation whenever possible. The notation is clearly explained in the text as it is introduced and there should be no ambiguity.

"If geophysics requires mathematics for its treatment,
it is the Earth that is responsible
not the Geophysicist"

Sir Harold Jeffreys,
Cambridge University

2. Physical and Mathematical Foundations

This chapter introduces the necessary mathematical and physical background required to develop the geological models used in subsequent chapters. It also serves to check the finite elements results of Chapter 3 by comparing simple numerical models with analytical predictions. This will give us added confidence in the finite element results before going on to more complicated models.

The mechanical state of a body is specified by means of kinematic and dynamic quantities. The former refers to motion (*i.e.* displacement, velocity and acceleration), the latter to forces of various types. In the study of rheology we establish basic relations between kinematic and dynamic quantities for continuous media, analyze their meaning and implications and subsequently make use of their consequences. The basic dynamic quantity is stress τ and the basic kinematic quantity is strain ε (or strain rate $d\varepsilon/dt$). Both of these are tensors of rank two or second-order tensors (scalars and vectors are sometimes called zeroth- and first-order tensors respectively). Stress is related to the surface *force*, and strain is related to *deformation* within the body.

In this thesis we will be dealing with the deformation of a viscoelastic Maxwell body which behaves like a Hookean elastic body at short time scales but like a fluid at long time scales. This type of deformation will be described by applying the correspondence principle to the elastic equation of motion and this chapter will form the basis of the theory while clearly stating the assumptions and approximations behind them. It will naturally lead into chapter 3 where the usefulness and limitations of the finite element method will be compared with these analytical results in detail.

In section 2.1 the linearized equations of motion are reproduced after Cathles (1975) for simple elastic and viscous Earth models. In Section 2.2 dimensional analysis was used to compare the contribution of each of the terms in these equations of motion. These results will then be used as the basis for the theoretical development of the static deformation of an isotropic, *elastic* half-space. This problem is associated with the name of Boussinesq (Farrell, 1972) who first studied it in 1885, and is summarized in section 2.3. In sections 2.4 and 2.5, an extended form of the Correspondence Principle will be employed to derive the quasi-static deformation of isotropic, *viscoelastic* half-space Earth models by mass loads applied to the surface. Finally, section 2.6 will address the characteristics of the thin plate approximation for the flexural model of an infinite plate with a load that has a large lateral extent when compared with the thickness of the plate itself. It is in this section that the concepts such as flexure, flexural rigidity, and peripheral bulge are introduced.

2.1 Linearized Equations of Motion.

The elastic equation of motion is required to describe the behaviour of the Earth at short time scales and the viscous equation is necessary for the behaviour in the viscous limit. The transition between these two states however, is taken into account by the correspondence principle.

For a continuous body to be in equilibrium, the resultant of all body and surface forces, and the resultant moment about any axis, must vanish. The *linearized* elastic and viscous equations of motion in a pre-stressed, self-gravitating Earth model can be written as (Cathles, 1975):

$$\nabla.\tau - \rho_0\nabla(g_0 u_z) + g_0\rho_0(\nabla.\mathbf{u})\,\mathbf{z} - \rho_0\nabla\phi_1 = 0 \qquad (2.1.1)$$

$$\nabla.\tau + g_0\rho_0(\nabla.\mathbf{u})\,\mathbf{z} - \rho_0\nabla\phi_1 = 0 \qquad (2.1.2),$$

respectively. In these equations, τ is the stress tensor, ρ_0 and g_0 are the unperturbed (zeroth-order) density and gravity values respectively and the quantity ϕ_1 is the perturbed gravitational potential which is defined by Poisson's equation $\nabla^2\phi_1 = 4\pi G\rho_1$ where $G = 6.6732\times10^{-11}$ N m^{-2} kg^{-2} (the Universal Gravitational constant) and ρ_1 is the perturbed density.

The elastic equation of motion (2.1.1) incorporates four terms. These terms in the order they appear, are due to the: divergence of stress; advection of pre-stress; buoyancy force; and perturbation of gravity. The equation of motion for the viscous self-gravitating medium (2.1.2) however, does not have the pre-stress advection term. The advection term arises in equation 2.1.1 because, for an elastic solid, the displacement is instantaneous and carries the initial pre-stress along. In the viscous equation of motion however, the displacement *cannot* be sudden and hence the advection term does not appear (Cathles, 1975). The elastic problem and the viscous problem also have different boundary conditions. In the elastic problem, the boundary conditions are the continuity of displacements and stresses. In the viscous problem, the buoyancy force across the boundary must *also* be included in the continuity of the normal stress.

By starting with the elastic equation of motion and applying the Correspondence Principle, the advection of pre-stress term becomes the gradient of the buoyancy force across the boundary in the viscous limit. This term is combined with $\nabla.\tau$ to give the divergence of the viscous stress (Wu and Peltier, 1982). In other words, the advection of pre-stress term is necessary in the viscoelastic problem to satisfy the boundary conditions in the viscous limit.

2.2 Scale Analysis of Elastostatic Equation

A scale analysis of the equation of motion for a self-gravitating elastic body gives an estimate of the individual contributions of the divergence of stress; advection of pre-stress; buoyancy and the perturbation of gravity with respect to the size, or characteristic wavelength, of the load. In the following it will be shown that the perturbation of gravity term can be neglected for loads having a short characteristic wavelength. Using the same notation as in section 2.1, it was stated that equation (2.1.1) describing elastostatic equilibrium constituted four terms. Each of the four terms of equation (2.1.1) contributes to a specific physical property as shown below:

$$\underset{\substack{\text{Divergence}\\\text{of stress}}}{\nabla.\tau} \quad \underset{\substack{\text{Advection of}\\\text{pre-stress}}}{-\rho_0\nabla(g_0\mathbf{u}_z)} \quad \underset{\substack{\text{Buoyancy}\\\text{force}}}{+g_0\rho_0(\nabla.\mathbf{u})\,\mathbf{z}} \quad \underset{\substack{\text{Perturbation of}\\\text{gravity}}}{-\rho_0\nabla\phi_1} \quad = 0 \qquad (2.1.1).$$

Let us now define a cylindrical coordinate system with basis vectors **z**, **r** and θ. In order to solve for the dimensions of stress τ, gravitational potential ϕ_1 and density ρ_1, we require the following three relations:

$$\tau_{ij} = \lambda\,\varepsilon_{rr}\,\delta_{ij} + 2\mu\,\varepsilon_{ij} \qquad (2.2.1)$$

$$\nabla^2\phi_1 = 4\pi G\rho_1 \qquad (2.2.2)$$

and

$$\rho_1 = -\rho_0\,\nabla.\mathbf{u} - \mathbf{u}_r\partial_r\rho_0 \qquad (2.2.3).$$

Equation 2.2.1 is the relation between stress and strain, or displacement, while equation 2.2.3 can be derived by linearizing the usual conservation of mass equation.

Using braces to denote dimension and the notation [L] for the dimension of the characteristic wavelength, equation 2.2.1 has a dimensional relationship given by:

$$[\tau] = [\mu]\frac{[\mathbf{u}]}{[L]} \qquad (2.2.4).$$

Given that $g_0 = (4/3)\ \pi G a \tilde{\rho}$ where a is the equatorial radius of the Earth and $\tilde{\rho}$ is the average density from the surface down to the depth of penetration due to [L], equation 2.2.2 yields

$$[\phi_1] = [g_0][L]\frac{[\mathbf{u}]}{[a]} \qquad (2.2.5).$$

Equation 2.2.3 gives the dimensions of the perturbed density in terms of the zeroth-order density as $[\rho_1] = -[\tilde{\rho}][\mathbf{u}]/[L]$

Hence equation 2.1.1 along with the appropriate substitutions, reduces to

$$\underbrace{[\mu]\frac{[\mathbf{u}]}{[L]^2}}_{\text{Divergence of stress}} + \underbrace{[\tilde{\rho}][g_0]\frac{[\mathbf{u}]}{[L]}}_{\text{Advection of pre-stress}} + \underbrace{[\tilde{\rho}][g_0]\frac{[\mathbf{u}]}{[L]}}_{\text{Buoyancy force}} - \underbrace{[\tilde{\rho}][g_0]\left[\frac{\mathbf{u}}{a}\right]}_{\text{Perturbation of gravity}} = 0 \qquad (2.2.6),$$

where the contribution of each term is explicitly shown. Defining the quantity $[\vartheta]$ by

$$[\vartheta] = \frac{[L][\rho_0][g_0]}{[\mu]} \qquad (2.2.7),$$

and normalizing the divergence-of-stress term gives the following relative dimensional contributions:

$$\underset{\text{Divergence of stress}}{1} + \underset{\text{Advection of pre-stress}}{[\vartheta]} + \underset{\text{Buoyancy force}}{[\vartheta]} - \underset{\text{Perturbation of gravity}}{\frac{[L][\vartheta]}{[a]}} = 0 \qquad (2.2.8).$$

Equation 2.2.8 shows that both the buoyancy term and the advection of pre-stress term have the same order of magnitude but that the contribution due to the perturbation of gravity field term is much smaller provided $[L]/[a] \ll 1$.

Given that $[a] = 6{\cdot}3781\times10^6$ m, some typical values for $[\vartheta][L/a]$ are given in Table 2.2.1. Assuming that $[\tilde{\rho}]$ is as tabulated and measured in kg m^{-3}; $[\mu] = 10^{11}$ Pa; $[g_0] \approx 10$ m s^{-2}, then $[\vartheta]$ indicates where contributions from the buoyancy, advection of pre-stress and gravity perturbation terms become important. From Table 2.2.1, it is shown that the last term is negligible for loads smaller than the Fennoscandia ice sheets and therefore will be ignored throughout this study. Its contribution is equivalent to ≈ 3% of the dominant divergence of stress term for a loading problem with a characteristic wavelength similar to the Alberta Foreland Basin. This approximation results in an equation that is appropriate for modelling a flat Earth with a constant gravity field.

Location	**Characteristic Wavelength** L (km)	$[\tilde{\rho}]$ (kg m^{-3})	μ (Pa) $\times10^{10}$	$[\vartheta]$	$[\vartheta][L/a]$
Laurentide	3000	4448	17.26	0·77	0·36
Fennoscandia	2000	4037	13.01	0·62	0·19
Alberta Basin	550	3450	7.70	0·25	0·03
Lake Bonneville	200	3200	6.25	0·10	0·003

Table 2.2.1. Typical characteristic wavelengths L and ratios $[\vartheta]$ and $[\vartheta][L/a]$ for several loading experiments at various locations. The perturbed gravity field may be neglected for $[\vartheta][L/a] \ll 1$.

Finally, if we also assume that the halfspace is incompressible, *i.e.* $\nabla.\mathbf{u} = 0$, then equation (2.1.1) is further reduced to

$$\nabla.\tau - \tilde{\rho}\nabla(g_0 u_z) = 0 \qquad (2.2.9).$$

Table 2.2.1 shows that the advection of pre-stress term is also small for both Lake Bonneville and the Alberta Foreland Basin (25% of the $\nabla.\tau$ contribution) in the elastic problem. When this term is neglected, the problems are reduced to Boussinesq's problem and the plate flexure problem which are discussed in the following sections.

2.3 Boussinesq's Problem

In this section, Boussinesq's problem, where an elastic halfspace is perturbed by a surface load, will be reviewed (Boussinesq, 1885). Application of the Correspondence Principle, described in section 2.4, will subsequently allow us to derive the solution of a *viscoelastic* halfspace perturbed by a similar surface load (section 2.5). Both of these analytical results will be used to test the limitations of the finite element in chapter 3.

Let us consider the static equation for a Hookean elastic flat Earth model in the absence of gravity. Thus (2.2.9) reduces to $\nabla.\tau = 0$. By taking the divergence of the stress tensor in the constitutive relation for an elastic solid (2.2.1) and equating it to zero, we obtain, using the indicial notation,

$$\tau_{ij,k} = \partial_k\left\{\lambda\varepsilon_{rr}\delta_{ij} + 2\mu\varepsilon_{ij}\right\} = 0 \qquad (2.3.1).$$

Utilizing the definition of the strain tensor

$$\varepsilon_{ij} = \frac{1}{2}\left(\frac{\partial s_i}{\partial x_j} + \frac{\partial s_j}{\partial x_i}\right) \qquad (2.3.2),$$

where s is the displacement, we obtain the following

$$\tau_{ij,k} = (\lambda+\mu)\partial_i s_{r,r} + \mu\partial_i s_{j,k} = 0 \qquad (2.3.3a)$$

which, when expressed in the more familiar vector notation becomes (Farrell, 1972)

$$(\lambda+2\mu)\nabla\nabla.s - \mu\nabla_\times\nabla_\times s = 0 \qquad (2.3.3b).$$

Equation (2.3.3b) is identical to the familiar Naviér-Stokes equation of motion for seismic (elastic) wave propagation with the acceleration term set to zero. This is the elastostatic equation for a Hookean elastic solid without any body forces. The displacement **s** can be found by solving for (s_x, s_y, s_z) using the appropriate boundary conditions. Note that there is no time dependence in the displacement vector **s** since elastic deformation is instantaneous.

Let $z \leq 0$ be the volume occupied by the halfspace. For the time being, we seek solutions to (2.3.3) under the condition that the free surface be stress-free except for a disc load of radius a at the origin. Since the problem is axially symmetric, there is no θ dependence and therefore we let the displacement **s** be the sum of two orthogonal displacements such that

$$\mathbf{s} = u(z,r)\,\mathbf{z} + v(z,r)\,\mathbf{r} \qquad (2.3.4).$$

Following Farrell (1972), it can be shown that the final solution for the displacements produced at the surface of a semi-infinite isotropic elastic solid is:

$$
\begin{aligned}
u(0,r) &= \begin{cases} -\dfrac{\alpha}{\pi^2\mu\eta a} E\left(\dfrac{r}{a}\right) & , r < a \\ -\dfrac{\alpha}{\pi^2\mu\eta r}\left\{E\left(\dfrac{a}{r}\right) - \left(1 - \dfrac{a^2}{r^2}\right) K\left(\dfrac{a}{r}\right)\right\} & , r \geq a \end{cases} \\
v(0,r) &= \begin{cases} -\dfrac{r}{4\pi\eta a^2} & , r < a \\ -\dfrac{1}{4\pi\eta r} & , r \geq a \end{cases} \qquad (2.3.5). \\
\tau_{zz}(0,r) &= \begin{cases} -\dfrac{1}{\pi a^2} & , r < a \\ 0 & , r \geq a \end{cases}
\end{aligned}
$$

Equation (2.3.5) is expressed in terms of the elliptical integrals $E\left(\frac{r}{a}\right)$, $K\left(\frac{a}{r}\right)$ and the terms $\alpha = (\lambda+2\mu)$ and $\eta = (\lambda+\mu)$.

This problem was first studied by J. Boussinesq in 1885 and later on by others (Lamb, 1902; Farrell, 1972; Peltier, 1974). Further work has also been done on Boussinesq's problem with an external gravity field term included (Wolf, 1985). Since our intention is to treat the viscoelastic problem analytically, the natural next step in our discussion is to use the Correspondence Principle and apply it to equation (2.3.5) to obtain the associated viscoelastic solution. This is the topic of the next section.

2.4 The Correspondence Principle

As illustrated in the last section, the solution to the elastic problem can be obtained when the equation of motion is combined with the constitutive relation (2.2.1) and solved with the appropriate boundary conditions. For a viscoelastic body, the constitutive relation contains terms involving the rate of change of stress and strain (see 2.4.1) and thus the problem becomes more complicated. The Correspondence Principle however, makes the solution more tractable. Essentially the Correspondence Principle says that, in the transformed domain, the viscoelastic problem reduces to an "associated" elastic problem which can be solved with the techniques known for elastic problems. The following shows how this comes about (Cathles, 1975).

The one-dimensional analogue of the linear viscoelastic model otherwise known as the Maxwell solid can be represented by a spring and a dashpot in series as illustrated in Figure 2.4.1.

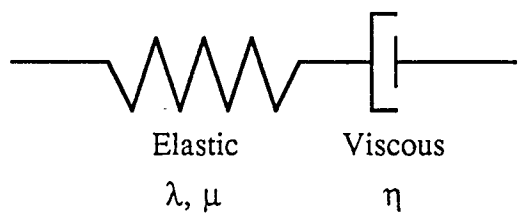

Figure 2.4.1. One-dimensional spring and dashpot analogue for a linear viscoelastic (Maxwell) solid. The parameters describing the Maxwell solid are the elastic parameters λ, μ (N m^{-2}) and viscosity η (Pa s).

The constitutive relation for a three-dimensional Maxwell body (Cathles, 1975) is:

$$\lambda\delta_{kl}\dot{\varepsilon}_{rr} + 2\mu\dot{\varepsilon}_{kl} = \dot{\tau}_{kl} + \frac{\mu}{\nu}\left\{\tau_{kl} - \frac{1}{3}\tau_{rr}\delta_{kl}\right\} \qquad (2.4.1).$$

Taking the Laplace transform of (2.4.1) gives

$$\lambda\delta_{kl}s\,\tilde{\varepsilon}_{rr} + 2\mu s\,\tilde{\varepsilon}_{kl} = \tilde{\tau}_{kl}s + \frac{\mu}{\nu}\left\{\tilde{\tau}_{kl} - \frac{1}{3}\tilde{\tau}_{rr}\delta_{kl}\right\} \qquad (2.4.2),$$

where tilde denotes the Laplace transformed variable and s is the transform variable. This can be written in contracted form and substituted back into equation (2.4.1) to give

$$\tilde{\tau}_{kl} = \left[\frac{\lambda\nu s + \mu\kappa}{s\,\nu + \mu}\right]\tilde{\varepsilon}_{rr}\delta_{kl} + 2\left[\frac{\mu\nu s}{s\,\nu+\mu}\right]\tilde{\varepsilon}_{kl} \qquad (2.4.3)$$

where κ is the bulk modulus. By comparing (2.4.3) with the constitutive relation for an elastic solid (*i.e.* equation 2.2.1), we can identify the terms in square braces to be $\lambda(s)$ and $\mu(s)$, which are the appropriate compliances for the associated problem. These compliances are given by:

$$\lambda(s) = \left[\frac{\lambda\nu s + \mu\kappa}{s\,\nu + \mu}\right]$$
$$\mu(s) = \left[\frac{\mu\nu s}{s\,\nu+\mu}\right] \qquad (2.4.4).$$

The equation of motion in the transformed domain is the same as (2.1.1) except that τ_{kl}, μ and ϕ, are variables in the transformed domain.

Hence we can treat the viscoelastic problem by direct analogy with the elastic problem using the Correspondence Principle. The basis for this principle is that with zero initial conditions the Laplace or Fourier time-transformed viscoelastic equations and boundary conditions are formally identical with the equations for an elastic body of the

same geometry (Peltier, 1974). Hence, if the solution of the elastic problem is known, then by substituting the elastic constants λ and μ by the operational modulii or compliances $\lambda(s)$ and $\mu(s)$, and replacing the time dependence of the prescribed loading and displacements by transformed quantities, the viscoelastic problem *in the transformed domain* can be obtained. This solution however, has to be inverted to the time domain.

2.5 Static Equilibrium Equation for a Viscoelastic Halfspace

Using the same notation as previously, let us find the solution at the surface for $\mathbf{u}(z=0, r, t)$. Equation (2.3.5) can be rewritten in the transformed Laplace domain, where the elastic constants λ and μ are replaced by their compliances $\lambda(s)$ and $\mu(s)$ to give

$$u(0,r,s)=\begin{cases} -\dfrac{\tilde{\alpha}(s)}{\pi^2\tilde{\mu}(s)\tilde{\eta}(s)\,a}\,E\left(\dfrac{r}{a}\right) & , r<a \\ -\dfrac{\tilde{\alpha}\,r}{\pi^2\tilde{\mu}(s)\tilde{\eta}(s)\,a^2}\left\{E\left(\dfrac{a}{r}\right)-\left(1-\dfrac{a^2}{r^2}\right)K\left(\dfrac{a}{r}\right)\right\} & , r\geq a \end{cases} \qquad (2.5.1).$$

Also assume for the moment that $r < a$. By substituting the appropriate modulii of elasticity we obtain an expression which is in the form of a quadratic in s divided by another quadratic in s. Explicitly written, this becomes:

$$u(0, r, s) = -\left[\frac{E\left(\frac{r}{a}\right)}{\pi^2 a}\right]\frac{\left[(\lambda+2\mu)\,s+\frac{\mu\kappa}{\nu}\right]\left(s+\frac{\mu}{\nu}\right)}{\mu s\left[(\lambda+\mu)\,s+\frac{\mu\kappa}{\nu}\right]} \qquad (2.5.2),$$

which is difficult to invert as it stands.

The inverse Laplace transform of equation 2.5.2 is the solution to the viscoelastic problem. In order to take the inverse Laplace transform of this expression, we must first reduce the order of the numerator. This is accomplished by first finding the elastic asymptote by taking the limit $s \to \infty$ (which implies that $t \to 0$) as follows (Wu and Peltier, 1982):

$$\lim_{s\to\infty} -\frac{E\left(\frac{r}{a}\right)}{\pi^2 a}\frac{\tilde{\alpha}}{\tilde{\mu}\tilde{\eta}} = -\frac{E\left(\frac{r}{a}\right)}{\pi^2 a}\frac{(\lambda+2\mu)}{\mu(\lambda+\mu)} \qquad (2.5.3)$$

This term is independent of s and inversion will give the same term back, multiplied by a delta function in time. The second step is to subtract equation 2.5.3 from u(0, r, s) to obtain the *viscous* portion $\tilde{u}^{V}(0, r, s)$ of the solution. We can then take the inverse Laplace transform of the viscous portion of the solution using Cauchy's residual theorem or other standard methods

$$\tilde{u}^{V}(0, r, s) = \frac{E\left(\frac{r}{a}\right)}{\pi^2 a} \frac{\left(\frac{\mu}{V}\right)\left[(\eta\alpha+\eta\kappa+\alpha\kappa)\, s + \eta\left(\frac{\mu}{V}\right)\kappa\right]}{\mu\eta s\left(\eta s+\mu\frac{\kappa}{V}\right)} \tag{2.5.4}$$

to obtain the impulse response. Adding back the time-domain elastic contribution gives the total solution for the displacement due to an impulsive load. This can be written as

$$u(0, r < a, t) = \frac{E\left(\frac{r}{a}\right)}{\pi^2 a}\left\langle \frac{\lambda+2\mu}{\mu(\lambda+\mu)}\,\delta(t) + \frac{1}{\eta\mu\, C}\left\{B - \left(B - \frac{AC}{\eta}\right)\exp^{-\frac{Ct}{\eta}}\right\}\right\rangle \tag{2.5.5}$$

$$A = (\eta\alpha + \eta\kappa + \alpha\kappa)$$

$$B = \eta\kappa\frac{\mu}{V}$$

$$C = \frac{\mu\kappa}{V}$$

Since we are interested in the response due to a disc load left on the Earth's surface *over a period of time* $T = t$, we must convolve the solution 2.5.5 with a Heaviside function $H(t)$. This gives the following (Peltier, 1974):

$$\mathbf{u}(0, r<a, t) = -\left[\frac{E\left(\frac{r}{a}\right)}{\pi^2 a}\right]\left\{\frac{\lambda+2\mu}{\mu(\lambda+\mu)} + \frac{t}{V} - \frac{1}{\mu\kappa}\left[\eta - \frac{A}{\eta}\right]\left(1 - e^{-\frac{Ct}{\eta}}\right)\right\} \tag{2.5.6 a}$$

This equation represents the displacement at the surface due to a disc load of radius a placed over an infinite viscoelastic halfspace for a period of time t. Applying the same procedure for $r \geq a$ gives the rest of the solution which only differs by the coefficient outside the braces. The solution of u(0, $r > a, t$) is given by

$$u(0, r > a, t) = -\frac{r}{\pi^2 a^2}\left[E\left(\frac{a}{r}\right) - \left(1 - \frac{a^2}{r^2}\right)K\left(\frac{a}{r}\right)\right] \times \left\{\frac{\lambda+2\mu}{\mu(\lambda+\mu)} + \frac{t}{\nu} - \frac{1}{\mu\kappa}\left[\eta - \frac{A}{\eta}\right]\left(1 - e^{-\frac{Ct}{\eta}}\right)\right\} \qquad (2.5.6\ b).$$

These expressions for the viscoelastic halfspace reduce to the elastic solution if we choose time $t = 0$ since by definition an elastic medium must adjust instantaneously to an applied load.

2.6 Thin Layer Plate Approximation

For loads of duration much longer than the relaxation time $\tau(k)$ of the upper mantle for that load wavelength, the Earth can be represented by using a rigid lithosphere overlying a fluid mantle. In contrast to the last problem, a buoyancy force is included here due to the density contrast of the lighter load displacing the denser mantle material. If this load has a characteristic length much greater than the thickness of the lithosphere, we can approximate the model by a thin plate supported by a fluid mantle. For this problem, the upper mantle is completely relaxed; thus we cannot "see" the mantle viscosity but we can use the information from this type of loading experiment to study the properties of the lithosphere. If we consider small deflections in a thin plate, thereby assuming that (i) the fibre stresses τ_{xx} and τ_{yy} vary linearly throughout the thickness of the plate, (ii) there are no shear stresses τ_{zx}, and (iii) the in-plane normal stress $\tau_{zz} = 0$, we can write the equilibrium equation for two-dimensional flexuring of plates as (Turcotte and Schubert, 1981):

$$D\frac{d^4 w(x)}{dx^4} = q(x) - P\frac{d^2 w(x)}{dx^2} \qquad (2.6.1),$$

where $w(x)$ is the vertical displacement, $q(x)$ is the vertically applied load, and P is the horizontal force. D is a quantity known as the flexural rigidity which quantifies the lithospheric stiffness and is usually expressed in Newton metres (N m). The flexural rigidity D is defined by:

$$D = \frac{E\,d^3}{12\left(1-\nu^2\right)} \qquad (2.6.2)$$

for a given Young's modulus E, Poisson's ratio ν and lithospheric thickness d.

For our surface loading problem, take the horizontal forces $P = 0$ and a load $q_a(x)$ that is applied vertically. The load is supported by the plate and the buoyancy force. Thus for a mantle density ρ_m, sediment density ρ_s and density of water ρ_w, the net force $q(x)$ is $q_a(x) - (\rho_m - \rho_w)gw(x)$ for the oceanic lithosphere case and $q_a(x) - (\rho_m - \rho_s)gw(x)$ for the continental crust case. Hence the fourth-order differential equation describing the displacement due to vertical loading with a buoyancy term counteracting it (Walcott, 1970) can be written as:

$$D\,\frac{d^4w(x)}{dx^4} - (\rho_m - \rho_f)\,g\,w(x) = q_a(x) \qquad (2.6.3),$$

where the replacement density ρ_w or ρ_s has been written as ρ_f for generality.

For a loading problem in cylindrical coordinates, the boundary conditions are as follows:

(i) $dw/dr = 0$ at the centre, at $r = 0$.

(ii) w, dw/dr and d^2w/dr^2 are all continuous at the load edge, $r = A$

(iii) and the displacement $w = 0$ at $r = \infty$.

In the following, the functions ber, bei, ker and kei are the Bessel-Kelvin transcendental functions of zero order. The solution for (2.6.3) takes a particularly simple form for axisymmetrical loads (Brotchie and Silvester, 1969). For a point load $w = \frac{q_a\,l^2}{2\pi D}$ kei

$\left(\frac{r}{l}\right)$ where l is the radius of relative stiffness. l has dimensions of metres and is defined by $l^4 = D/(\rho_m - \rho_f)g$ where ρ_f is once again the fill-in density. Note that for two dimensional problems, as in chapter 4, the flexural wavelength l_{2D} is more appropriate and is defined by $l^4_{2D} = 4D/(\rho_m - \rho_f)g$. For a uniform disc load of density ρ, height δ and radius A, the deflection at $r \leq A$ is

$$w = \frac{\rho\delta}{(\rho_m - \rho_f)}\left[\, 1 + C_1 \operatorname{ber}\left(\frac{r}{l}\right) + C_2 \operatorname{bei}\left(\frac{r}{l}\right)\right] \qquad (2.6.4\ a)$$

and at $r > A$ the deflection is

$$w = \frac{\rho\delta}{(\rho_m - \rho_f)}\left[\, C_3 \operatorname{ker}\left(\frac{r}{l}\right) + C_4 \operatorname{kei}\left(\frac{r}{l}\right)\right] \qquad (2.6.4\ b).$$

The constants C_i are evaluated from the appropriate boundary conditions and are given by the following

$$\begin{aligned} C_1 &= \frac{A}{l} \operatorname{ker}'\left(\frac{A}{l}\right) \\ C_2 &= -\frac{A}{l} \operatorname{kei}'\left(\frac{A}{l}\right) \\ C_3 &= \frac{A}{l} \operatorname{ber}'\left(\frac{A}{l}\right) \\ C_4 &= -\frac{A}{l} \operatorname{bei}'\left(\frac{A}{l}\right) \end{aligned} \qquad (2.6.4\ c),$$

where the primes indicate derivatives with respect to the argument (A/l) of the Bessel-Kelvin functions.

For a thicker lithospheric plate the thin layer approximation does not hold and equations 2.6.1 and 2.6.3 are no longer valid. Note that the viscosity of the mantle does not come into the solutions of 2.6.1 since we assume the mantle is an inviscid fluid.

A plot of the deformation of a thin plate due to a point load is shown in Figure 2.6.1. The values used in this figure are a flexural parameter l_{disc} = 102·2 km and a flexural rigidity $D = 3{\cdot}64\times10^{24}$ N m. The deflections due to point loads $-q_a = 1{\cdot}08\times10^{18}$ N and

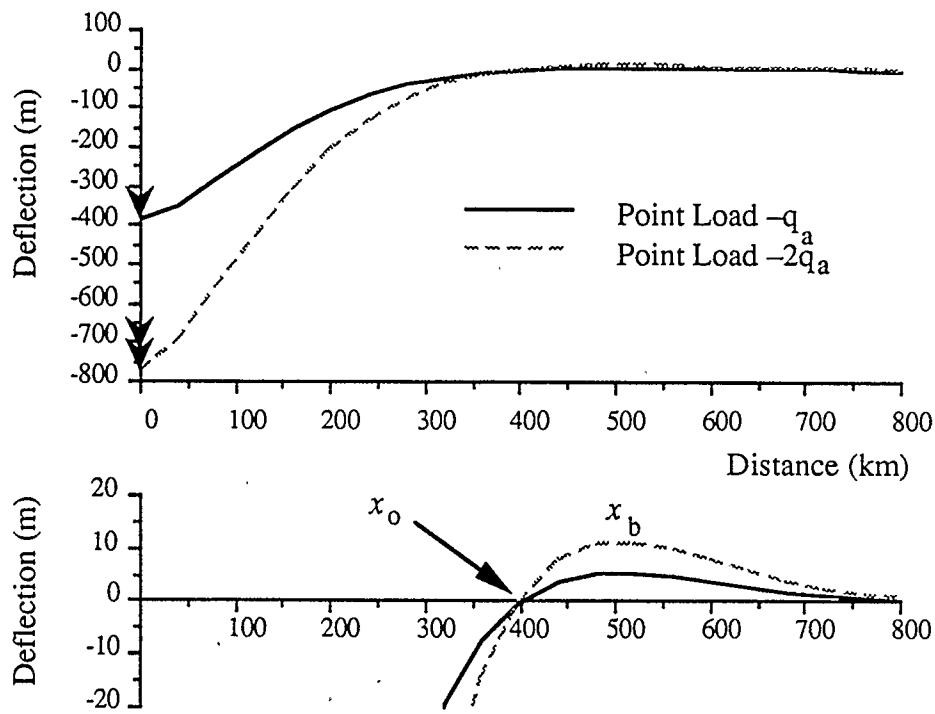

Figure 2.6.1. Rigid elastic lithosphere with l = 102·2 km and $D = 3{\cdot}64\times10^{24}$ N m overlying a fluid mantle. [Above] The flexure of the unbroken lithosphere for point loads $-q_a = 1{\cdot}08\times10^{18}$ N and $-2q_a$ at $x = 0$ gives maximum displacements of w_0 = –387 m and –774 m at $r = 0$ respectively. There is zero displacement at $x_0 \approx 400$ km and a peripheral bulge with a maximum height of $w(x_b)$ = 5·53 m and 11·06 m, respectively, at x_b = 504 km. [Below] Enlarged portion of the same plot showing the deflection near the surface around x_0 and x_b.

$-2q_a = 2{\cdot}16\times10^{18}$ N, both located at $x = 0$ km, correspond to –387 m and –774 m respectively.

Some important features of Figure 2.6.1 are the location of the cross-over distance at $x_0 \approx 400$ km; the location of the peripheral bulge at $x_b \approx 504$ km; and the maximum displacements $w(x_b) = 5{\cdot}53$ m and $11{\cdot}06$ m for each of the two loads respectively. The locations at x_0 and x_b are related to l (and hence the flexural rigidity D and plate thickness d) and do not change when the load magnitude varies. Thus the location of the peripheral bulge contains information on the lithosphere. The maximum deflection $w_0 = w(0)$ and the height of the peripheral bulge $w(x_b)$ however, both depend on the applied load magnitude.

The effects of having a *disc* load rather than a *point* load are shown in Figure 2.6.2. In

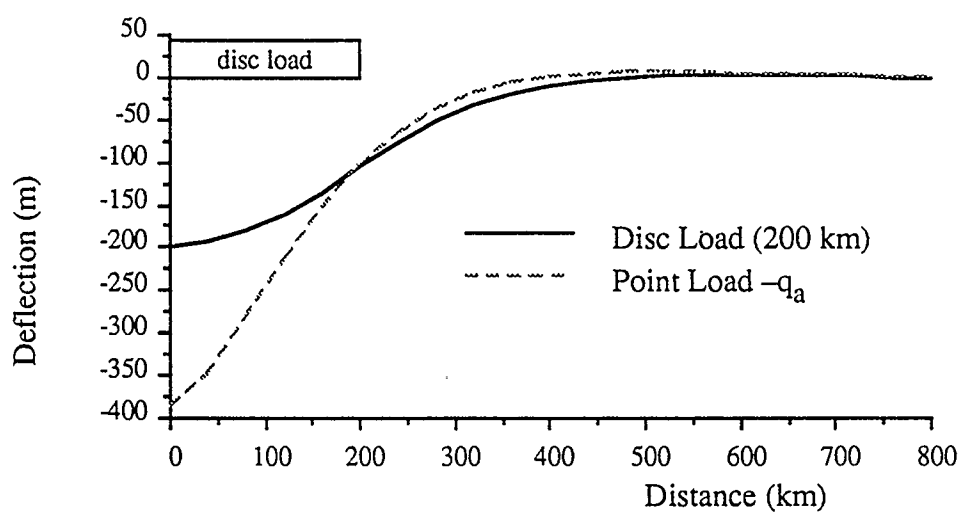

Figure 2.6.2. Deflection of a disc load of radius 200 km and a mass $-q_a = 3{\cdot}75\times10^{12}$ N. Notice that the deflection w_0 is smaller at $x = 0$ km and that the deformation is spread out further. The locations x_0 and x_b are different than those calculated for a point load. The flexure due to a point load $-q_a$ is also shown in dashed for comparison.

this figure, the disc has the same weight $-q_a$ as the point load of $-q_a$ but with the pressure distributed over a disc radius of 200 km. The deflection due to the point load $-q_a$, as taken from Figure 2.6.1, is roughly twice as great as the deflection produced by the distributed load which is shown in the dashed line for comparison.

Theoretical locations of the zero crossing x_0 and the peaks of the arch x'_b, x_b for both a point load and a disc load using an axisymmetrical coordinate system are given in Table 2.6.1 (McNutt and Menard, 1982):

Point Load	**Disc Load**
$x_0 = 3{\cdot}915\, l$	$x_0 = \sqrt{2}\, l \left[\frac{7\pi}{8} + \tan^{-1}\left(\frac{C_3}{C_4}\right)\right]$
$x'_b = 4{\cdot}932\, l$	$\tan\left(\frac{x_b}{\alpha}\right) = \left(1 + \frac{1}{2\frac{x_b}{\alpha} + \frac{7\pi}{8} + 2\tan^{-1}\left(\frac{C_3}{C_4}\right)}\right)^{-1}$
	where $\frac{x_b}{\alpha} = \frac{x'_b}{\alpha} - \frac{7\pi}{8}\tan^{-1}\left(\frac{C_3}{C_4}\right)$ $\alpha = \sqrt{2}\, l$

Table 2.6.1. The locations of the zero crossing x_0 and the peak of the peripheral bulge x'_b and x_b for a point load and a disc load respectively using an axisymmetric coordinate system. (see Appendix A, pp 363-394, McNutt and Menard, 1982).

"ABC as we build blocks 123"

Fred (1984),
from the Book of Fred

3. The Finite Element Method

In this chapter we will focus on the *finite element method* as it applies to structural analysis and we will show how we can apply the method to obtain numerical solutions to problems in geophysics. After a brief introduction to the finite element method and the underlying principles governing it, the analytical solutions of the previous chapter will be used to check the accuracy of the finite element method. Once the accuracy of the finite element method is established, it will be used to solve more difficult problems such as models that incorporate lateral inhomogeneities.

The finite element method falls into the broader category of discretization methods in the theory of continuum mechanics (see for example, Zienkiewicz, 1975). The idea behind continuum mechanics is to obtain a field function (such as a displacement or stress field function) over the continuous domain occupied by the medium. Mathematically these fields are governed by differential and integral equations. The solutions of these equations in real life situations are complex and generally not obtainable using known, closed form analytical functions. The use of the methods of discretization and numerical approximation to solve these problems has therefore been a fertile research field. Among the various discretization procedures available, one may also include: power series expansion methods, where the solution is expanded in a Taylor series; the finite difference method, where differentials are approximated by difference quotients; and Ritz's and other methods of the calculus of variations in which one starts with a variation-like principle (such as minimum potential energy, etc.) and assumes a solution to belong to a family of smooth functions. The finite element method is formally connected to the Ritz method.

In the finite element technique, the Earth is discretized into a number of elements. Each element contains information on geometry and material property. Each of these elements are interconnected by *nodal points*. For a certain loading problem, nodal

forces act at these nodal points, and at each nodal point the nodes are allowed to move in a number of directions (determined by the degrees of freedom). Within the elements, the displacement field is obtained by interpolation between the displacements at the nodes. Hence a standard set of simultaneous equations can be formulated at each element that relates the nodal forces, nodal displacements, and material properties. Physically assembling these elements to form the whole structure is equivalent to mathematically superimposing the element equations. The result is a large number of simultaneous equations which are suited for solution by computer. The result given is a distribution of the stress field or displacement field that closely approximates the correct solution.

3.1 Basic Structural Concepts

The basis of the finite element method lies in the principle of virtual work. The Principle of Virtual Work essentially solves $\nabla.\tau + f = 0$ in integral form. In order to explain the Principle of Virtual Work we must define virtual displacement. Virtual displacement can be loosely defined as a small smooth displacement field on the structure that is compatible with its supports. This means that it cannot violate the support conditions. It follows then that *virtual work* is the work done on the body due to this virtual displacement field $\{\delta \mathbf{U}\}$. The *external* forces on a body are the body forces $\mathbf{f}_b$ (due to its own weight); surface tractions $\mathbf{f}_s$ (force per unit area at the surface) and concentrated, or point, forces $\mathbf{F}_i$ (where distributed forces may be modelled as a series of concentrated forces). These external forces do work called *external virtual work*. Since the body is not perfectly rigid, any virtual work due to an infinitesimal displacement field will give rise to a stress field and subsequently a virtual strain field $\{\delta\varepsilon\}$. The *internal virtual work* is the work performed as a result of this stress field.

The principle of virtual work asserts that this stress field is in equilibrium with given external forces ($\mathbf{F}_i$, $\mathbf{f}_b$ and $\mathbf{f}_s$), if and only if, the internal virtual work (IVW) is identically equal to the external virtual work (EVW) for *all* possible displacements. It can be shown that the principle of virtual work (PVW) reduces to the equilibrium equations. Different numerical procedures for finding the solution exist. Of the more common methods, one is to approximate partial derivatives with finite quotients (finite difference method); and another is to make an approximation to the principle of virtual work and use the finite element method. Both methods will converge to the required solution.

An approximation to the principle of virtual work is the Ritz Approximation, and is made to convert equation 2.2.9 into integral form. Mathematically, the principle of virtual work can be stated as follows:

$$\mathrm{IVW} = \int_V \left[\tau_{ij}\delta\varepsilon_{ij}\right] dV \equiv$$

$$\mathrm{EVW} = \int_V \{\mathbf{f}_b\}^T \{\delta\mathbf{U}\}\, dV + \int_S \{\mathbf{f}_s\}^T \{\delta\mathbf{U}\}\, dS + \sum_{i=1}^{n} \{\mathbf{F}_i\}^T \{\delta\mathbf{U}_i\} \qquad (3.1.1).$$

In this equation, **V** is the volume and **S** is the surface of the body and superscript T represents the transpose of the matrix.

3.2 Comparison of Finite Element Method Results

In order to determine how well the results of the finite element method compare with the exact analytical solutions derived in the previous chapter, let us consider the following numerical example using some typical Earth parameters. Assume an infinite halfspace in a cylindrical coordinate system (r, θ) with a modulus of elasticity $\lambda = 7{\cdot}96\times10^{10}$ N m^{-2} and a modulus of rigidity $\mu = 6{\cdot}25\times10^{10}$ N m^{-2}. Consider a rigid disc load having the same Lake Bonneville Basin dimensions as given in Table 2.2.1. The pluvial lake roughly corresponds to an evenly distributed mass of $10{\cdot}15\times10^{15}$ kg covering a circular area of radius A = 80 km (Passey, 1981).

(a) Elastic Deformation (Boussinesq's Problem):

In this subsection, first assume that the infinite halfspace is completely *elastic*. Since the computer mesh must be finite in dimension, *infinity* for the model is considered to be any point beyond which the effects of the load will not be felt. The edges of the model therefore, were taken to be $25A$ in both the horizontal and vertical directions. This lateral extent was known to be sufficiently far away using the analytic (elastic) solution given in equation 2.3.5.

Each element was chosen to be 10 km^2 in cross-section and axisymmetric about the azimuth θ. Hence the elements at the centre are discs of radius 10 km and all others are toroids.

Such a disc load will theoretically give rise to the non-physical result of a discontinuous stress drop between $(A-\delta r) < x < (A+\delta r)$ as $\delta r \rightarrow 0$. Figure 3.2.1 shows how the finite element treats the problem of this distributed load type using the work-load equivalent method.

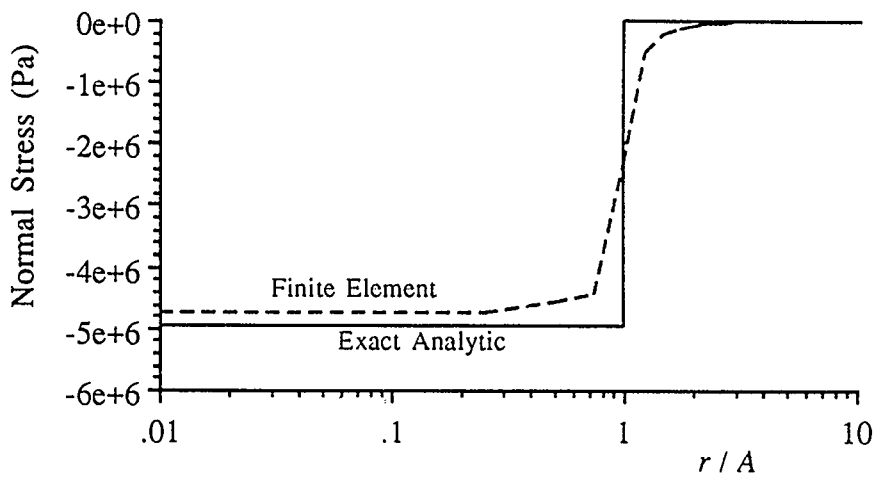

Figure 3.2.1. Comparison of normal stress as a function of distance (dimensionless) using both analytic and finite element methods. The finite element method makes use of the work-load equivalent method across the discontinuity. The abscissa (r/A) is plotted on a logarithmic scale.

Substituting the numerical values given above into equation 2.3.5 gives the theoretical displacement u(r) as a function of the distance r from the centre. A comparison of the analytic results with the finite element results can be seen in Figure 3.2.2. The radius r in both Figures 3.2.1 and 3.2.2 is dimensionless as it was normalized by the disc radius A. The abscissa is also plotted on a logarithmic scale to emphasize the results within the disc ($r/A < 1$). The finite element results were found to compare quite well with the exact solution. A plot of the difference between the analytically derived displacements and the numerical modelling results is shown in Figure 3.2.3. It should be noted that the finite element model had a maximum discrepancy of – 0·18 m (5%) occurring at the edge of the load where $r = A$.

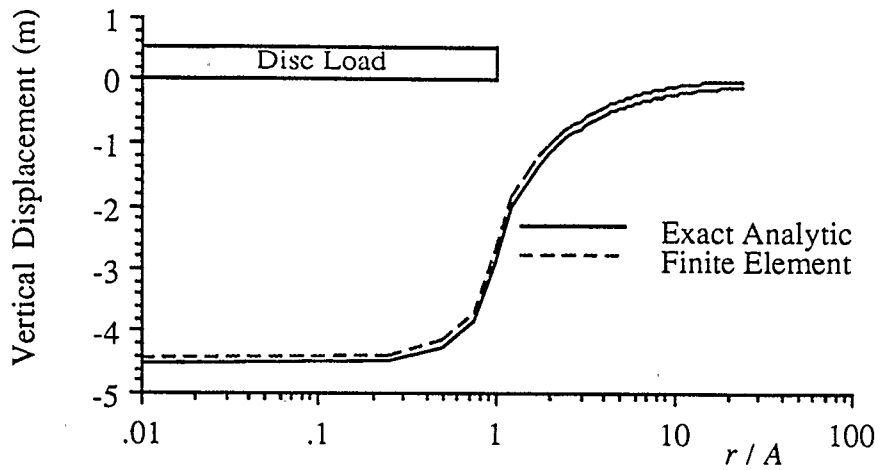

Figure 3.2.2. Vertical displacement versus (normalized) distance from centre due to a uniform disc load over a Hookean halfspace. The model, which uses the same order-of-magnitude parameters as for the Lake Bonneville Basin, compares well with the solution to Boussinesq's problem derived in section 2.3.

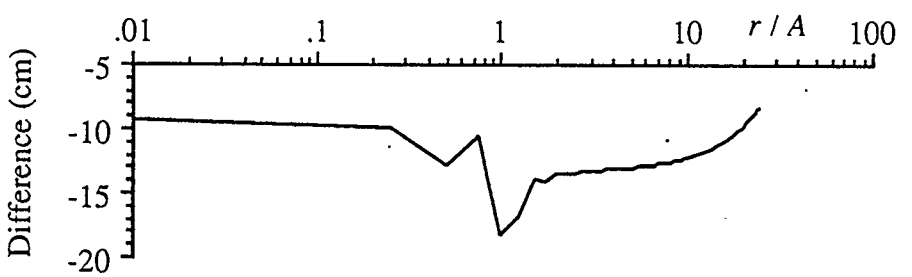

Figure 3.2.3. Difference in vertical displacement between analytical solution and finite element method for elastic experiment. The largest discrepancy occurs at the edge of the load (*i.e.* at $r/A = 1$) with a difference of -0.18 m.

(b) Viscoelastic Deformation:

Let us compare the results of the viscoelastic solution by assuming a creep experiment consisting of an infinite viscoelastic halfspace with a viscosity of 10^{21} Pa s and a total creep time of $T = 4{\cdot}11\times10^{11}$ s (13 000 years). The elastic parameters λ and μ were assumed to have the same values as for the elastic case. The model has the same shape as in the previous case but the lateral extent is greater to allow for more deformation. The new model extent was $50A$ in the horizontal direction since, for the viscoelastic creep experiment, the amplitude was greater. The theoretical displacement was given by equation 2.5.6. The displacement shown in Figure 3.2.4 is the result of the elastic component of displacement added to the viscous (or creep) component caused by the fluid mantle flow during the 13 ka period. The elastic component was found to be around – 4·54 m at $r = 0$ while the total maximum displacement was around – 80 m at the centre.

The displacement $u(r, z)$ does not theoretically fall to < 0·1 m before about $r = 500A$ when using a creep time of 13 ka. Hence our notion of "infinity" for the computer model was difficult to achieve in practice. (There was a trade-off between obtaining elements of a reasonable size for a load of only 80 km and the size of the total model with respect to computer time). At the surface boundary edge of our model *i.e.* at coordinate ($r = 4\times10^6$ m, θ, $z = 0$ m) the theoretical displacement was – 0·868 m whereas the finite element model was forced to be 0·000 m. The results were found to be quite good despite this limitation and are shown in Figure 3.2.4.

Although it is difficult to see, the finite element results in Figure 3.2.4 started to show a slight positive bulge beyond $r = 17A$. This was attributed to the fact that, in the finite element model, the mantle was not great enough in depth and extent and hence some material flowed and accumulated outside the load.

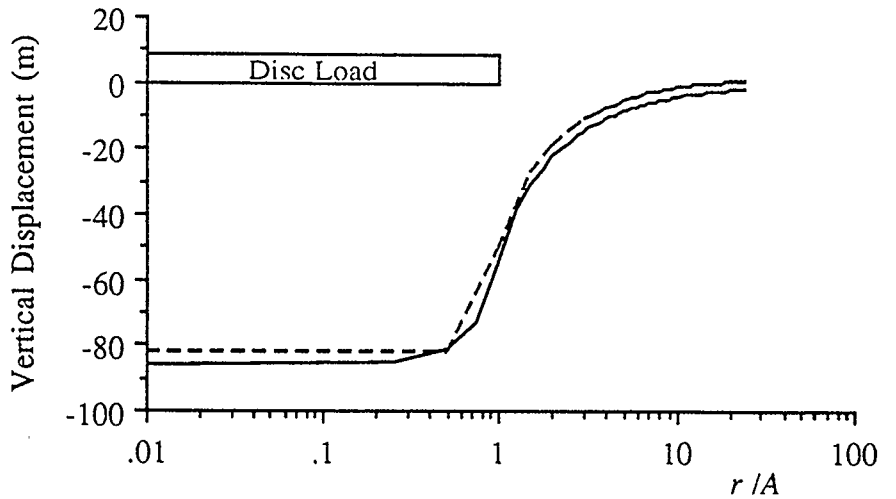

Figure 3.2.4. Comparison of the displacement profile of analytical results (solid line) with numerical or finite element method results (dashed) for a Maxwell body loaded by a disc for a total loading period of 13 ka. The parameters used were taken from Lake Bonneville Basin.

Figure 3.2.5 shows how well the finite element results compare with theory. The difference between the exact theoretical results and the finite element results was plotted in metres as a function of radial distance r which once again was normalized by A and plotted on a logarithmic scale. The maximum difference between the results was of the order of – 5 m and occurred at the edge of the load.

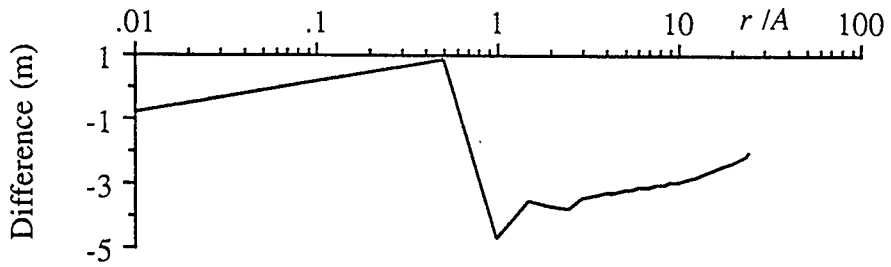

Figure 3.2.5. Difference between the displacements derived from the analytical results and finite element results shown in Figure 3.3.4. The largest error was a difference of – 4·73 m (≈ 5·9 %)at the load edge where $r/A = 1$.

To summarize, the mean of the differences was – 0·12 ± 0·02 m for the Hookean solid and – 2·95 ± 0·72 m for the Maxwell Earth after 13 ka creep. The maximum discrepancies in these results were found to be – 0·18 m for the elastic analysis and – 4·73 m for the creep experiment. Both of these errors occurred at the disc edge where $r/A = 1$ and were smaller elsewhere.

In conclusion, a comparison of the displacements obtained using finite element modelling with the analytical solution for both an elastic halfspace and a viscoelastic halfspace shows that the finite element method can give a good approximation to the analytical results.

3.3 Thin Layer Model

Let us now consider an Earth model consisting of an elastic lithosphere supported by a fluid mantle as described in Section 2.6. In that section we stated that for a load of a long time duration (say a few times the relaxation time), and a radius A that is much greater than the lithospheric thickness d, the model can be approximated by the bending of a thin elastic plate supported by buoyancy forces.

The numerical model chosen for comparison was a 40-km thick elastic lithosphere supported by a fluid mantle exerting a restoring force proportional to $(\rho_m - \rho_s)g$ where the density of the mantle ρ_m was 3400 kg m^{-3} and there was noreplacement density ρ_s (implying that there were no sediments deposited). The finite element model will be used since it does not require that the plate is thin. The disc of radius A = 240 km exerted a pressure of $\rho g \delta$ = 10 MPa on the surface. This is equivalent to a seamount

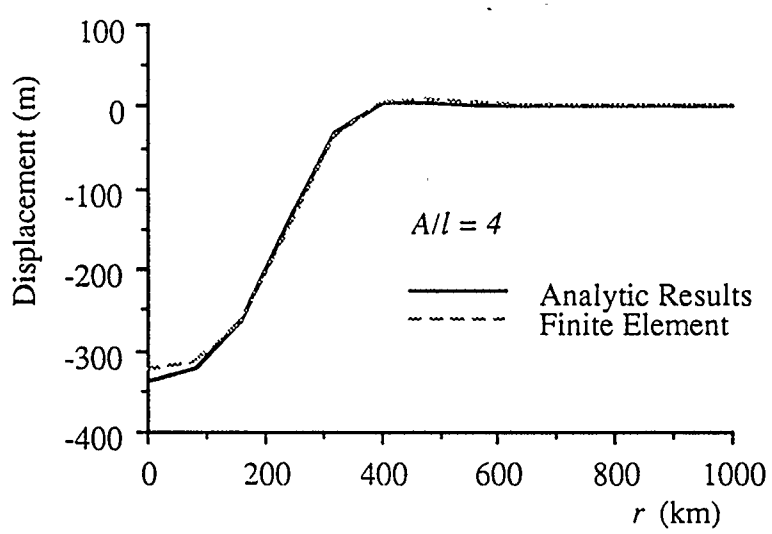

Figure 3.3.1. Comparison of the finite element method with analytical results for the displacement of a thin elastic lithosphere overlying a fluid mantle. The load exerted a 10 MPa pressure and consisted of a disc of radius 240 km.

load of average basaltic density 2800 kg m^{-3} and height δ of 357 m measured from the seafloor. The axisymmetric model consisted of fifty elements across and four elements down. Each element was 40 km long by 10 km deep to simulate a lithospheric model that was 2000 km long and 40 km thick. Other parameters used were Young's modulus $E = 0{\cdot}8\times10^{11}$ N m^{-2} and Poisson's ratio $\nu = 0{\cdot}28$. The imposed boundary conditions were that the outer model circumference was constrained in both the x- and z-directions. The buoyancy force was modelled by using an elastic or Winkler foundation (Kerr, 1964) beneath the lithosphere that exerted a restoring force proportional to the displacement. The radius of relative stiffness l of the elastic lithosphere was calculated to be 61·02 km and hence the flexural rigidity D was $4{\cdot}63\times10^{23}$ N m. The results in Figure 3.3.1 show a very good match between the solution derived in Equation 2.6.4 and the finite element method. This shows that the plate approximation is valid when $A/l \approx 4$. The maximum (analytical) displacement at the centre is – 337·3 m below the surface. The height of the forebulge is 6.24 m and

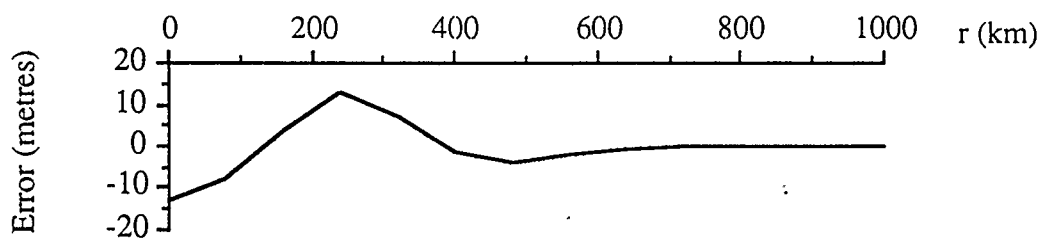

Figure 3.3.2. Difference between the approximate (see text) analytical results and the finite element method for the viscous model described in text. The maximum discrepancies found at the centre and load edges are around –13 m and +13 m respectively.

occurs at r = 447·16 km. The displacement, which oscillates between negative and positive due to the nature of the ber(A/l) and bei(A/l) functions, is heavily damped and has a first zero crossing at about r = 383 km. The difference between the analytical

results and the numerical modelling results is shown in Figure 3.3.2 above. It should be noted that both the finite element and the analytical results are only an approximation to the rigorous flexure problem (Lambeck and Nakiboglu, 1980). The difference in the two methods ranges from – 12·6 m at the centre to 12·8 m at $r = A = 240$ km (*i.e.* the disc edge).

For progressively thicker plates, the thin plate approximation used in the analytical derivation did not hold. As lithospheric thicknesses increase from 80 km to 120 km and 240 km, the corresponding flexural parameters become $l_{80} = 102{\cdot}63$, $l_{120} = 139{\cdot}10$, $l_{240} = 233{\cdot}94$ km respectively, hence the corresponding ratios A/l become ≈ 2·34, 1·73, and 1·03 for each of the three lithospheric thicknesses. Consequently, the thin plate results steadily deviated from the finite element results as A/l decreased (see Figure 3.3.3). The maximum discrepancies occurred at the centre and are 40·9 m, 83·3 m and 120·1 m for each of the increasingly thickening lithospheres respectively.

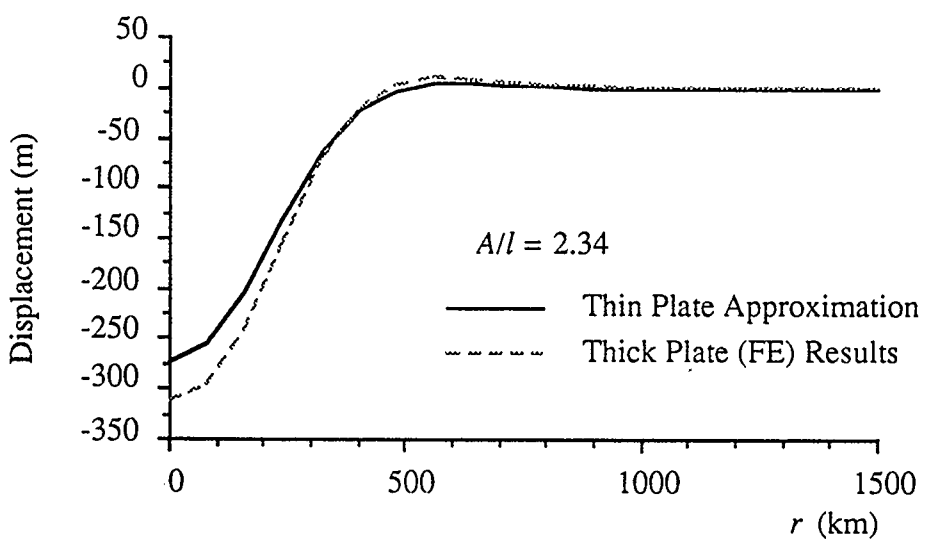

Figure 3.3.3. Comparison of thin plate theory with thick plate modelling for three different lithospheric thicknesses holding all other variables constant. (Top) Lithosphere is 80 km thick and $A/l = 2{\cdot}34$; [Overleaf] (Top) Lithosphere is 120 km thick and $A/l = 1{\cdot}73$; (Bottom) Lithosphere is 240 km thick and $A/l = 1{\cdot}03$.

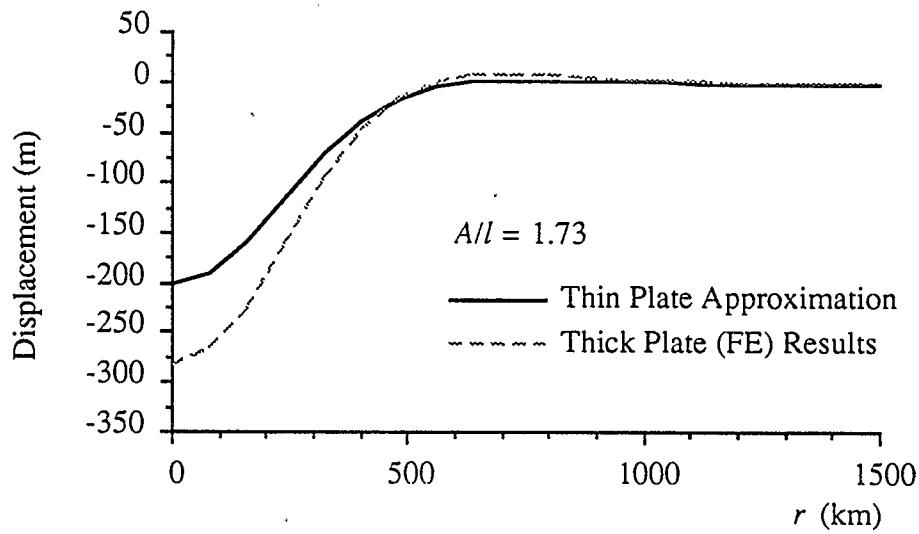

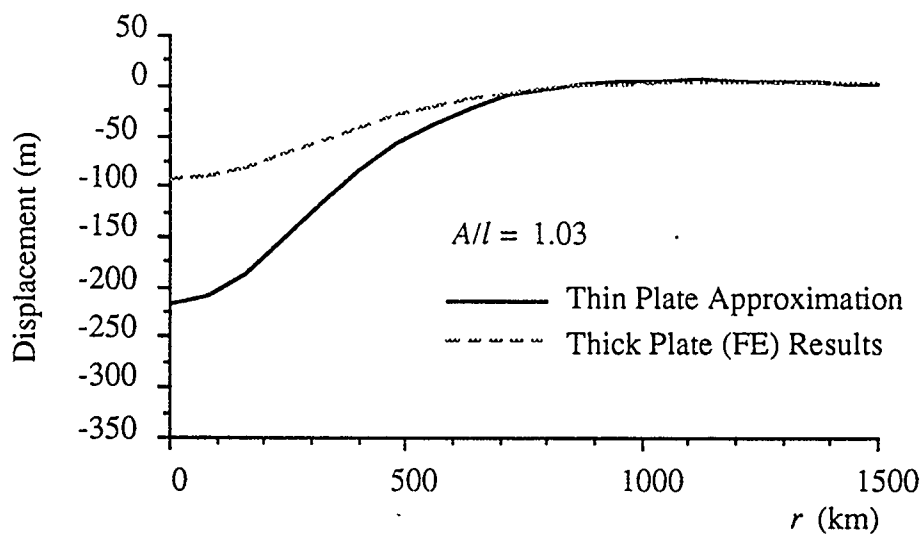

Figure 3.3.3. Comparison of thin plate theory with thick plate modelling for three different lithospheric thicknesses holding all other variables constant [...continued] (Above) Lithosphere is 120 km thick and A/l = 1·73. (Bottom) Lithosphere is 240 km thick and A/l = 1·03.

3.4 Conclusions on the Use of the Finite Element Method

The finite element method was found to work quite well for the cases of an elastic halfspace; a viscoelastic halfspace; and an elastic plate overlying a fluid halfspace. The errors introduced by using this method were no more than 5% for the elastic halfspace and 6% for the viscoelastic halfspace. These maximum errors occurred near the edge of the disc load ($r/A = 1$) for reasons explained below and were significantly less elsewhere. The higher percentage error for the viscoelastic model was attributed to the fact that the model was limited in size and depth with respect to the amplitude of the deformation. Hence, model extent was an important parameter in using the finite element method.

In order for the numerical approximation to work well, it was necessary to choose an appropriate mesh and element size subject to the speed and memory limitations of the computer. In order for the solution to converge, the mesh was chosen to be as uniform as possible with each of the elements being as square as possible. Furthermore, the elements which constituted the mesh were chosen to be sufficiently small. In order to ensure that a finite element solution is acceptable, the finite element code must be run with a progressively finer grid mesh and larger lateral extents until the solution becomes insensitive to these refinements. Elements that are too coarse would have resulted in a poorly interpolated displacement profile across the nodes especially when the deformational gradient is large. It is because of this that the discrepancies between the theoretical and numerical models are large at the edge of the load since the displacement gradient was the highest there.

There is a trade off between (i) an appropriate model extent, (ii) the appropriate element sizes, (iii) the aspect ratio of these elements and (iv) the amount of computer time used in finding a solution. These four factors must be considered before setting up the initial mesh and their contributions weighed against the desired accuracy.

In the finite element program ABAQUS, the accuracy of the solution to the *elastic* loading problem depends on PTOL (Pressure TOLerance) the tolerance on individual force components. Throughout this work, the force tolerance was set to PTOL $\leq 0{\cdot}1\%$ of the total *pressure* exerted by the load. For example, for a load exerting a pressure of $4{\cdot}7\times10^{7}$ Pa acting downwards on one face of an element 50 km in length, the corresponding PTOL value was set to be $2{\cdot}4\times10^{9}$ N. (This corresponded to a tolerance that is $0{\cdot}1\%$ of $4{\cdot}7\times10^{7}$ $Nm^{-1} \times 50{,}000$ m). Small displacement theory, which uses a linear approximation, was used throughout this study. This required that the nodal displacement remain small when compared with the dimension of the element which can be justified in posterior. Large displacement solutions also exist in finite element code.

To solve viscoelastic problems, ABAQUS uses explicit time integration (forward difference) or implicit integration. The accuracies of the *creep* problem depended on PTOL and on the parameter CETOL (CrEep TOLerance) which is the tolerance in creep strain increment during the time period of integration. This creep tolerance was calculated to be about $0{\cdot}1\% \times \dot{\varepsilon}$. For example, using a strain rate of $1{\cdot}5\times10^{-15}$ s^{-1}, which was dependent on the viscosity, and a creep time period T = 10 Ma, a creep tolerance CETOL = 5×10^{-4} (*i.e.* $0{\cdot}1\% \times 3{\cdot}15\times10^{14}$ s $\times$ $1{\cdot}5\times10^{-15}$ s^{-1}) was used. Setting CETOL too small resulted in a failure to converge to a solution within a predetermined number of attempts (in a pseudo-time domain used by ABAQUS) and the program failed to converge and aborted. These values for creep tolerance and creep increment were reasonable and any further refinement did not enhance the results.

In conclusion, the percentage error introduced by using the finite element technique was found to be well within the limits of most of the geological assumptions that were used to create the models (such as estimations of the exact locations of paleo-shorelines, extent and amount of tectonic loads, and the exact stratigraphy, for example). Substantial advantages of using the finite element technique to qualitatively test different geodynamical models included the ability to: use thick plate theory instead of being restricted to thin plate theory; use more complex models not restricted to lateral homogeneity; and test nonlinear rheologies which are becoming

increasingly favourable in current research.

In the following chapter, the finite element method was used exclusively to test various geodynamic deformation cases for true Earth models. As an extention of this work, some of the following models will also utilize lateral heterogeneities that cannot otherwise be modelled theoretically.

"You can kick at the darkness until it bleeds daylight"

Bruce Cockburn (1986).
World of Wonders

4. Flexure of the Lithosphere and Formation of the Alberta Sedimentary Basin

Improved geophysical observations, continuum mechanical modelling, and the application of laboratory measurements of mechanical properties of rocks have led to advances in our understanding of the rheology of the Earth's lithosphere. Oceanic lithospheres are generally better understood than continental, or cratonic, lithospheres because the thickness of the oceanic lithosphere is determined by cooling and this is related to its age. The concept of rigid plates constituting a lithosphere overlying a more fluid-like asthenosphere has been most successful in describing the tectonics of oceanic basins, owing in part to the relatively high strength of the oceanic lithosphere.

Due to the far more complex thermal history and heterogeneous composition of the continents however, significant developments in our understanding of the continental lithosphere remains slow. Simple mechanical plate models employing elastic, viscous, viscoelastic and plastic rheologies have been used to address: subsidence of continental plate margins during rifting and crustal thinning associated with thermal heating and extension (Park and Westbrook, 1983; Braun and Beaumont, 1990); the development of large-scale intracontinental basins (Bills, 1983; Garner and Turcotte, 1984); and the response of the continental crust to vertical loads associated with surface topography including erosion (Stephenson, 1984), fold-thrust belts (Beaumont, 1981), and plate-scale faulting (Owens, 1983). These models of the lithosphere are usually homogeneous and few previous works have addressed the effects of laterally varying lithospheric properties. One of the aims of this chapter is to investigate this lateral variation beneath Western Canada.

4.1 The Cratonic Lithosphere

The lithosphere is defined to be the mechanically strong outer shell of the Earth that can support stresses elastically. It is not to be confused with the *crust* which is a chemically distinct layer. The inferred thickness d of the lithosphere is related to the thickness of the thermal and chemical boundary layers and the duration of the load. The thickness of the lithosphere is mentioned throughout this chapter and will therefore be explained in more detail in this section.

Since viscosity is thermally activated, any vertical variation of the temperature $T(z)$ will give a viscosity profile $\eta(z)$ as (Turcotte and Schubert, 1981):

$$\eta(z) = \eta_0 \exp\left[\frac{(E^* + p\,V^*)}{R\,T(z)}\right] \qquad (4.1.1).$$

In this equation, η_0 is the reference viscosity (*i.e.* the viscosity at a specific depth z_0 by which the viscosity profile $\eta(z)$ is normalized); E^* is the activation energy per mole measured in J mol^{-1}; V^* is the activation volume per mole measured in m^3 mol^{-1}; R is the universal gas constant equal to 8·317 J K^{-1} mol^{-1}; and p is the pressure gradient. The activation energy parameter E^* is usually empirically determined and is ≈ 123 kJ mol^{-1} (granite), 260 kJ mol^{-1} (dolerite), and 523-540 kJ mol^{-1} (olivine) (see Tables 10.1 and 10.2 in Ranalli, 1987). At pressures typical of the upper mantle, the pV^* term is only about 10 to 20% of E^* (Turcotte and Schubert, 1981).

The relaxation time $\tau(z)$ decreases as a function of depth since viscosity and relaxation time are related by $\tau \propto (\eta / \mu)$. This relationship with depth can be seen in Figure 4.1.1. For a load of duration T, the upper part of the Earth that has a relaxation time much longer than T will be seen as the elastic lithosphere. Therefore the thickness of the elastic lithosphere inferred from short period glacial loads (10^3 - 10^4 a) is found to be greater than that inferred from longer term tectonic loads (≈10^6 a). Below the elastic lithosphere, there is a viscoelastic part which initially supports the

load (for time durations < T), but which later on relaxes viscoelastically. The elastic and viscoelastic parts of the lithosphere together define the thickness d of the lithosphere. Below the viscoelastic part lies the inviscid upper mantle whose relaxation time is too short ($\tau_{mantle} \ll T$) to influence the deformation.

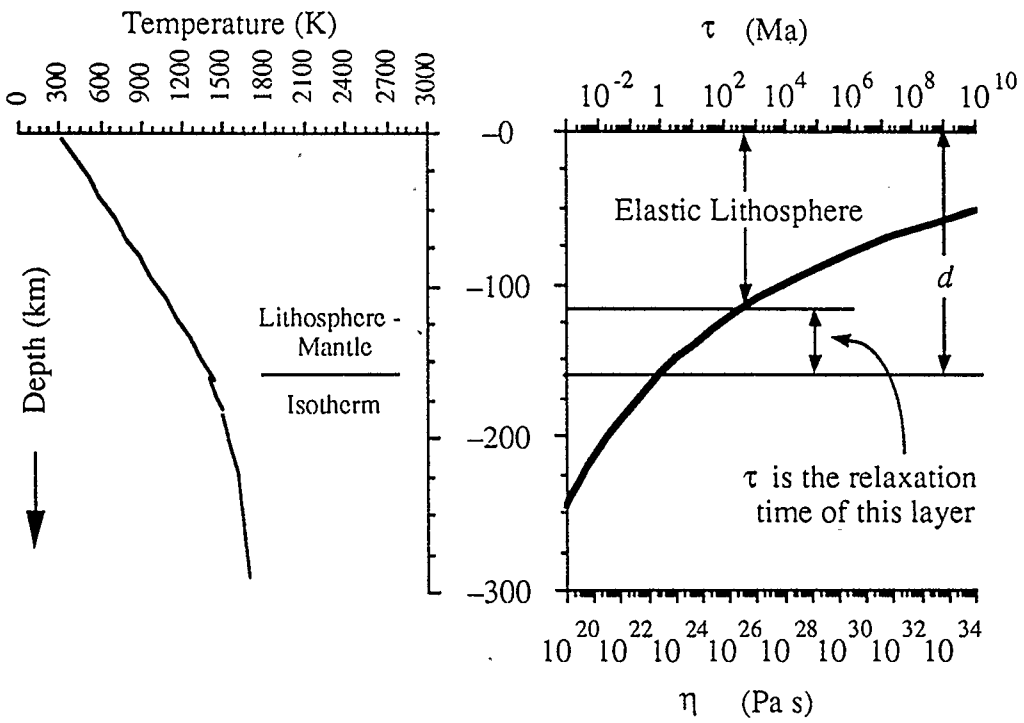

Figure 4.1.1. Plots of temperature (K) and viscosity η (Pa s) or relaxation time τ (Ma) *vs.* depth z (km) with reference to a mantle viscosity of 10^{21} Pa s at 250 km and an assumed geotherm T(z). The *effective* relaxation time of the cratonic lithosphere τ (Ma) depends on the duration of the load and is measured over the viscoelastic portion while the lithospheric thickness d applies to the whole outer boundary.

When there is a lateral change in the temperature profile T(x,z), then there will be a corresponding lateral change in the thickness $d(x)$ of the lithosphere. In order to investigate the lateral changes in the lithosphere, we will parameterize the vertical

variation by an effective thickness d as explained above and an *effective* relaxation time τ which takes into account the viscoelastic portion of the deformation. A plot of this parameterized lithosphere can be seen in Figure 4.1.1 for one particular location.

4.2 Evidence Supporting a Thick Cratonic Lithosphere

There is evidence that the continental lithosphere under North America thickens towards the old craton around Hudson's Bay. This section reviews such evidence using both mechanical evidence and chemical arguments. Finally a link between mechanical and chemical definitions is brought forward.

(a) Mechanical Evidence of a Thickening Lithosphere:

Fulton and Walcott (1975) used glacial loads to infer that the thickness of the lithosphere in British Columbia is about 30 km. Wu and Peltier (1983) however, modelled the relative sea level changes following the last glacial period and concluded that, in order to fit the observed sea level data along the east coast of the United States, the lithosphere has to be close to 240 km thick underneath the craton. Thus one does not expect the same lithospheric thickness on the west and east ends of the North American Plate.

Further evidence supporting a thick cratonic lithosphere comes from secular motion of the Earth's rotational pole (*i.e.* polar wander). Wu and Peltier (1984) pointed out that in order to simultaneously explain the observed speed of polar wander, the free air gravity anomaly and the relative sea level change at the deglaciation centre, the average continental lithospheric thickness has to be close to 200 km.

Glaciers however, have a period of loading of about 1 - 10 ka whereas the period of loading for sedimentary basins is about 10^3 to 10^6 ka. The lithospheric thickness as inferred from the evolution of sedimentary basins is therefore expected to be different.

(b) Chemical (Seismic) Evidence:

Nicholls *et al.*, (1982) studied petrologic variations using xenoliths of ultra-mafic rocks and estimated that the lithosphere beneath the Omineca Core Zone (west of the Rocky Mountain Fold and Thrust Belt) is less than 35 km thick.

There is seismic (chemical) evidence however, that supports a cold and deep *chemical* root lying beneath the North American craton. Using the time differences between the (almost) vertically propagating ScS phase and their multiples, the average traveltimes of shear waves moving vertically through the (old) Pacific Plate were found to be about 4 s greater than the corresponding traveltimes under cratons. This large difference in traveltime could not be explained solely by the presence of a low velocity zone underneath oceans (Sipkin and Jordan, 1980). They concluded that in order to reconcile the ScS data with surface wave data, significant chemical contrasts between oceanic and cratonic lithosphere that persist to depths exceeding 200 km were required.

Another line of chemical evidence comes from three dimensional inversion of surface wave data. Woodhouse and Dziewonski (1984) used these data to construct a tomographic image of the upper mantle. In their models, a fast region below the North American craton is found down to a depth of 350 km and possibly 550 km. This anomously high velocity was interpreted to be due to a cold deep chemical root.

Finally, a deep "chemical root" is also suggested from studies in shear wave splitting of SKS phases. Silver and Chan (1988) argued that the seismic anisotropy that causes shear-wave splitting must be confined to lie near the top 200 to 250 km beneath the North American craton.

It should be pointed out that a deep chemical root does not necessarily imply a thick, mechanically strong lithosphere. However, Jordan (1978), showed that there is a strong correlation between vertical shear-wave traveltimes and mantle heat flow for different types of crustal rocks. This suggests that either the thickness of the chemical root controls the temperature structure of the mantle or *vice versa*. This is also implied by the correlation between the ScS traveltimes and seismic attenuation (Jordan, 1981). Since the mechanical strength of the plate is determined by its temperature profile, the correlation between the thickness of chemical roots and temperature implies that a thick, mechanically strong lithosphere must also exist beneath cratons with thick chemical roots. This tectosphere model proposed by Jordan is consistent with the mechanical evidence presented above.

Having introduced the concept of thickness of cratonic lithospheres and shown some evidence favouring thick, cold cratonic lithospheres, the primary aims of this chapter are to:

(a) refine Beaumont's search for a uniformly-thick lithospheric model to see if the results can be improved in the Alberta Foreland Basin

(b) test whether an eastward thickening lithosphere is able to fit the stratigraphic data given the aforementioned evidence supporting a thick lithosphere.

and, (c) determine which of the two models above has a better fit to the observed data.

4.3 Foreland Basins and the Alberta Foreland Basin

(a) Foreland Basins and Adjacent Orogens:

The characteristic pattern of subsidence, deformation and uplifts of foreland basins has long been recognized qualitatively by geologists. Some classic works describing geological models (see Aubouin, 1965, for a comprehensive review of these ideas) have provided grounds for quantitative modelling. Several studies have been made to date that realize the importance of rigorous modelling (Beaumont, 1981; Cant and Stockmal, 1989).

As pointed out by Price (1973) and modelled by Beaumont (1981), foreland basins form at the site of a downwardly flexed lithosphere in response to passive loading by adjacent supralithospheric mass loads. These tectonic loads may be due to fold-belt thrusting caused by continental collision or accretion of terranes (Cant and Stockmal, 1989). The tectonic loading history may be determined from palinspastic reconstructions of geological cross-sections (Price and Mountjoy, 1970; Bally *et al.*, 1966). Besides the tectonic load, the sediment which fills the foredeep further loads the lithosphere. The amount of sediment however, depends on the amount of flexure which depends on the strength of the lithosphere itself. Schematically, the process of generating a foreland basin is as follows:

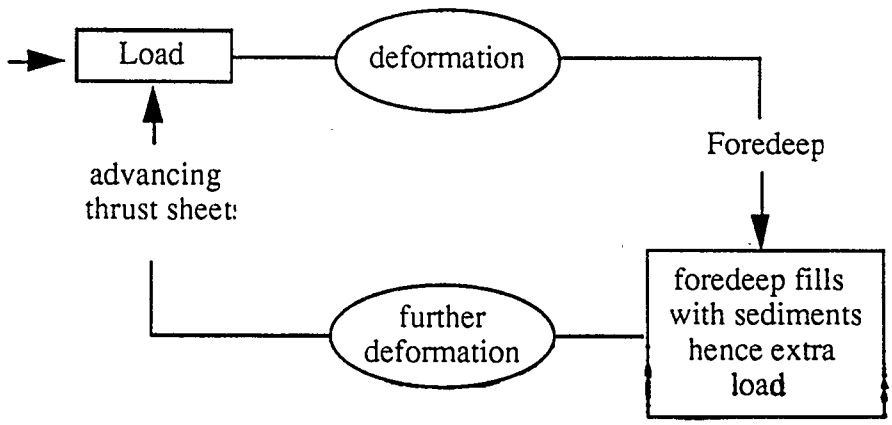

The sedimentation process is an important aspect of the cycle as it provides a *distributed* load throughout the foredeep. Assuming an isostatic equilibrium model, this additional load may increase the total downwarping by 2·5 times (when compared with a similar foredeep filled with water). The sediments which fill foreland basins also result in a stratigraphic record containing the history of the orogen and hence provide a complete coupling between the stratigraphy of the basin and its adjacent orogen. Hence, we are able to deduce the tectonic history and the characteristic properties of the lithosphere from the stratigraphy. In the rest of this chapter we will specifically address the Alberta Foreland Basin and the underlying North American Craton.

(b) Alberta Foreland Basin:

The Alberta Foreland Basin is located on the east side of the Canadian Cordillera. The schematic model depicted in Figure 4.3.1 is the assumed present-day working model for the central part of the Alberta Foreland Basin. The Juan de Fuca

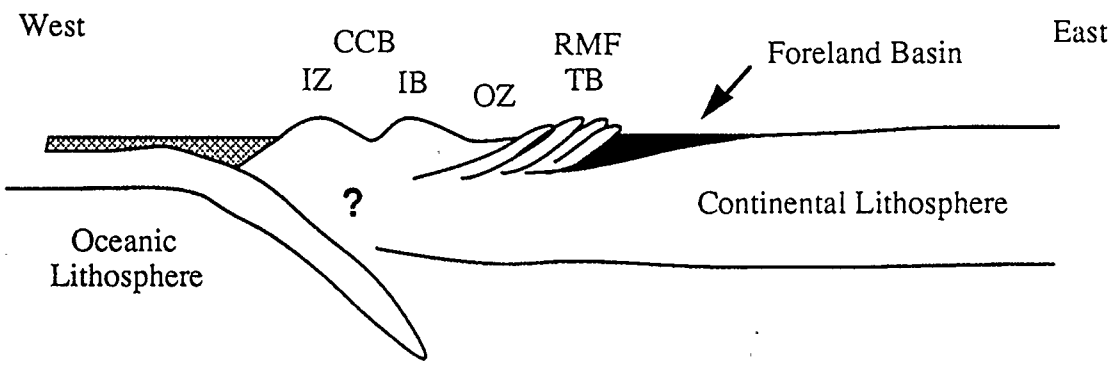

Figure 4.3.1. Conceptual illustration of the present-day Alberta Basin. Subducting oceanic plate produces bathymetry due to thermal uplift (core zone) and a fold-thrust belt west of the foreland basin (foredeep in black). The five zones which comprise the Cordillera are the Insular Zone (IZ), Coastal Crystalline Belt (CCB), Intermontane Belt (IB), Omineca Zone (OZ), and the Rocky Mountain Fold and Thrust Belt (RMFTB).

Plate is subducted beneath the North American cratonic lithosphere causing the trench west of Vancouver Island. The Cordillera is divided into five major zones also shown in Figure 4.3.1. At the west end, where subduction is known to take place, the continental lithosphere is broken and the edge is subject to a counter-clockwise torque produced by motion of the denser plate.

Similar to Beaumont (1981), a cross-section coincident with Gussow's (1962) geological section was chosen for two-dimensional modelling of the Alberta Foreland Basin. The location of the cross-section along BB', shown in Figure 4.3.2, is roughly

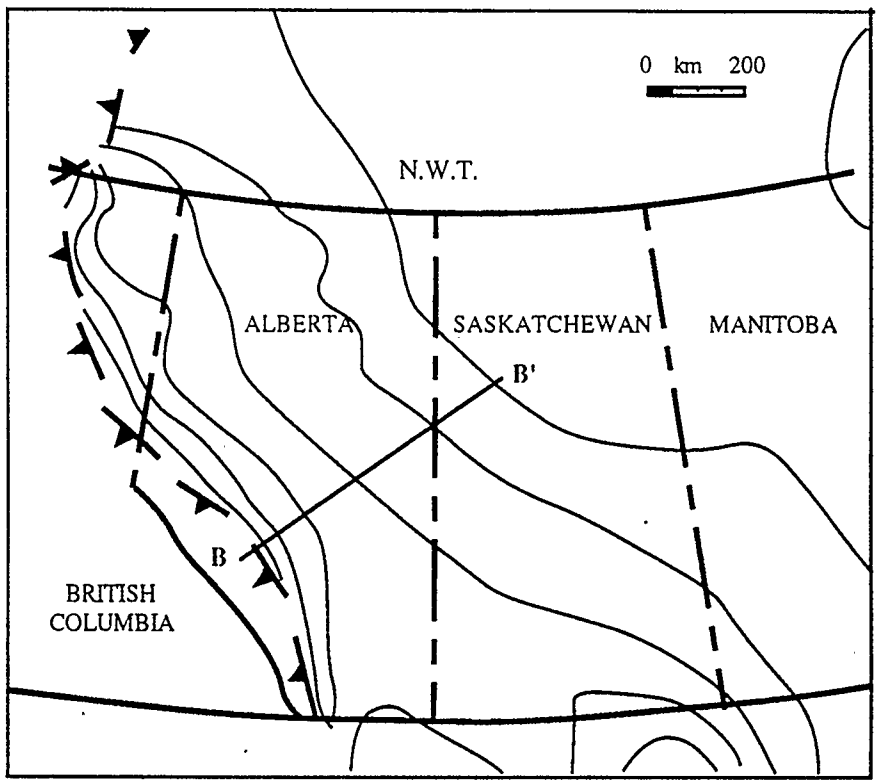

Figure 4.3.2. Location of the cross-section used for modelling the Alberta Foreland Basin. Note that the line BB' is roughly perpendicular to strike. The contours map the Precambrian sedimentary basement at 1000 m intervals (0 m on east end) (after Gussow, 1962).

perpendicular to the edge of the load and is across strike through the depositional basin. The observed cross-section constructed by Gussow and reproduced in Figure 4.3.3 will be used to constrain the load history and the properties of the lithosphere. The subduction zone is at x = 0 km and, proceeding eastwards along BB' (of Figure 4.3.2), the eastern limit of overthrusting is situated at x = 1050 km in the Foothills and the Alberta-Saskatchewan border, or 4th Meridian, was located at 1550 km. The features in Figure 4.3.3 may be divided into *first-order features*, which are defined here to be features primarily caused by the geodynamic deformation process and which are are directly related to the tectonics, and hence the flexure of the foredeep; and *second-order features*, which are defined here to be features that are mainly controlled by the depositional processes.

Three important observations of the geological cross-section in Figure 4.3.3 are described in Table 4.3.1.

---

[i] The depth of the top Jurassic section at x = 1050 km, *i.e.* at the load edge, is about 2400 m below present-day sea level. The depth of the Jurassic at the load edge will be referred to as the amplitude of the load.

[ii] The individual units all dip towards the *west* in the geological section. This implies that a present-day forebulge peak, if it existed, must be to the *east* of x = 1650 km otherwise the units would have an eastward dip.

[iii] The general shape of the Mississippian unconformity is as shown and is a direct result of the flexural response to loading. This flexure is dominated by the first-order effects and is the least affected by the mechanics of sedimentary infilling and erosion.

Table 4.3.1. A list of three important features of the Alberta Foreland Basin taken from Gussow's (1962) geological cross-section. These features were primarily a result of the deformation process and were used as the criteria for accepting or rejecting various models.

It is this flexure which controls the shape of the foredeep that the sediments fill. Note that until deposition of the Paskapoo Formation during the Paleocene stage, the sediments were dominantly marine with the exception of the Upper Colorado Group. Between 1450 km < x < 1650 km in Figure 4.3.3, salt dissolution resulted in the collapse of the Mississippian. This is a second-order geologic feature caused by dissolution of the Elk Point Group evaporites and should not be confused with an eroded peripheral bulge (Meijer Drees, 1986). It is for this reason that it could not be included as one of the tectonically controlled features listed in Table 4.3.1.

Later, it will also be shown that both (a) second-order depositional parameters and (b) the present-day height of the mountains also had to be considered in order to obtain an *acceptable* model.

In this chapter, it will be shown that a uniform model does not satisfy the data as well as an eastward thickening (stiffening) lithosphere using a Maxwell-type rheology. Due to the strong dependence of $\eta(x,z)$ on the temperature $T(x,z)$, an eastward stiffening model is also more realistic since an eastward thickening lithosphere is probably the result of an eastward decrease in the thermal gradient. All the forthcoming models utilize the finite element method described in chapter 3.

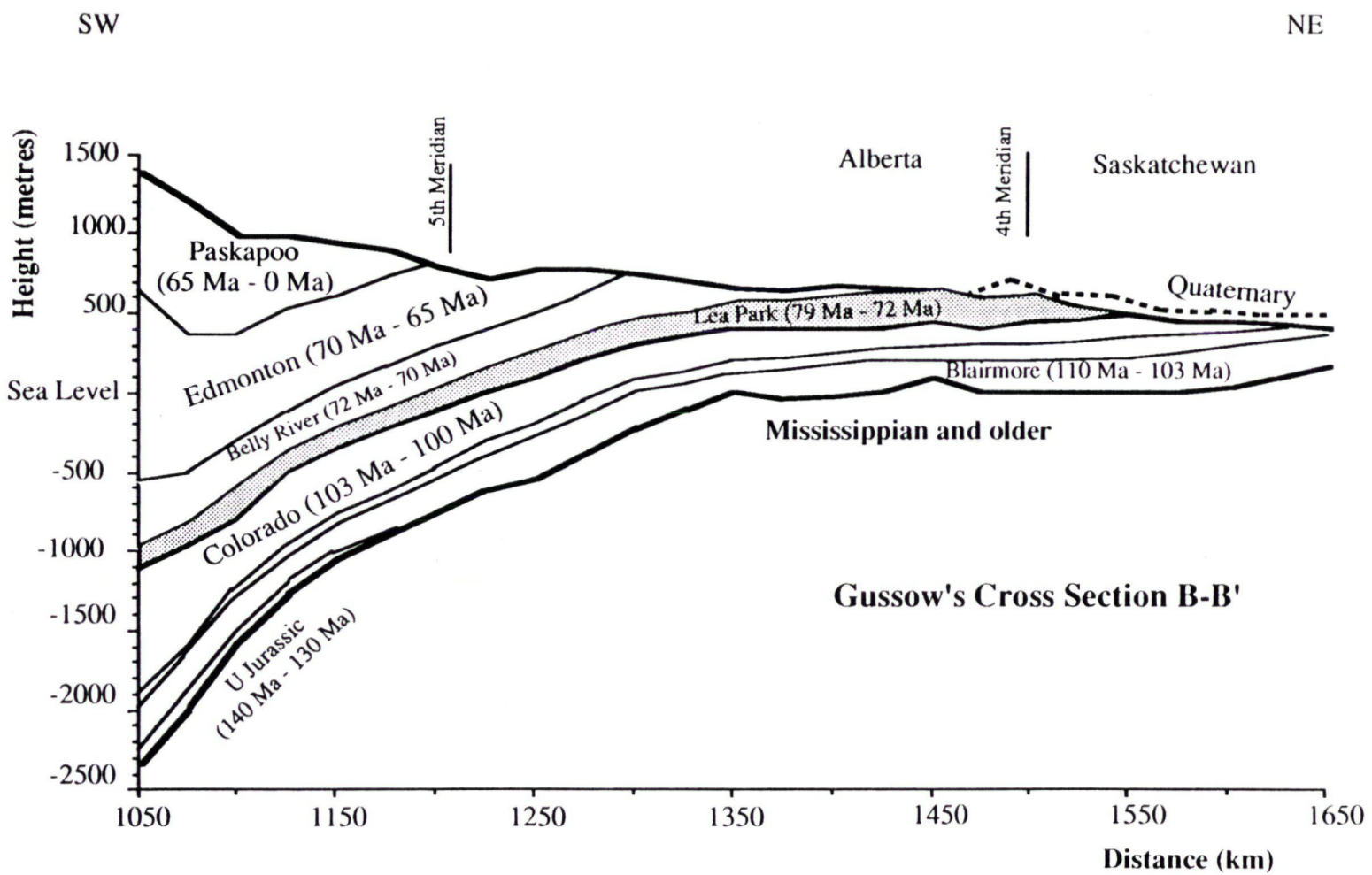

Figure 4.3.3 Reproduction of Gussow's (1962) geological cross section showing the present erosional surface across strike. The stratigraphy is shown along with the estimated ages for each of the horizons. This cross section will be used to compare all results. The Lea Park Formation is shaded in this figure and all following figures for easier comparison.

4.4 The Finite Element Model

The finite element method was used to compute the deformation at the surface by utilizing the tectonic and sedimentary load histories coupled with the lithospheric model. The input is the tectonic load history $L(x,t)$ which corresponds to the advancing imbricate stack sheets during thrusting. The way this input to the model was treated will be explained in section 4.5.

The lithosphere was modelled assuming a Maxwell type viscoelastic rheology parameterized by an effective relaxation time τ. The effective viscosity η is related to the effective relaxation time τ (measured in seconds) by $\tau = 3\eta/E$ Pa s, where a value of $E = 1{\cdot}13\times10^{11}$ Pa (Turcotte and Schubert, 1981) was used for Young's modulus.

The finite element method allowed us to model a *compressible* lithosphere by using a value of $\nu = 0{\cdot}28$ for Poisson's ratio (Turcotte and Schubert, 1981). This value of Poisson's ratio is not inconsistent with the earlier assumption (section 2.2) of an incompressible lithosphere. The assumption that $(\nabla.\mathbf{u})\rho g = 0$ in section 2.2 was required since the finite element method does not automatically account for the buoyancy force term. By choosing a value for $\nu \neq 0{\cdot}5$, a compressible lithosphere (but *without* the buoyancy forces of section 2.2) is implied.

Although some of the beam theory assumptions were valid (*i.e.* deflections remained small when compared to the thickness of the plate; plane sections remained plane after deformation; and the in-plane forces acting on the middle plate were negligible), the assumption that the plate thickness remains much smaller than the characteristic wavelength of the load was not valid during the first three loading steps. Later on it will be shown that the thrust sheets had wavelengths that were *smaller* than a mean plate thickness of 100 km between 140 and 103 Ma. Hence the finite element method was used throughout our modelling.

The lithospheric models were 3000 km in length and varied from 30 km to 300 km in thickness. The finite element mesh comprising these lithospheric models all contained 60 elements horizontally and 8 elements vertically. The elements were two-dimensional plane strain type elements each 50 km in length and with an aspect ratio ranging from 1·3 to 4 (depending on the thickness). The top of the undeformed model, which was initially assumed to be the undeformed Mississippian unconformity, will be referred to as the *baseline*. The baseline corresponded to $z = 0$ m where the z-axis is measured positive in the upward direction. The horizontal, or x-axis, was measured from 0 km at the west end and increased linearly towards the east.

Consistent with geological observations, our lithospheric model was broken at $x = 0$ km at the western edge. This coincides with where the Juan de Fuca Plate subducts beneath the cratonic lithosphere causing it to bend in the anticlockwise sense. This torque gives a moment acting on a thin lithosphere at the site of subduction west of the Insular Zone and which would be incapable of producing any significant deformation to the west of the Rocky Mountains. As a result, the imposed boundary condition was to allow the western boundary to move freely in the vertical direction. Rigid boundary conditions around northern Québec at $x = 3000$ km restrained the eastern side from any vertical or horizontal motion. This distance was considered to be far enough away from the basin so as to not interfere with the deformational processes.

The inviscid upper mantle density was assumed to be $\rho_m = 3400$ kg m^{-3} while the density of the lithosphere was chosen to be $\rho_{litho} = 2400$ kg m^{-3} (Turcotte and Schubert, 1981). It was the density contrast $(\rho_m - \rho_{litho}) = \Delta\rho = 1000$ kg m^{-3} that was responsible for the buoyancy force at the lithosphere-mantle boundary. This buoyancy force was therefore equal to $\Delta\rho g \mathbf{u}_z(x,z)$ where $\mathbf{u}_z(x,z)$ is the vertical component of the displacement at this boundary. The inviscid mantle was modelled by using a Winkler foundation that exerted an upward buoyancy force equal to $(\rho_m - \rho_{litho})\mathbf{g} = 9820$ N m^{-3} multiplied by $\mathbf{u}_z(x,z,t)$, the vertical component of displacement. On the top of the lithosphere there is another buoyancy force. Wherever there was sediment accumulation above the lithosphere, the buoyancy force is proportional to $(\rho_{litho} - \rho_{sed})\mathbf{g} = 0$ N m^{-3}. However, under the load where sediments could not ac-

cumulate, the buoyancy force is $\rho_{litho}\ g\ u_z(x,z)$. Due to the movement of the load, the boundary condition is more complicated and will be discussed in the next section.

To a first-order approximation the basin was assumed to be contemporaneously filled with sediments having an average density of $\rho_{sed} = 2400$ kg m^{-3}. Since the sediments deposited in the foredeep (caused by the input tectonic load) provided an additional

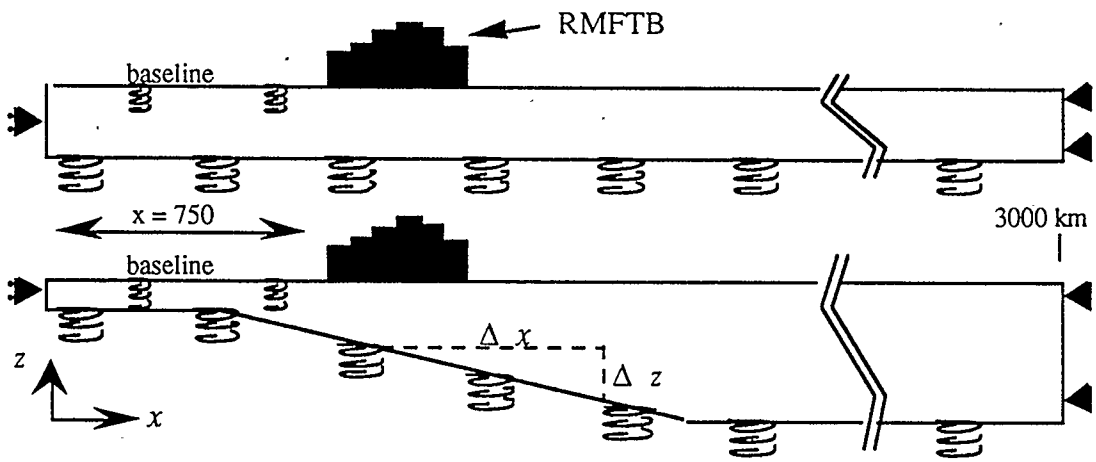

Figure 4.4.1 Two lithospheric models used. [Top] lithospheric model with uniform thickness d and [Bottom] an eastward thickening lithosphere with a slope m of $\Delta z/\Delta x$ measured in m km^{-1}. The boundary conditions are: the broken continental lithosphere on the western edge; the fixed North American Craton on the east; the mantle-lithosphere interface (large springs) on the bottom; and the buoyancy forces due to the lithospheric-sedimentary interface east of the RMFTB (small springs).

distributed load which in turn affected the flexural results, the modelling procedure was clearly non-linear. The Omineca Belt to the west of the load was not filled with

sediments since it was argued that pre-existing topography from uplift in the core zone was sufficiently high to prevent any sediment accumulation. The effects of any sediments that did accumulate however, would have an extremely small effect within the basin (Beaumont, 1981).

Figure 4.4.1 shows the finite element models for a uniform lithosphere having a thickness d [Top] and an eastward thickening lithosphere with a slope of m m km^{-1} [Bottom]. The boundary conditions on the west end, east end and bottom are also shown. The surficial boundary condition was more complicated and will be discussed separately. Table 4.4.1 gives a comprehensive list of the parameters used in all the finite element modelling.

Fixed:	ρ_{sed}	=	2400 kg m^{-3}
	ρ_{litho}	=	2400 kg m^{-3}
	ρ_m	=	3400 kg m^{-3}
	E	=	$1{\cdot}13\times10^{11}$ N m^{-2}
	ν	=	0·25
Variable:	τ_{eff}, d, m, $L(x,t)$		All varied in the parameter search
Dependent:	$\Delta\rho$	=	$(\rho_{litho} - \rho_{sed}) = 0$ kg m^{-3}
	η_{eff}	=	$(\tau_{eff}\ E)/3$ Pa s

Table 4.4.1 Summary of the parameters that were used in the finite element lithospheric models to arrive at a first-order approximation to the Alberta Foreland Basin. The first five parameters were fixed and while the next four parameters were varied in subsequent parameter searches.

4.5 Input to the Finite Element Model

As explained in section 4.3, the lithosphere responded to two types of loads: (i) the advancing thrust sheets known as the tectonic or applied load; and (ii) the weight of the distributed sedimentary deposits that filled the basin.

The applied load can be deduced from a palinspastic reconstruction of the Fold and Thrust Belts (see, for example, Bally *et al.*, 1966, plate 13). Variations of the load in the crystalline core zone (*i.e.* $x < 750$ km) were neglected since the lithosphere could not spread the deformation out towards the foredeep. Deformation inside the basin due to the load outside the Front Ranges is comparatively small (< 5 m). Using beam theory, it can be shown that for a 100 km thick lithosphere, the contribution is small with

$$\frac{w_{700}(1050)}{w_{1050}(1050)} \approx 5\ \%$$

where $w_x(x_0)$ is the displacement at $x = x_0$ due to a unit load situated at $x = \mathbf{x}$ km.

(a) The Applied or Tectonic Load:

Beaumont (1981) divided the applied load into six load columns each 50 km in width. The load was then divided into eleven time steps, the first one starting at 140 Ma which is when the inception of thrusting is believed to have taken place (Dickinson, 1976). Each load column was made up of thrust sheets of a given height assuming an initial average density ρ_L. The heights of the loads can be seen in Table 4.5.1 and were used as the initial input to the models. The horizontal dotted lines delineate the advancing thrust sheets through time and correspond to different orogenic events shown. The different loads were not meant to be interpreted as

individual *sheets* at any particular time but rather the total *weight* for any given time.

Age (Ma BP) \ Load Column	1	2	3	4	5	6
140	2					
130	2					
110	2	1	1			
103	2	1	1			
100	2	3	3			
79	2	3	5	2		
72	2	3	5	2.25	0.25	
70	2	3	6	7.25	4.25	
65	2	3	6	14.25	11.25	6
35	2	3	4.5	6.55	6.15	5.1
15	2	3	2.9	4.55	4.15	3.1
0						

Intermontane Superterrane
Bridge River
Cascadia
Insular Superterrane
Pacific Rim

Time Step	Sediment
1	U Jurassic
2	110 Ma
3	Blairmore
4	L Colorado
5	U Colorado
6	Lea Park
7	Belly River
8	Edmonton
9	Paskapoo
10	Paskapoo
11	Paskapoo

Table 4.5.1 Beaumont's load history $L_l(x,t)$ showing the total height of the load (km) at each of the six load columns *vs* time (Ma). The dashed lines delineate the eastward advancing thrust sheets and correspond to significant orogenic events throughout time.

Note that the characteristic wavelength of the applied load in Table 4.5.1 is between 50 km and 300 km. Assuming a 100 km thick uniform lithosphere and the values shown in Table 4.4.1, a flexural rigidity of D = 10^{25} N m corresponding to a radius of relative stiffness of $l \approx 180$ km is implied. This gives values of $0{\cdot}3 < A/l < 1{\cdot}7$ during all loading time steps. In section 3.3 however, it was shown that in an axisymmetric coordinate system the thin plate approximation holds for values of $A/l \geq 4$. Since l_{2D} =

$\sqrt{2}\,l$, then the thin plate approximation holds for $A/l_{2D} \geq 5{\cdot}5$ for this problem. Hence the thin plate approximation is not valid in this problem.

(b) The Distributed Sedimentary Load:

Deposition of the sediments was assumed to fill up to the baseline in the finite element model as flexure occurred. This was only an approximation however, since it was recognized that the actual baseline did not remain constant through time. The extra sediment load due to the change from the fixed baseline to the new baseline could be divided into (i) a uniformly thick package between the two baselines, and (ii) a small wedge of sediments above or below the new baseline. These two regions are illustrated in Figure 4.5.1.

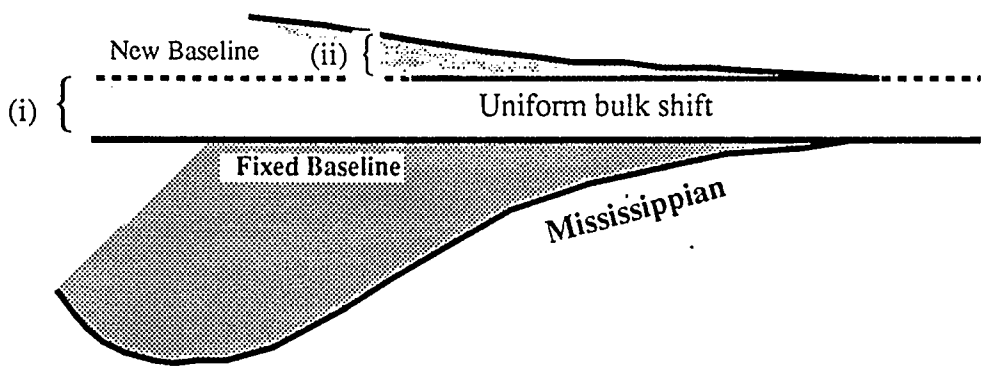

Figure 4.5.1. Effect of second-order sediments caused by eustasy and terrigenous deposits. Sedimentary deposits placed in region (i) result in a uniform load that contributes to a uniform bulk shift while sediments in region (ii) are relatively small and can be ignored.

The sedimentary load in region (i) is uniform and results in a uniform bulk shift in

displacement while that in region (ii) is small and was ignored.

Modelling the sedimentary load to properly establish the boundary condition at the surface was more complicated and was divided into three regions. The first region corresponded to the surface *west* of the RMFTB, the second corresponded to the surface *beneath* the advancing RMFTB and the third corresponded to the surface *east* of this applied tectonic load.

The first region was situated west of the RMFTB (*i.e.* 0 km < x < 750 km). It was assumed that no sediments were deposited in this region and hence this surface was modelled using a Winkler foundation with an upward buoyancy force of $\rho_{litho}\, u_z\, \mathbf{g}$. In the distal portion of the basin east of the present-day load edge (the third region defined by x > 1050 km) however, sediments were coevally deposited and this region was modelled using a Winkler foundation exerting a (restoring) buoyancy force of $\Delta\rho u_z\, \mathbf{g}$ in the upward direction where $\Delta\rho = (\rho_{litho} - \rho_{sed})$. Hence when flexure occurred at any time step, the foredeep was automatically filled up to the baseline with sediments having an average density of 2400 kg m^{-3}.

Beneath the advancing load in the second region, defined by 750 km < x < 1050 km, the boundary conditions varied temporally as the thrust sheets advanced. Consider Figure 4.5.2 which shows the load advancing over node **2** at three consecutive time steps labelled *A* - *C*.

During time step *A* node 2 was in the distal portion of the basin because the tectonic load M_1 lies to the left of node **1** and sediments were simultaneously deposited on either side of node **2**. Hence the buoyancy force at node **2** was proportional to $\Delta\rho\mathbf{g}$ acting in the upward direction.

At time *B*, the tectonic load has advanced to node **2**, so sediments are still being deposited to the right of node **2** and the applied load *plus* the previously deposited sediments sit on the left of node **2**. The forces acting on this node were an upward buoyancy force equal to $\frac{1}{2}\rho_{litho}\, u_z\, \mathbf{g}$ due to the sediments on the left plus $\frac{1}{2}\Delta\rho\, u_z\, \mathbf{g}$ =

0 N due to the sediments on the right counteracted by a force of $\frac{1}{2} M_2{}^*g$ due to the total load on the left. $M_2{}^*$ is used to denote the tectonic load of mass M_2 (as shown in the load history table) *plus* the load due to the sediments that were deposited over half that element at time *A*.

Finally, at time *C*, an advancing tectonic load of mass M_3 has completely covered the sediments that were deposited at times *A* and *B* to the right of node **2**. These

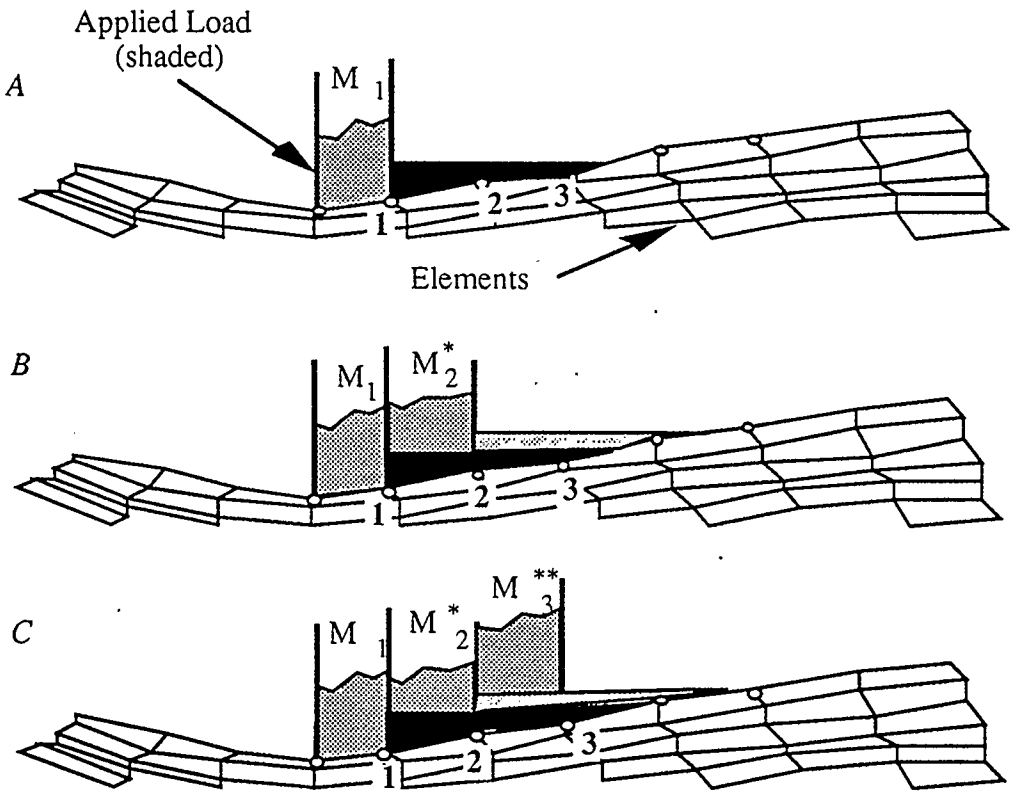

Figure 4.5.2. Three time steps as the thrust sheet advances. Node **2** has different buoyancy forces acting on it for each time step as explained in text. Time *A*: node **2** has sediments on either side. Time *B*: node **2** bears an applied load on one half and buoyancy forces (sediment load) on the other half. Time *C*: node **2** is beneath the applied load.

sediments thus became part of the total load M_3**. Hence, by the work-load equivalent method, the forces acting on node **2** are $\frac{1}{2}(M_2{*}+M_3{**})\mathbf{g}$ counteracted by a buoyancy force equal to $\rho_{litho}\, u_z\, \mathbf{g}$.

Therefore, using the loading history *L(x,t)* as the input to the model described in section 4.4, the output of the finite element modelling procedure gives both the deformational history through time and the approximate sedimentary load for any given lithospheric model. This approximate sedimentary load also gives a first-order stratigraphic model where the term first-order is used to indicate only those factors which influence flexure.

4.6 Accommodation Control

So far we have discussed a lithospheric model having an associated foredeep that is assumed to be completely filled with sediments (*i.e.* up to a fixed baseline) for each of the units corresponding to the eleven time steps. As pointed out by Beaumont (1981) however, second-order parameters significantly affect the depositional history and must also be taken into account. The above simple sedimentation model therefore, was too restrictive to be realistic. Since the flexure gives a first-order estimate of the thickness of each formation, by incorporating second-order effects such as eustasy, incomplete deposition, compaction and partial erosion, we can produce a more realistic depositional model. This section deals with the input to such a model and a detailed explanation of each of the four parameters.

(a) Eustatic Sea-Level Variations:

Eustasy affected the depositional history during times when the basin was connected to open seaways and hence marine deposition occurred. The algebraic sum of tectonic subsidence, due to lithospheric flexure and computed by the finite element model, plus the eustatic changes in sea level provide the amount of *accommodation* or total "space available" for depositing acquatic sediments.

The relative changes in sea level are small when compared to the flexure immediately adjacent to the load but become increasingly important in the distal portion of the basin where eustatic variations are comprable to the amount of flexure. The eustatic

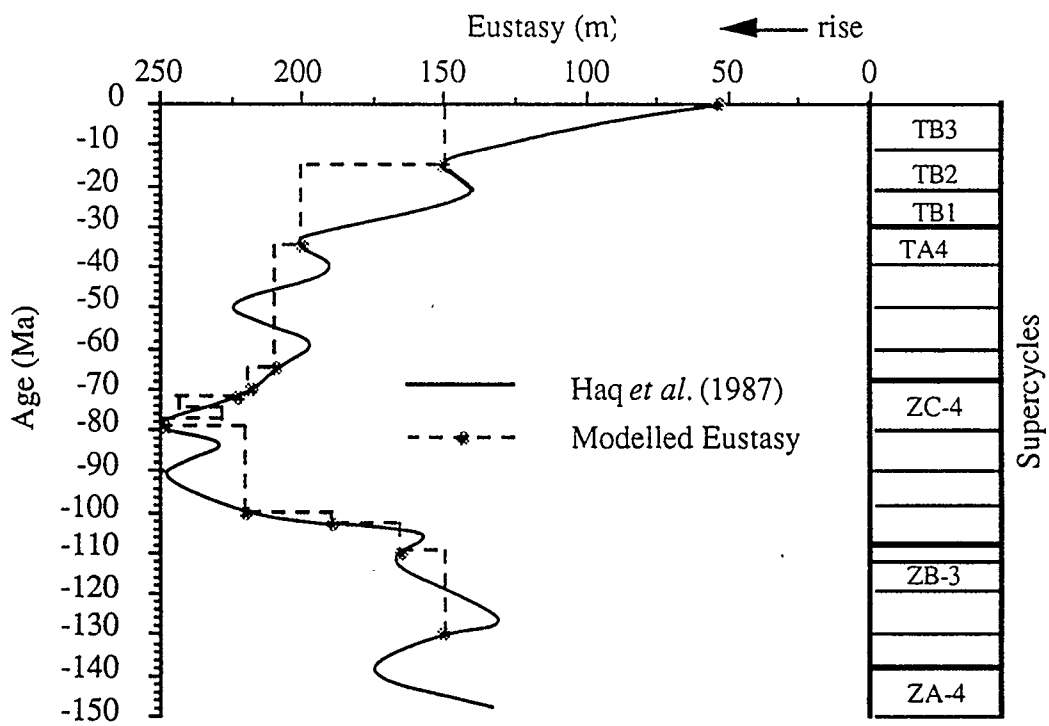

Figure 4.6.1. First-order (megacycle) and second-order (supercycle) eustasy curves. Megacycles are to the order of 65 Ma (Tejas) and 90 Ma (Zuni) and supercycles are to the order of 10 Ma (TB3 and ZC-4). Third-order cycles have a period of < 4 Ma and are not included here except for ZC-4.4 at 73 Ma during Maastrichtian time.

curve, modified after Haq *et al.* (1987), was "blocked" into the same eleven time steps used for the loading history in Table 4.5.1. Figure 4.6.1 shows the eustatic variations after Haq *et al.* along with the blocked curve (dashed line) used in our model. The names of the corresponding supercycles are given in the right-hand column for reference. Notice that only the supercycles were considered except at 73 Ma where the ZC-4.4 (a third-order cycle), was necessary to explain the fit to the observed stratigraphy at Maastrichtian time.

(b) . Incomplete Basinal Deposition and Secondary Sources:

A starved basin due to incomplete deposition was modelled to occur if the time period between successive loads was considered to be too short to fill the additional space available. This was not only reasonable but necessary since some seaways such as Bearpaw (the last marine incursion) between 76 Ma and 72 Ma were as deep as 100 to 200 m in places and it is not conceivable that they were ever completely filled (Hills, L.V., *pers. comm.*, 1989). Although the main sediment supply was from the west, progradation of some marine deposits was also allowed to come in from the east. The Lea Park is an example where a secondary source allowed clastic sediments to prograde from the east but not extend all the way to the west.

(c) Partial Erosion:

Partial erosion was the third parameter included in our model. Although partial erosion is geologically quite different from *incomplete deposition*, it was mathematically treated in a similar way. Partial denudation of the sediments lying above the paleosea-level was assumed in the depositional spreadsheet. As for the case of sedimentary deposition however, these weathered sediments were not always completely eroded (consider, for example, present-day Alberta and Saskatchewan which have an erosional surface above present-day sea-level).

(d) Compaction of Sediments:

Physical models for compaction were the most subjective of the parameters included in our model. This was due to the fact that a time-dependent physical model that explains compaction of sediments at depth could not be invoked without making additional assumptions with respect to facies. The net effect of compaction however, could be considered together with partial erosion. For our purposes, a model that expresses an isopach thinning due to partial erosion is formally identical to one that is explained by compaction. The simple manner in which compaction was treated therefore, was to assume that the sediments were proportionally compacted as a function of their thickness.

These four secondary parameters were used in a spreadsheet to arrive at an acceptable depositional model. The net effect of incorporating these second-order parameters, was to fine-tune the thicknesses of the individual units. Given that these thicknesses are correct, then the location of the outcrops and the angles of dip of these units were not controlled by the accommodation model but rather by the flexure.

Having established a finite element model with the appropriate boundary conditions and a depositional model using this spreadsheet, and using the loading history as the input to the working model, we can proceed with our first objective which was to refine Beaumont's model using the above improvements.

4.7 Uniform Lithospheric Models

Beaumont (1981) used the thin plate approximation to model the flexure of a uniformly thick viscoelastic lithosphere which overlies an inviscid asthenosphere (or upper mantle). In his model, which was based on the analytic solution to the flexural problem, the plate was assumed to be incompressible and infinitely long in either direction with fixed boundary conditions at $x = \pm\infty$. His best lithospheric model was found to have a relaxation time of 27·5 Ma with a flexural rigidity of $D = 10^{25}$ N m. This flexural rigidity implied a thickness of $d \approx 100$ km when values of $1{\cdot}15\times10^{11}$ N m^{-2} and 0·5 were used for Young's modulus and Poisson's ratio respectively.

In this section, Beaumont's model is first reproduced using the finite element model described earlier along with the boundary conditions discussed in sections 4.4 (west, east, and bottom) and 4.5 (surface). Beaumont's parameter search is then refined to produce a uniform lithospheric model that more closely matches Gussow's observations. This refined uniform lithospheric model will be subsequently used to compare with an eastward-thickening lithospheric model.

The stratigraphy in these models was generated using the spreadsheet described in section 4.6. It was recognized however, that (a) the position of the present-day sea level with respect to the Mississippian "baseline" was not known and (b) the eustasy curve itself has limited accuracy. Consequently, the results of the initial models were subjected to vertical shifts of up to 250 m either way (the maximum amplitude of the eustasy curve over the last 140 Ma) and the true location of the zero crossing of the peripheral bulge (with respect to sea level rather than the baseline) was not definitively known (although the point at which the dip of the units changed direction going from west to east was observable). The spreadsheet therefore also allowed for such a vertical bulk shift so that the Mississippian at $x = 1500$ km matches the observed height of the present-day erosional surface in Gussow's section.

The predicted stratigraphy reproduced using the finite element model and aforementioned spreadsheet, is shown in Figure 4.7.1. The model was adjusted by lowering the sea level down 400 m with respect to the baseline in order to better match the amplitude at the load edge (the deformation at x = 1050 km was –1705 m with respect to the baseline). This adjustment results in a poor fit in the height of the Mississippian unconformity for x > 1500 km.

When compared to Gussow's (1962) geological cross-section (Figure 4.3.3), certain inadequacies of the model in Figure 4.7.1 immediately become apparent. Firstly, the locations of the outcrops in the model are too close to the mountain range which means that the predicted present-day forebulge is closer to the load than what is actually observed. This implies that the value of the flexural rigidity is too small since the location of the forebulge is directly related to the flexural stiffness (see Figures 2.6.1 and 2.6.2). Secondly, towards the east, close to the Alberta-Saskatchewan border (4th Meridian), the modelled horizons dip eastwards. This again is due to the fact that we are on the other side of the peak of the peripheral bulge and all formations dip eastward. This is contrary to the observation where all formations dip to the west and a stronger lithosphere would spread the deformation further from the load. Again this implies that this model of the lithosphere is too thin and weak.

Figure 4.7.2 shows the burial history at the load edge at x = 1050 km, and at the 5th and 4th Meridians respectively. The deflection to the right of the dashed line corresponds to a positive deflection with respect to the z = 0 fixed model baseline. The profiles at the load edge and the 5th Meridian show that between 140 Ma < t < 35 Ma there was an increasing burial of sediments followed by uplift between 35 Ma < t < 0 Ma. At the 4th Meridian however, the sediments were found to remain close to the surface (to within ±250 m). When combined with the thermal history of the basin, this burial information can be used to estimate the level of organic metamorphism (LOM) of the source-prone sediments.

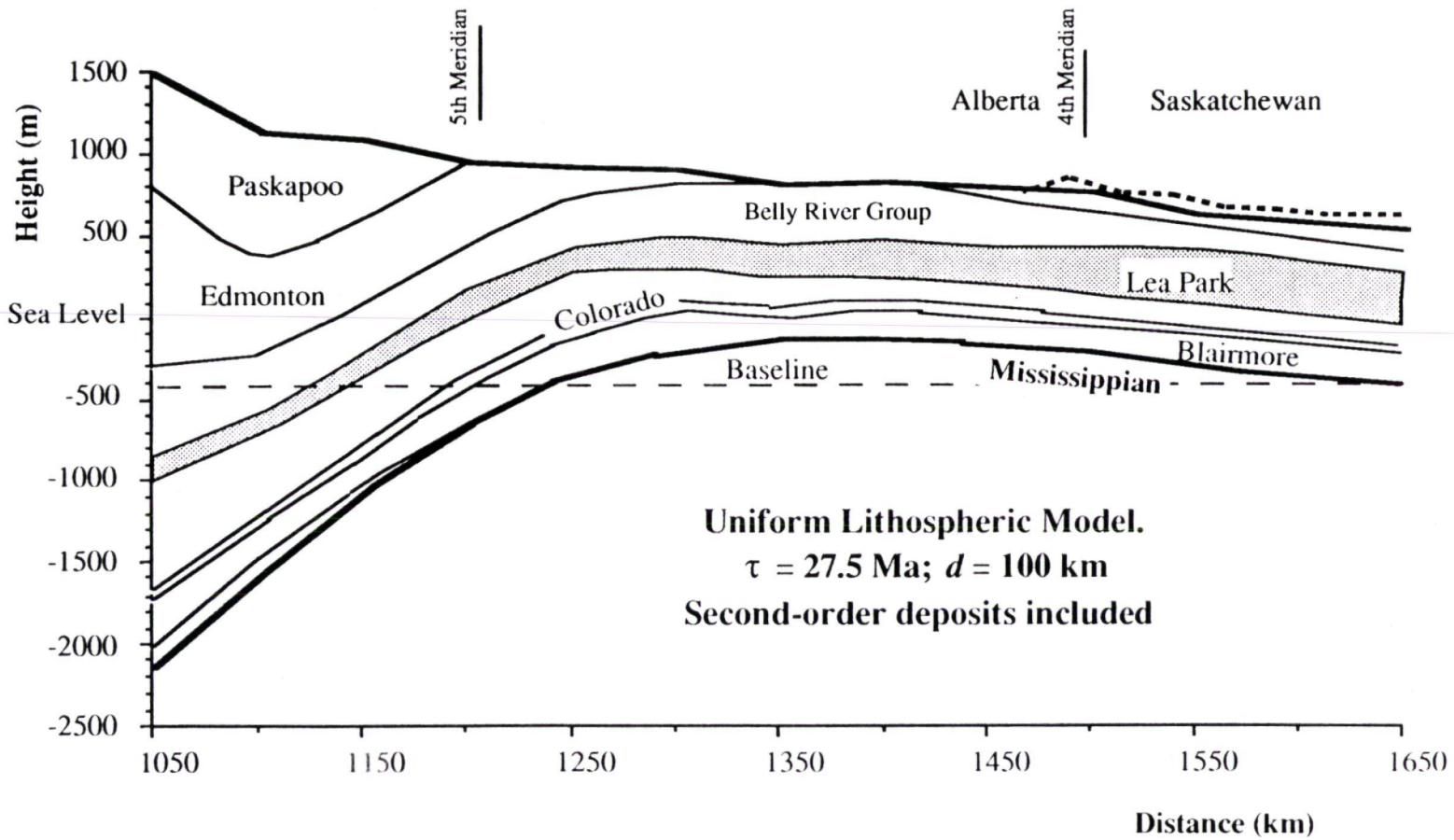

Figure 4.7.1. Reproduction of Beaumont's (1981) best model but using finite elements and improved boundary conditions. The units have approximately the correct thickness but the wrong shape. The outcrops are in the wrong location and the units incorrectly dip eastward at the Alberta-Saskatchewan border. The model predicts the existence of a prominent peripheral bulge too close to the mountains (compare with Figure 4.3.3).

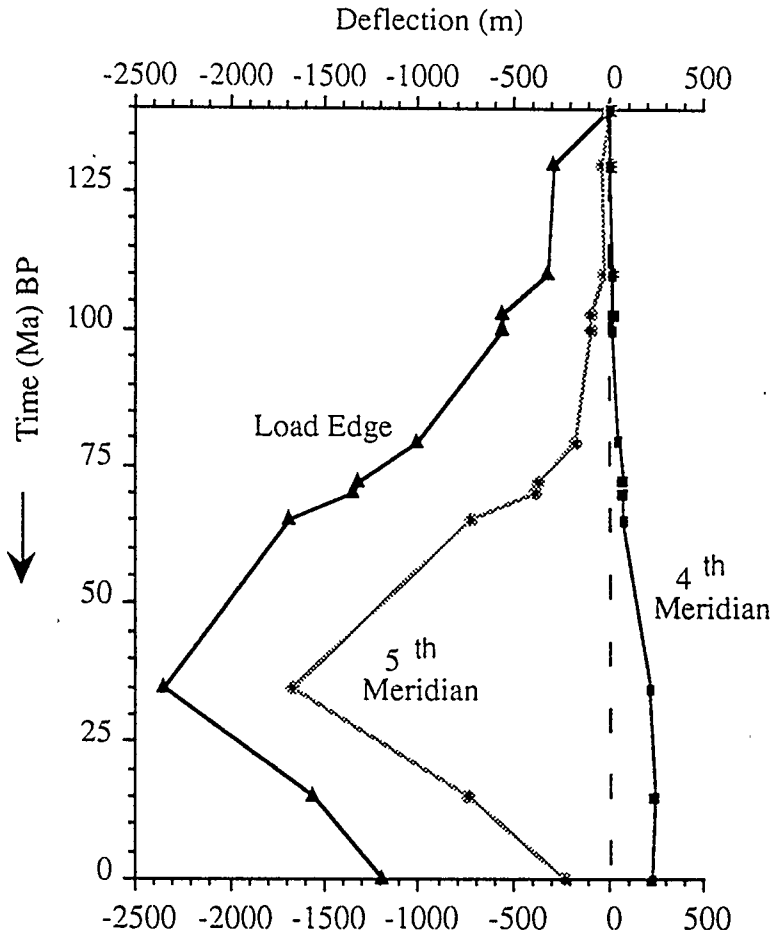

Figure 4.7.2. Temporal flexure of the surface of the lithosphere using Beaumont's (1981) model. The curves, which correspond to the edge of the load, the 5th Meridian and the 4th Meridian (the Alberta-Saskatchewan Border), show the rate of burial with respect to the baseline at these three locations.

4.8 Search of Uniform Lithospheric Models.

From the results of the last section, it was clearly shown that the lithospheric model having a value of $\tau = 27{\cdot}5$ Ma and $d = 100$ km is too weak. In order to determine a better uniform lithospheric model for the Alberta Foreland Basin, a systematic search of various parameters was made. In the parameter search of this new lithospheric model, the variables involved were: the effective relaxation time τ of the viscoelastic lithosphere as described previously; the lithospheric thickness d; and the loading history $L(x,t)$. The parameter search attempted to match the present-day Mississippian since it was not affected by secondary sedimentation processes such as the overburden.

(a) Parameter Search in d-τ Space:

Assuming a uniform lithospheric model for the moment, a search in d-τ space was first attempted. Given an initial lithospheric thickness of $d = 100$ km and Beaumont's load history $L_1(x,t)$ as described in Table 4.5.1, several models with different relaxation times were generated. Figure 4.8.1 shows the results of varying the relaxation times when the predicted shape of the Mississippian is compared to the observed (Gussow's section). The models with a relaxation time $\tau < 50$ Ma predicted a final Mississippian that was too weak with a prominent peripheral bulge well within the basin ($x < 1500$ km). They clearly did not match the observed Mississippian in Gussow's section. Models with $\tau > 100$ Ma predict a peripheral bulge that is east of $x > 1650$ km however, they were too stiff and did not correctly match the gradient between 1050 km $< x <$ 1250 km. This can be seen for the model with $\tau = 125$ Ma where a change in the load would adjust the amplitude at $x = 1050$ km but would not improve the deflection profile. Relaxation times bracketed by 50 Ma $< \tau <$ 100 Ma were hence used as an approximate match to the observations from Gussow's section. The uniform model with $\tau = 75$ Ma matched the data quite well between 1150 km $< x$

< 1450 km. A suite of uniform models was then generated for various thicknesses d using τ = 75 Ma. Figure 4.8.2 shows the flexure results for three thicknesses between

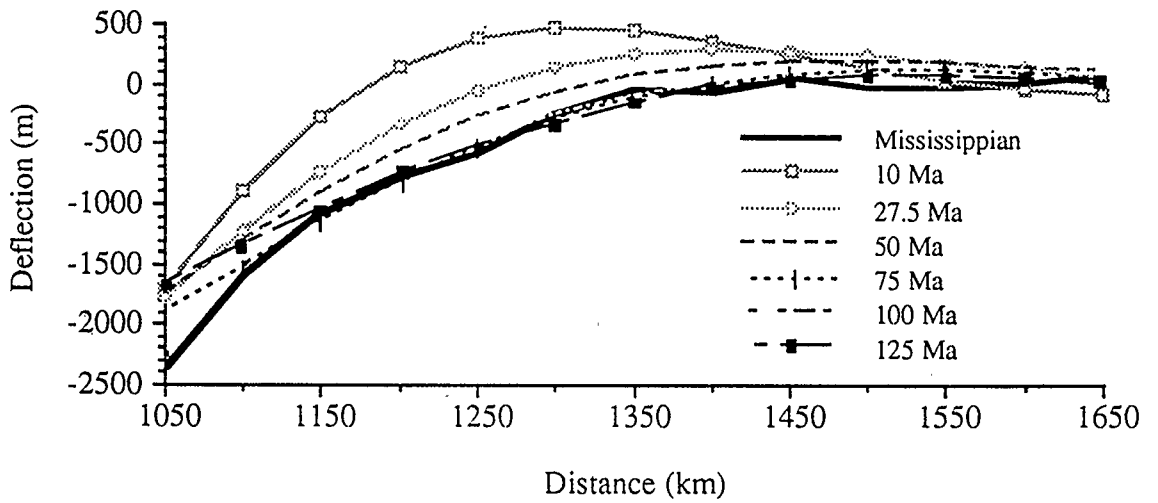

Figure 4.8.1. Plots showing results of varying τ for a uniformly thick lithosphere with d = 100 km. The observed Mississippian is shown in bold solid line. There was a best match by the model with τ = 75 Ma. Note that while the amplitude at x = 1050 km was not affected by varying τ, the gradient of the Mississippian was affected significantly.

50 km < d < 150 km. It was evident that for lower values of d, the flexural model predicted a significant peripheral bulge that was too close to the load. Thus, a thin (weak) lithosphere behaved in the same way as one with low values of τ. Increasing the value of $d \geq$ 150 km however, resulted in insufficient flexure throughout the foredeep. This was the result of a mechanical lithosphere that was too strong. A value of d = 100 km provided a good first-order fit to the present-day Mississippian. Nonetheless, some discrepancies in amplitude were evident at x < 1150 km near the load edge. Note that the peak of the forebulge still lies within the Alberta Foreland Basin.

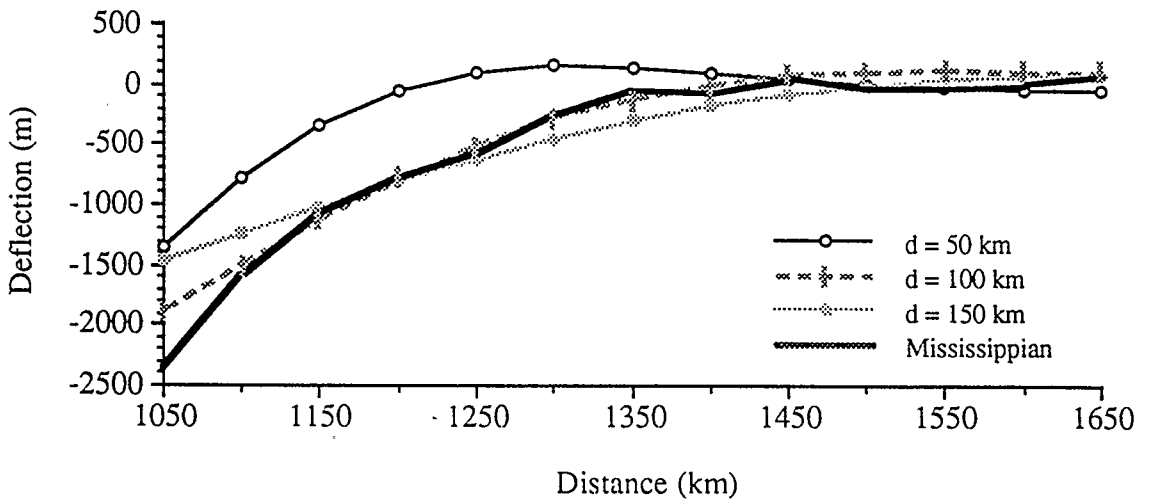

Figure 4.8.2. Thickness search using τ = 75 Ma and various values for *d*. The best value for *d* was found to be 100 km (thick dashed). There is still an amplitude discrepancy at the load edge that is largely controlled by the load history. The Mississippian from Gussow's section is shown in bold.

The results of Figure 4.8.1 and 4.8.2 are summarized in the d-τ space in Figure 4.8.3. All values that mapped *outside* the hatched lines in this d-τ domain would result in a worse fit than the d = 100 km, τ = 75 Ma model and were immediately ruled out. Models within this d-τ domain having a short τ and/or small d value (*i.e.* the lower left-hand quadrant), did not match observations between 1150 km < x < 1450 km. Those models in the long τ and/or thick d region (upper right quadrant) provided an ill fit for x < 1150 km and x > 1450 km. For those models between the hatched lines, there are still some mismatches, namely the difference in the amplitude of the deformation near the edge of the load at x = 1050 km. Since the magnitude of this amplitude is mainly controlled by the applied or tectonic load, a search in $L(x,t)$ space was then performed.

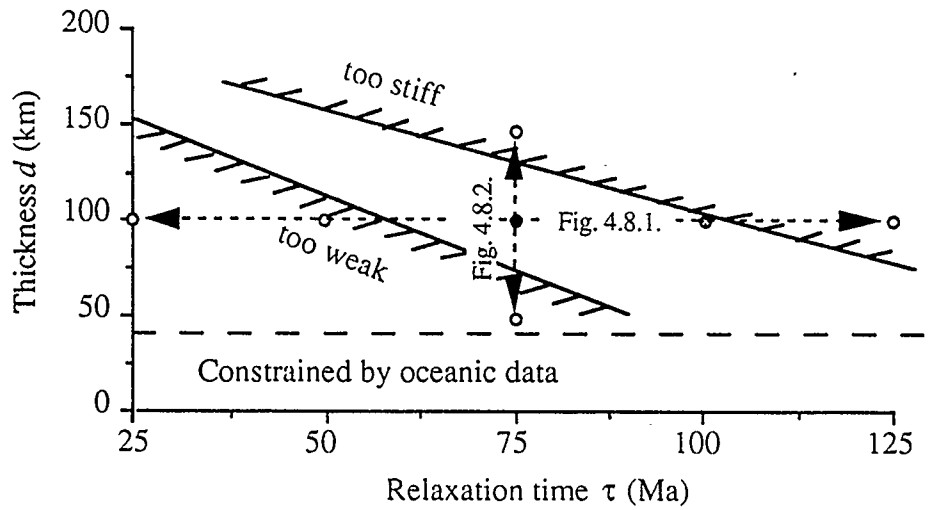

Figure 4.8.3. d-τ search space showing the best models using *uniform* lithospheric models. The schematic shows ranges of the lithosphere modelled with d = 100 km while varying τ and models with τ = 75 Ma while varying d. These models gave results that only satisfied *some* of the criteria. For shortcomings of the models within this domain see text.

(b) Load L(x,t) Search:

The next logical step in the analysis was to try and find an appropriate load history $L(x,t)$ so that the discrepancies in the amplitude will be minimized. A load model which gives an acceptable deflection of the Mississippian at the load edge (*i.e.* ≈ 2400 m below sea level) was sought. This was accomplished by adjusting the *heights* of the loads but staying within the error bar limitations placed by Beaumont (Beaumont, 1981, obtained the correct mountain height). The load search consisted of $L_1(x,t)$, which was the same as the load history defined in Beaumont's (1981) paper, as well as five additional load histories labelled $L_2(x,t)$ through $L_6(x,t)$. The definitions of these load histories are given in Table 4.8.1 below:

The results of using some of these load histories with a uniform lithospheric model

that was 100 km thick and with a relaxation time of 75 Ma are shown in Figure 4.8.4 for loads $L_1(x,t)$ and $L_4(x,t)$ - $L_6(x,t)$. Loads $L_2(x,t)$ and $L_3(x,t)$ were very similar to

---

$L_2(x,t)$: Same as Beaumont's load history $L_1(x,t)$ defined in Table 4.5.1 except that at time step 9, load 6 was changed from $9{\cdot}41\times10^7$ Pa to $1{\cdot}41\times10^8$ Pa. This extra $4{\cdot}70\times10^7$ Pa was left on until step 11 where $2{\cdot}35\times10^7$ Pa were removed. The overall height of load column 6 was increased by 1 km when using densities from Beaumont's load history.

$L_3(x,t)$: Same as above except that at time step 7, load 5 was changed from $5{\cdot}88\times10^6$ to $7{\cdot}64\times10^7$ Pa. The load causing this extra pressure was left on until step 11 where it was then eroded. The overall height of load column 5 remained the same as $L_1(x,t)$ but column 5 was still higher as was the case in $L_2(x,t)$.

$L_4(x,t)$: $4{\cdot}70\times10^7$ Pa were added to $L_2(x,t)$ at load column 6 between 35 Ma and Present.

$L_5(x,t)$: $4{\cdot}70\times10^7$ Pa were added to load columns 4 and 5 from 65 Ma to Present and another $4{\cdot}70\times10^7$ Pa were added to load column 6 from 35 Ma until Present.

$L_6(x,t)$: $3{\cdot}53\times10^7$ Pa were added to load columns 4 and 5 from 65 Ma to Present time and $3{\cdot}53\times10^7$ Pa added to load column 6 from 35 Ma to Present.

Table 4.8.1. Modified tectonic or applied load histories $L_1(x,t)$ to $L_6(x,t)$ showing the various changes in the applied load used by Beaumont (1981). These load histories were used in the load search in order to produce the correct amplitude of downwarp close to the mountain edge at x = 1050 km.

Beaumont's $L_1(x,t)$ load and could not be discerned on this plot scale. Load history $L_6(x,t)$ resulted in a deflection of 2350 km at the load edge while $L_4(x,t)$ resulted in a

deflection of 2045 km and $L_5(x,t)$ deflected the Mississippian by 2563 km at x = 1050 km. Variations in the load were found to control the amplitude but did not change the overall shape. Note how the general profile for all loads remained reasonably intact for large x with the largest departure at x = 1050 km. Table 4.8.2, shows the load history $L_6(x,t)$ chosen from the load parameter search since it best matched the amplitude at the edge of the load. The load values that differ from Table 4.5.1 with Beaumont's $L_1(x,t)$ load history are shown in bold in Table 4.8.2. Although this load is heavier overall, it will be left until later to show whether this load satisfies the observed gravity profile of the present-day mountain height.

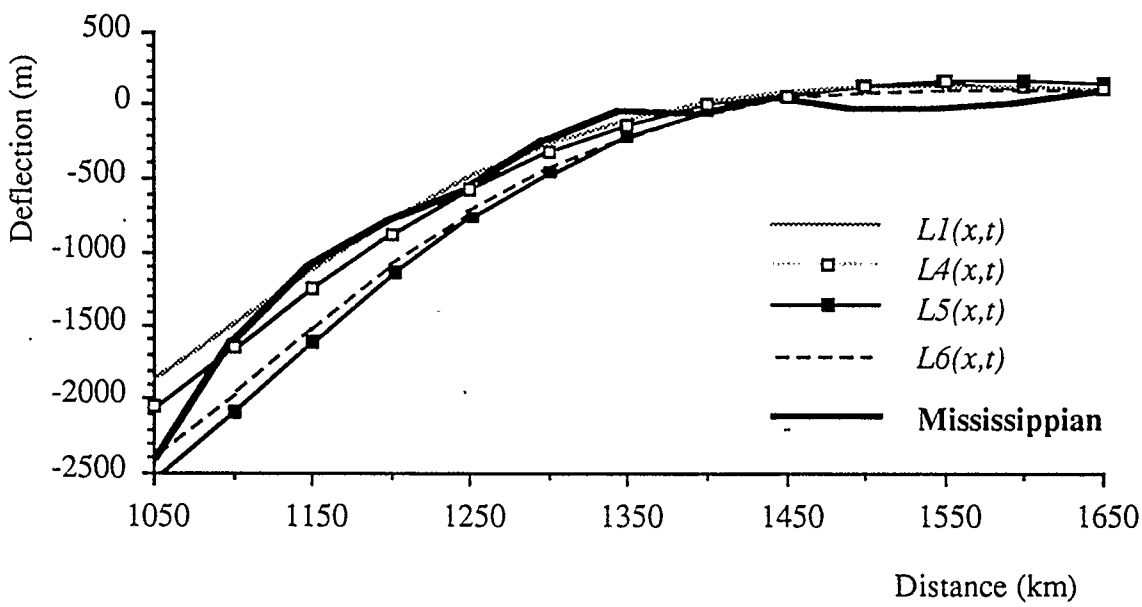

Figure 4.8.4. Deflection of the Mississippian for a uniform lithosphere of 100 km thickness and τ = 75 Ma using various load histories $L_1(x,t)$ (after Beaumont, 1981) and $L_4(x,t)$ through $L_6(x,t)$. Load 6 best matched the observed deflection of the Mississippian at the load edge.

Age (Ma BP) \ Load Column	1	2	3	4	5	6
140	2	Intermontane Superterrane				
130	2	Insular Superterrane				
110	2	1	1			
103	2	1	1			
100	2	3	3			
79	2	3	5	2		
72	2	3	5	2.25	0.25	
70	2	3	6	**6.25**	**3.75**	
65	2	3	6	**13.25**	**10.75**	**5.5**
35	2	3	4.5	**6.05**	**5.65**	**4.6**
15	2	3	2.9	**4.05**	**3.65**	**2.6**
0						

Time Step	Sediment
1	U Jurassic
2	110 Ma
3	Blairmore
4	L Colorado
5	U Colorado
6	Lea Park
7	Belly River
8	Edmonton
9	Paskapoo
10	Paskapoo
11	Paskapoo

Table 4.8.2. Load history 6 showing the total height of load (km) for each of the six load columns at different ages in time. The dashed line delineates the eastward advancing thrust sheets associated with different orogenic events while bold values represent changes from $L_1(x,t)$ in Table 4.5.1.

(c) Results of Improved Uniform Lithospheric Model:

The temporal deflection of the Mississippian was plotted at the Alberta-Saskatchewan border using the lithospheric model with d = 100 km, τ = 75 Ma and $L_6(x,t)$. Figure 4.8.5 shows that the deflection at the Alberta-Saskatchewan border, *i.e.* at x = 1500 km, was positive with respect to the original baseline at every time except between about 65 Ma and 28 Ma before present. The height of the peripheral

bulge was predicted to be as high as 150 m relative to the baseline at present time. Figure 4.8.6 shows that the peak of the peripheral bulge first migrated away from the load through time and then back towards the load stopping at present.

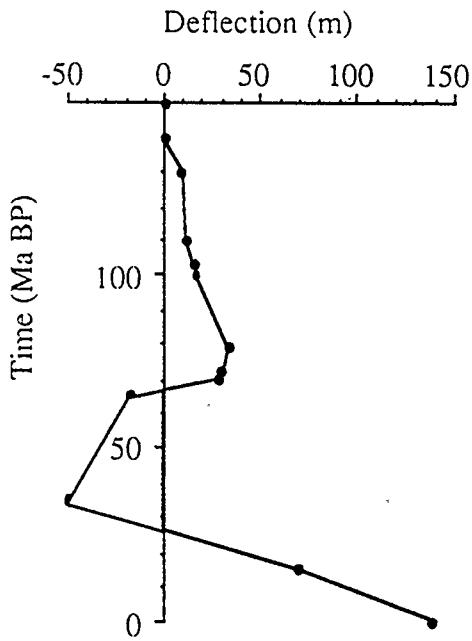

Figure 4.8.5. The deflection for a uniform 100 km thick lithosphere at x = 1500 km near the 4th Meridian using τ = 75 Ma and $L_6(x,t)$. The deflection indicates a positive deflection with respect to the fixed baseline at every time except where shaded between 65 Ma and 28 Ma.

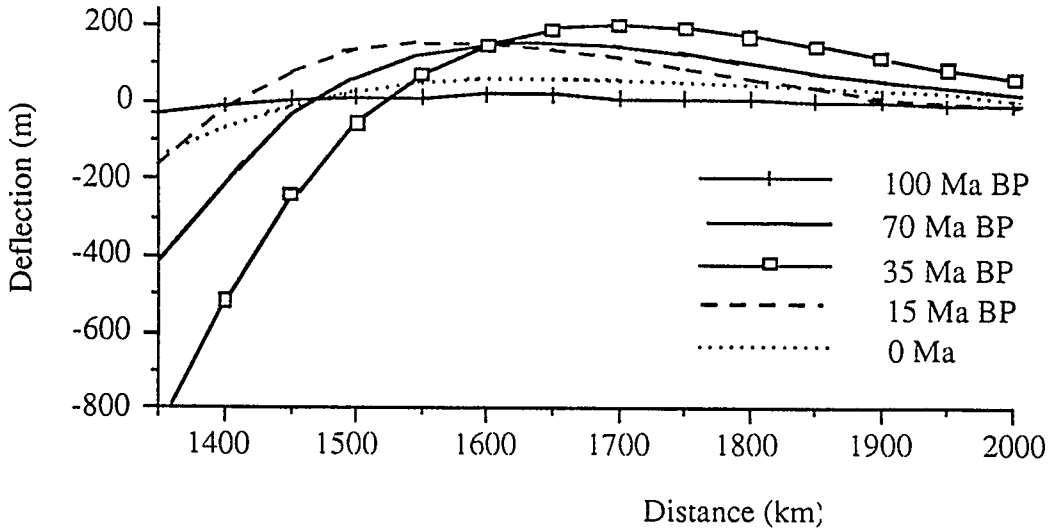

Figure 4.8.6. Migration of the peak arch during loading (solid lines) and unloading (dashed lines) around the Alberta-Saskatchewan border (x = 1550 km). The model was uniform, 100 km thick with τ = 75 Ma and using load history $L_6(x,t)$.

Figure 4.8.7 shows the final stratigraphy after the second-order sedimentation model was incorporated using the spreadsheet described in 4.6. The units in this model predict a present-day eastward dip on the Mississippian at $x > 1550$ km which is contrary to what is observed (Figure 4.2.2). It can be seen that using the new loading history $L_6(x,t)$ the stratigraphic units still crop out at the wrong location (the eastern limit of the Lea Park actually crops out about 40 km *west* of the Alberta-Saskatchewan border rather than 50 km *east* of it as in this model). It is also evident from this figure and the enlarged portion shown in Figure 4.8.8, that the basin is still too short since the peripheral bulge is at $x < 1650$ km. This must be true since the Blairmore unit was found to actually *thicken* as it dipped *eastwards* beyond $x = 1650$ km rather than thinning and subcropping at $x \approx 1650$ km as in Figure 4.3.3.

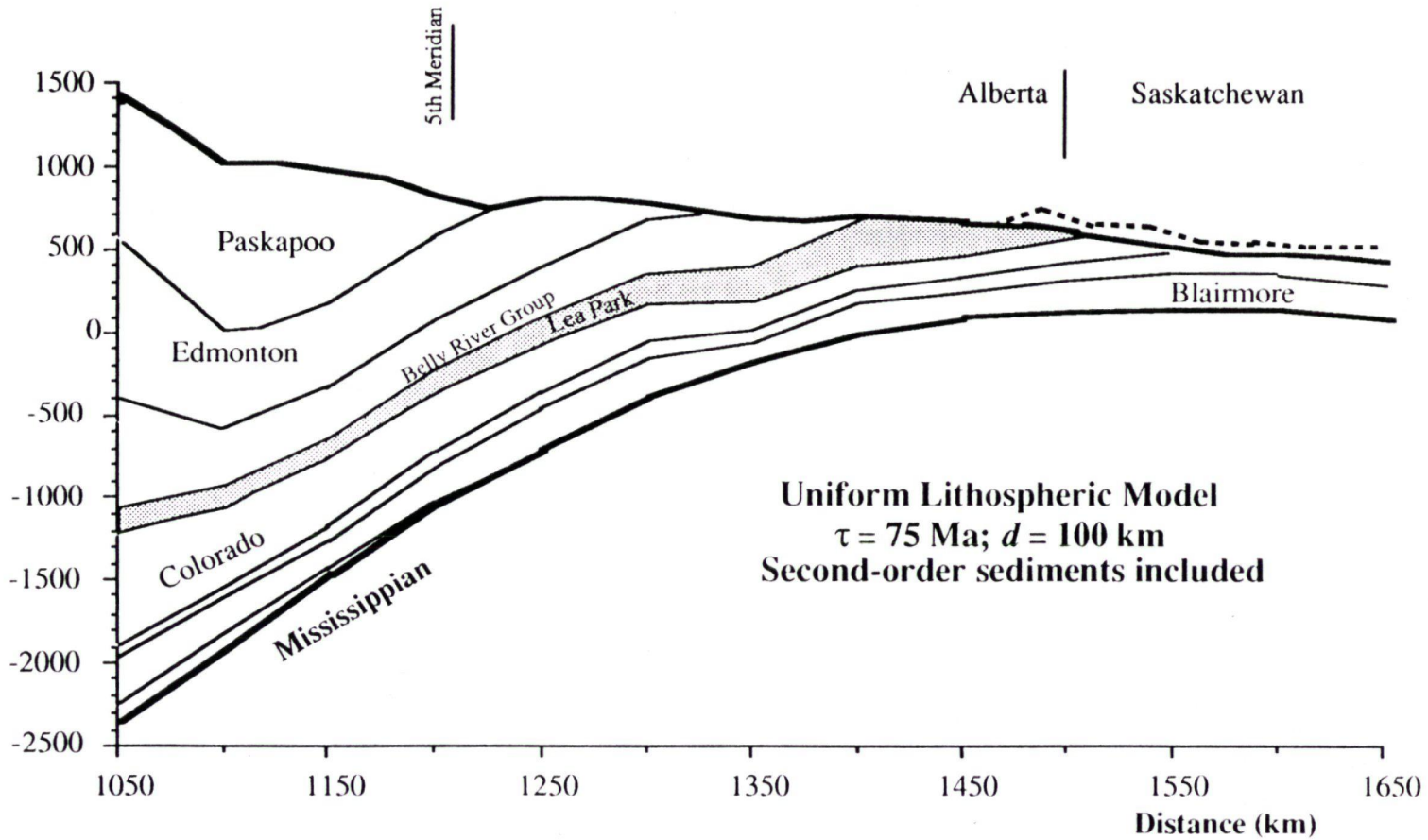

Figure 4.8.7. Our best model using a uniformly-thick lithosphere and modified load history. The units have approximately the correct thickness but the wrong shape. The outcrops are in the wrong location and the units incorrectly dip eastward at the Alberta-Saskatchewan border. The model does not spread the deformation of the foredeep out far enough. (*cf* Figure 4.3.3).

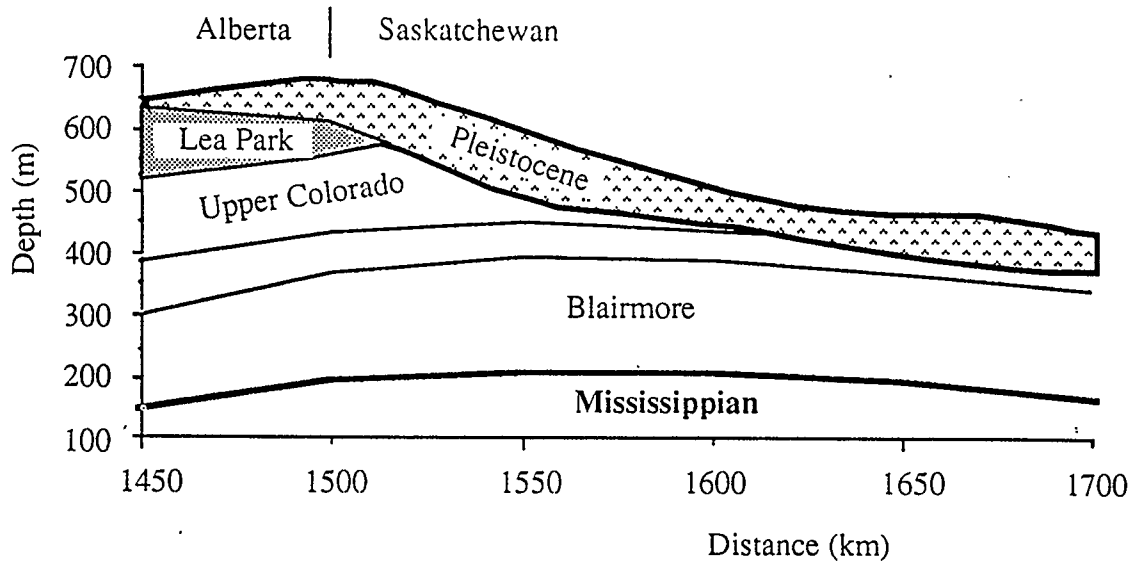

Figure 4.8.8. Enhanced view of the stratigraphy at the Alberta-Saskatchewan border predicted by using a uniform lithosphere 100 km thick with a relaxation time of 75 Ma. This model was rejected since the model forces the units to dip to the *east* at $x > 1550$ km.

In conclusion, it was found that a uniformly-thick lithospheric model that has the correct thickness for each formation, does not simultaneously have the correct dip direction east of the Alberta-Saskatchewan border and the correct outcrop location. From the searches in d and $L(x,t)$ space, it was shown that, by increasing the thickness of the uniform lithosphere, the deformation could be spread out further (thus eliminating the eastward dip in sediments) but with a resultant insufficient flexure at the load edge.

As proposed in section 4.2, an eastward thickening lithosphere (as shown in Figure 4.4.1 [Bottom]) was next used to model the Alberta Foreland Basin.

4.9 Eastward Stiffening Lithosphere

As discussed in section 4.2, the second aim of this chapter is to investigate whether an eastward *stiffening* lithosphere can fit the observations. The simplest model is to have an eastward thickening lithosphere with a constant slope m. This will spread the deformation away from the load while maintaining a reasonable deflection at the edge of the load. The model is shown in Figure 4.9.1 and it has a constant thickness on the west, and then linearly thickened towards the east. To the east, well into the interior

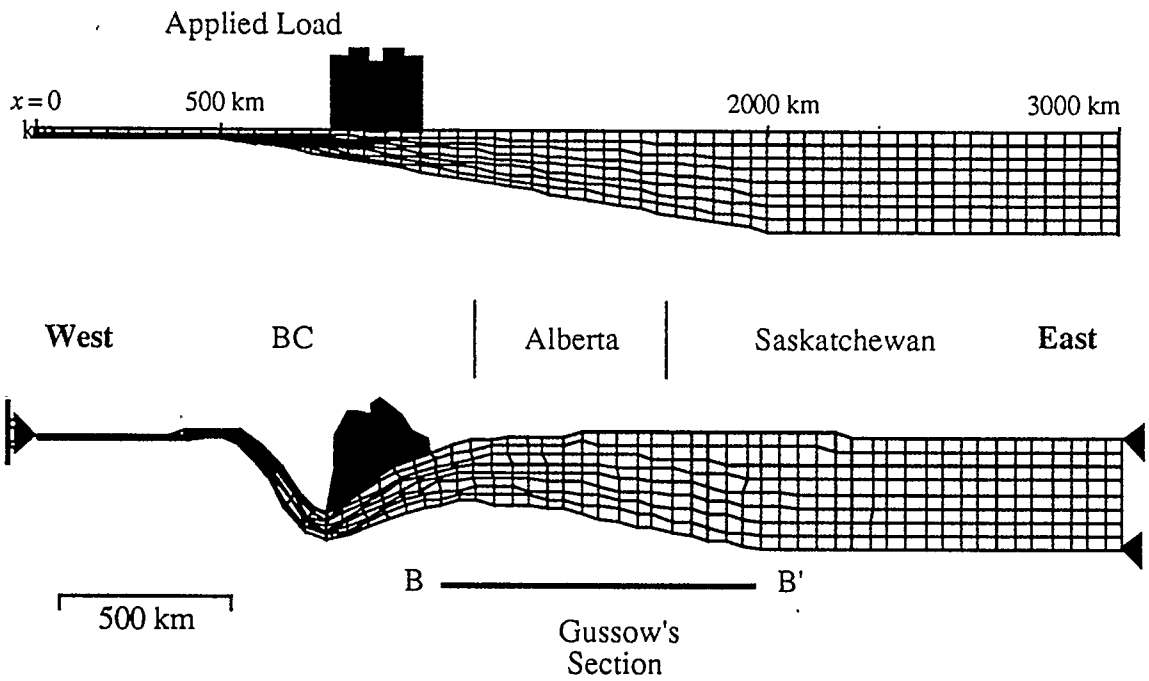

Figure 4.9.1. [Top] Finite element lithospheric model for the cratonic lithosphere beneath the west side of the North American Plate. The lithosphere is a viscoelastic continuum with a relaxation time of 75 Ma. [Bottom] Typical deformation for one load (no scale is inferred since deformation is very small when compared to the whole model).

of the craton, the lithospheric thickness was once again assumed to be constant (Figure 4.9.1 [Top]) since the thickness would otherwise be too great and the deflection is not strongly influenced by the thickness here. Figure 4.9.1 [Bottom] is a schematic showing a typical deformation of the lithosphere after the first loading time step. This has been exaggerated in the vertical direction by a scaling factor. In reality, the deflection is very small when compared to the dimensions of the lithosphere itself.

(a) Slope m Search:

A slope m search was therefore performed using values of τ = 75 Ma and $L_6(x,t)$ as for the improved uniform lithosphere. Figure 4.9.2 which is divided into [Top] and [Bottom] for clarity, shows the results of this slope search where the thickness of the lithosphere at x = 1050 km was fixed to be d = 100 km. Maintaining the thickness of the lithosphere at the load edge to be ≈100 km while using load history $L_6(x,t)$, ensured that the deflection at the edge of the load would be about 2400 m.

It was found that the m = 62 m km^{-1} and the m = 86 m km^{-1} models were not thick enough in the east and still produced a slight eastward dip beyond x = 1500 km. The models in Figure 4.9.2 [Bottom] do not show an eastward dip. However, the m = 189 m km^{-1} model thickened too rapidly and the deformation was too deep between 1150 < x < 1400 km. Both the m = 114 m km^{-1} and the m = 158 m km^{-1} models were in "good agreement" with the observed flexure of the Mississippian and hence considered to be *possible* lithospheric models.

Having determined an eastward thickening lithosphere which predicted a Mississippian having a good fit to the present-day observed Mississippian, a realistic sedimentation model was then added to the 114 m km^{-1} model to see whether the stratigraphy could be correctly matched.

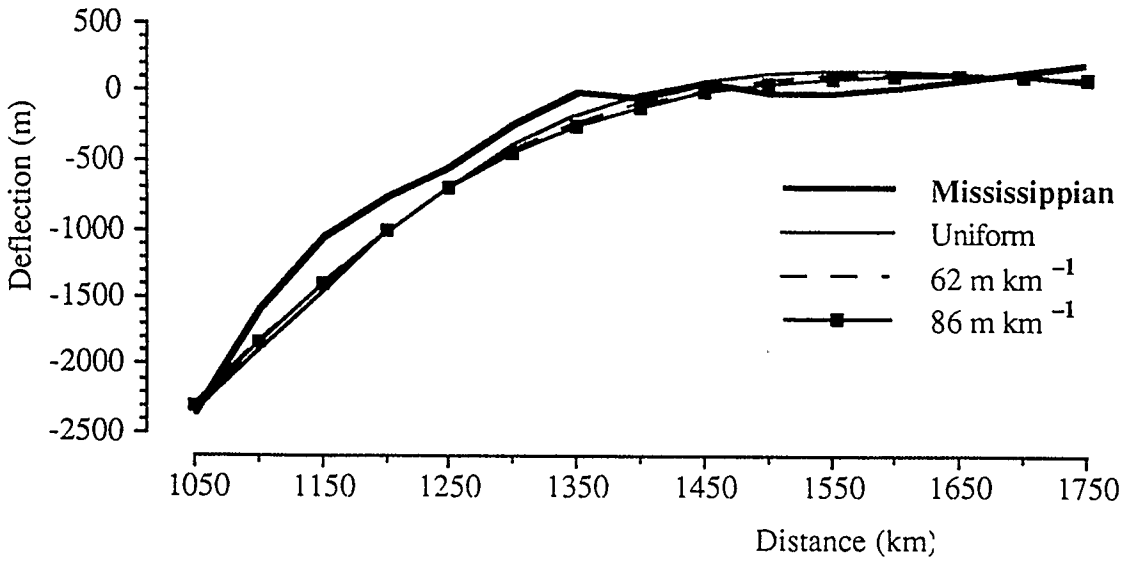

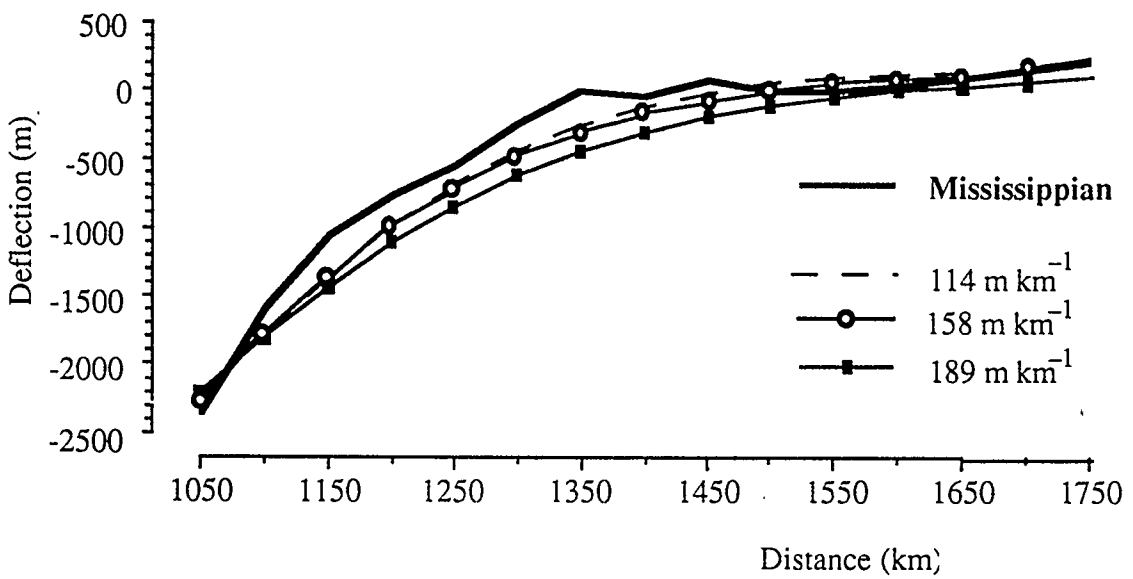

Figure 4.9.2. Models showing the effects of varying the slope m. The mean thickness of the lithosphere is 100 km at x = 1050 km (*i.e.* at the load edge). The uneven Mississippian was partially attributed to pre-existing topography. [Top] Results of two eastward thickening lithospheric models. [Bottom] Results of three lithospheric models using steeper slopes.

(b) Results of Laterally Varying Lithosphere:

The temporal flexure due to the laterally varying lithospheric model having a thickening slope of m = 114 m km^{-1} was plotted at three different locations, namely at the edge of the load (x = 1050 km); the 5th Meridian (x = 1200 km); and the Alberta-Saskatchewan border (x = 1500 km). Figure 4.9.3 shows the results of the lithospheric flexure through time at these sites along with the eustatic curve of Figure 4.6.1. The eustatic curve was plotted at the same scale to show the magnitude of its contribution in relation to the amount of flexure. The amount of space between the eustatic curve and the flexure curve is the amount of accommodation available for marine

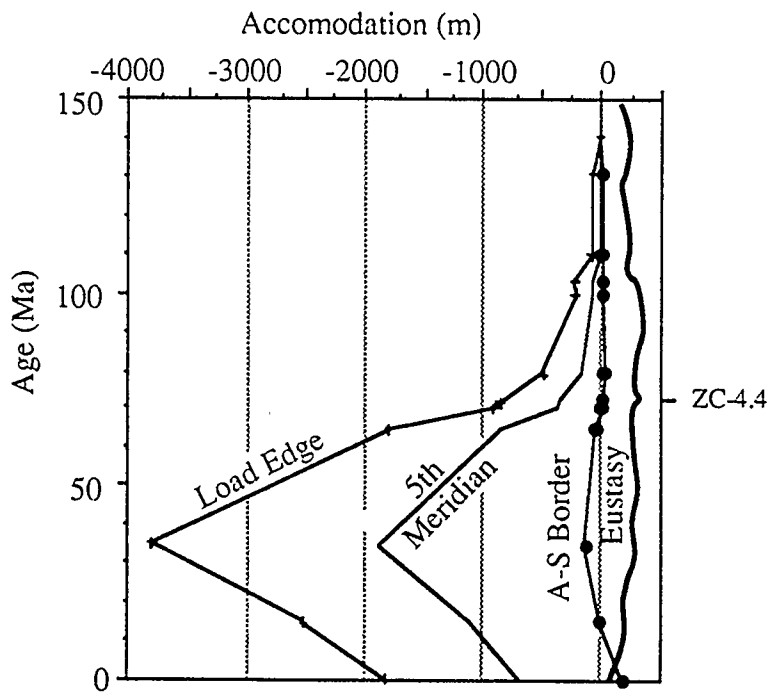

Figure 4.9.3. Accommodation control at three different locations. The amount of space between tectonic subsidence and eustatic changes in sea level represents the permitted amount of marine deposits for various times. Note that there is no peripheral bulge for the m = 114 m km^{-1} model at any time. The eustatic curve showing first-order variations is taken from Figure 4.6.1.

deposits. It can be seen that eustasy is especially important at the Alberta-Saskatchewan border throughout time since it is comparable to the amount of flexure that took place throughout time. Note also that at ≈ 72 Ma, the Zuni C-4.4 (second-order) cycle was included. The reason for including this will become clear later. The resulting stratigraphy was therefore inferred by combining the results of this flexural model with the depositional model as described in section 4.6. In this manner, the stratigraphy of the adjacent foreland basin was tied to the structure through the deformation of the lithosphere.

The process of gradually filling in the sediments through time was repeated until the present time was reached. Figures 4.9.4 (a-d) show the predicted basin evolution during the end of Kimmeridgian (140 Ma); end of Early Albian (103 Ma); end of Campanian (79 Ma); and the end of Early Maastrichtian times (72 Ma) respectively. At the time of initial thrusting, during the Jurassic, when the mountains were beginning to form, the Jurassic Kootenay and Fernie Formations were predicted to be deposited in a shallow marine environment extending as far as the middle of Saskatchewan (about x = 1750 km) and later were predicted to erode. The Early Albian was accompanied by a gradual relative sea level rise of about 35 m. Hence Blairmore sediments were predicted to be more distal with respect to the limit of thrusting and fill the foredeep as far as the Alberta-Saskatchewan border (Rudkin, 1964, chapter 11).

An intermittent high stand of relative sea level of around 195 m (with respect to present-day sea level) at ≈91·5 Ma is predicted to result in deep marine sediments such as the Viking Shale (Albian) and Lower Colorado to be deposited. Ignoring the short term eustatic changes, relative sea level fell steadily between 91·5 Ma and about 84 Ma. The continued deepening of the seaway brought in the Joli Fou, Viking and Lower Colorado Shale which are all marine deposits.

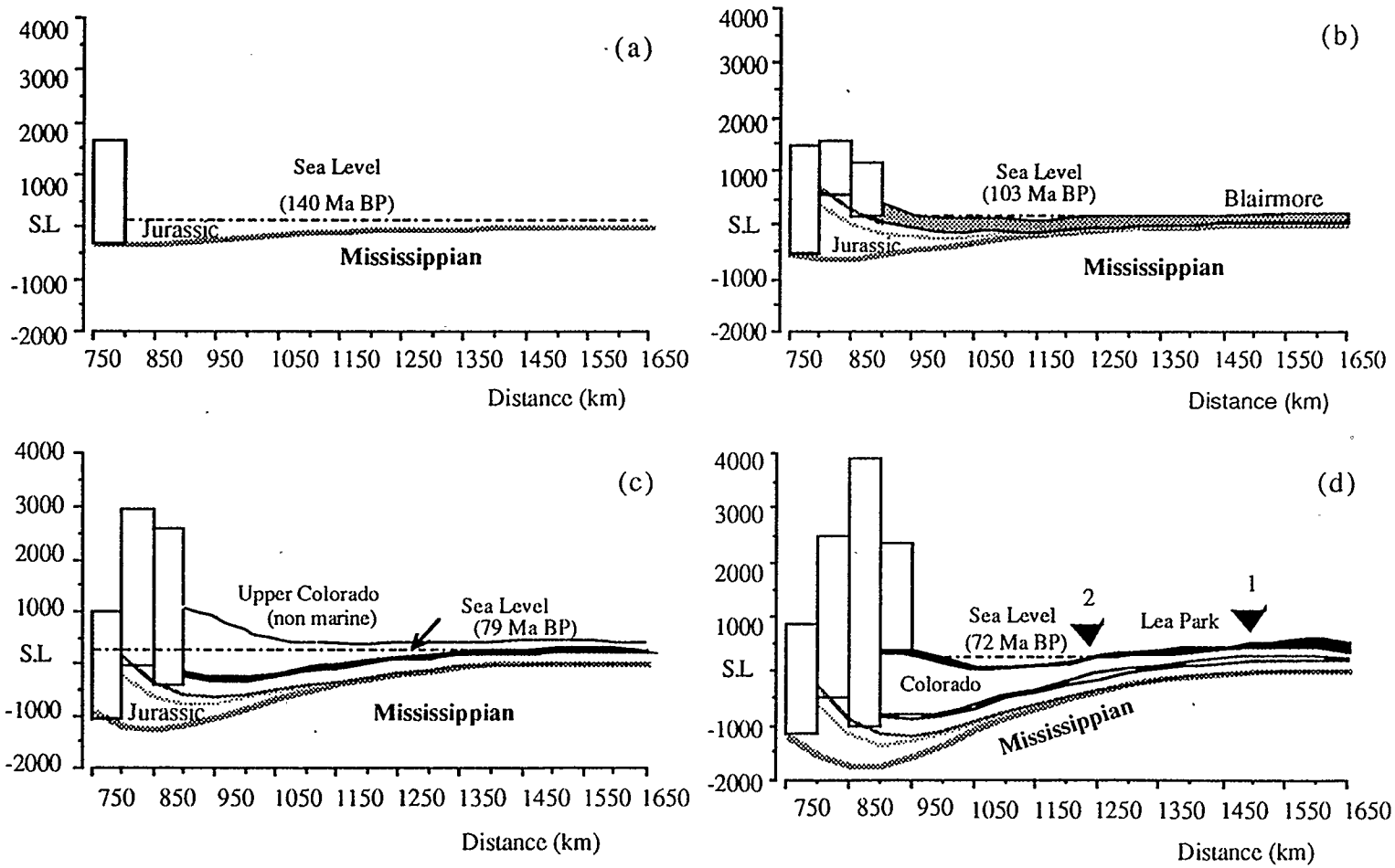

Figure 4.9.4 (a-d). From top left. Paleogeography during (a) Kimmerigian (b) Early Albian (c) Campanian and (d) Early Maastrichtian time. Note that the predicted non-marine Upper Colorado and the narrower marine fairway during the Lea Park both agree with observations. The load columns were taken from our loading history L6(x,t).

During Campanian (79 Ma), relative sea level had fallen. The effect of this was to drop the water depth by ≈ 250 m, a net gain of about 75 m with respect to Early Albian but nonetheless a relative drop with respect to Turonian (see Figure 4.9.4c). This time marked commencement of deposition of the Post Colorado Supergroup, which is dominantly non-marine near the Foothills. Towards the east however, this gives way to a marginal marine facies. The Lower Colorado is shown highlighted in this figure for clarity.

Finally, during the Maastrichtian, the last of our paleogeographic sections (Figure 4.9.3d) shows deposition of the Lea Park (highlighted in black) which is mainly marine. Note that Figure 4.9.4d predicts that the Lea Park is made up of an older shoreline denoted as 1 at about x = 1500 km and a younger one denoted as 2 at about x = 1250 km.

A high-stand of relative sea level produced a fluctuation of roughly 50 m lasting between 75 Ma and 71 Ma reaching a maximum at 73 Ma (cycle Zuni C-4.4). This is the only explanation for the older (raised) shoreline at 1500 km. The high-stand would have raised the sea level by 50 m in this short-order (2 Ma) cycle to result in a widening of the marine fairway. Then it would have dropped 50 m just as suddenly to the original, more proximal shoreline of the eastern basin margin. Introducing this second-order eustatic cycle was necessary to better approximate the present-day cross-section.

Also shown in the paleogeographic sections, are the respective predicted heights of the Rocky Mountain Fold and Thrust Belt as it evolved. These are shown as the total column of sediments and thrust sheet using a combined average density of 2400 kg m^{-3}. In the next section it will be shown that this process of mountain building will in fact result in a reasonable present-day mountain height.

Creating the depositional history step by step through time enabled us to reconstruct the present-day Alberta Foreland basin. The result of this best present-day model is shown in Figure 4.9.5 (for a direct comparison with the observations of 4.3.3). Figure

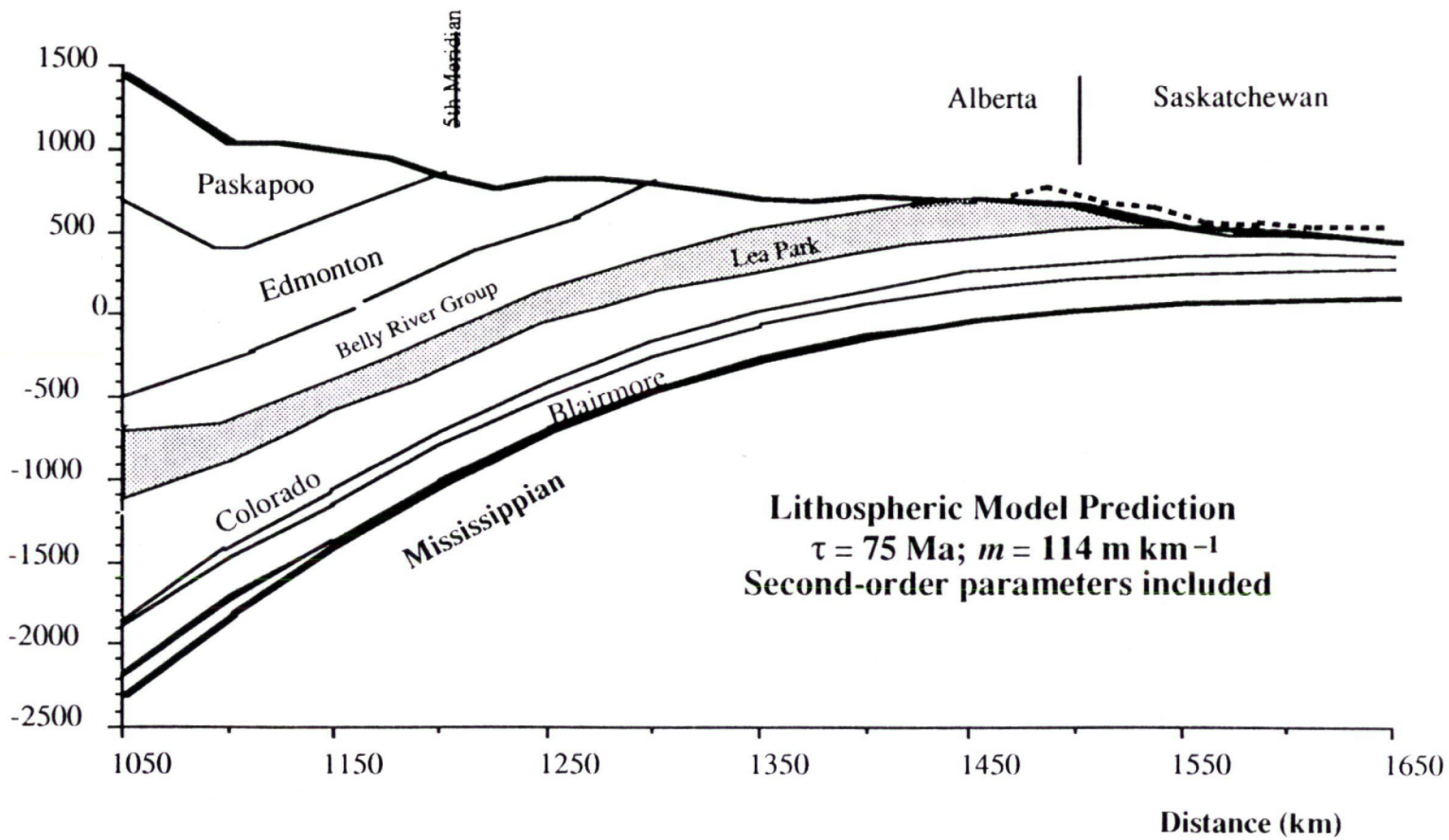

Figure 4.9.5. Our best model using an eastward thickening lithosphere with m = 114 m km^{-1}, τ = 75 Ma and load history 6. The units have the correct shape and thickness and outcrop in the right location. The peak of the peripheral bulge lies east of x = 1650 km. Notice that the emergence of the Lea Park at the Alberta-Saskatchewan border implies the correct basin extent (compare with Figure 4.3.3).

4.9.5 shows that the thickness of the units are approximately correct while simultaneously maintaining the correct dip and outcrop locations of these units. Notice that the peripheral bulge must be *east* of x = 1650 km since the Mississippian does not show evidence of any eastward dip. The Lea Park (shaded) emerges at the Alberta-Saskatchewan border implying the correct extent of the basin.

4.10 Rocky Mountain Height

In order to show that the load model $L_6(x,t)$ was entirely reasonable and that internal consistencies can be achieved with the lithospheric models, the predicted present-day heights of the mountains were then compared for both the uniformly-thick model (d = 100 km; τ = 75 Ma) and the eastward thickening lithospheric model (m = 114 m km^{-1}; τ = 75 Ma). The height of the tectonic load $L_6(x,t)$, given in Table 4.8.1, was added to the height of the sediment load assuming densities of both 2300 kg m^{-3} and 2400 kg m^{-3} in order to test the sensitivity of density variations. Figure 4.10.1 gives the predicted height of the Rocky Mountain Fold and Thrust Belt along BB'. The values for the heights in kilometres above sea level were found to be:

x =	*750*	*800*	*850*	*900*	*950*	*1000*	km
Load Column	1	2	3	4	5	6	
m = 114 m km^{-1}	0·84	1·59	1·02	2·68	2·53	2·52	(ρ = 2400)
model	0·93	1·65	1·04	2·69	2·55	2·54	(ρ = 2300)
Uniform	0·89	1·53	0·98	2·65	2·50	2·51	(ρ = 2400)
model	0·93	1·65	0·94	2·58	2·43	2·48	(ρ = 2300)

Another result of this analysis was an upper estimate of the volume of sediments that were deposited beneath the RMFTB in Belly River Group time and earlier (*i.e.* before

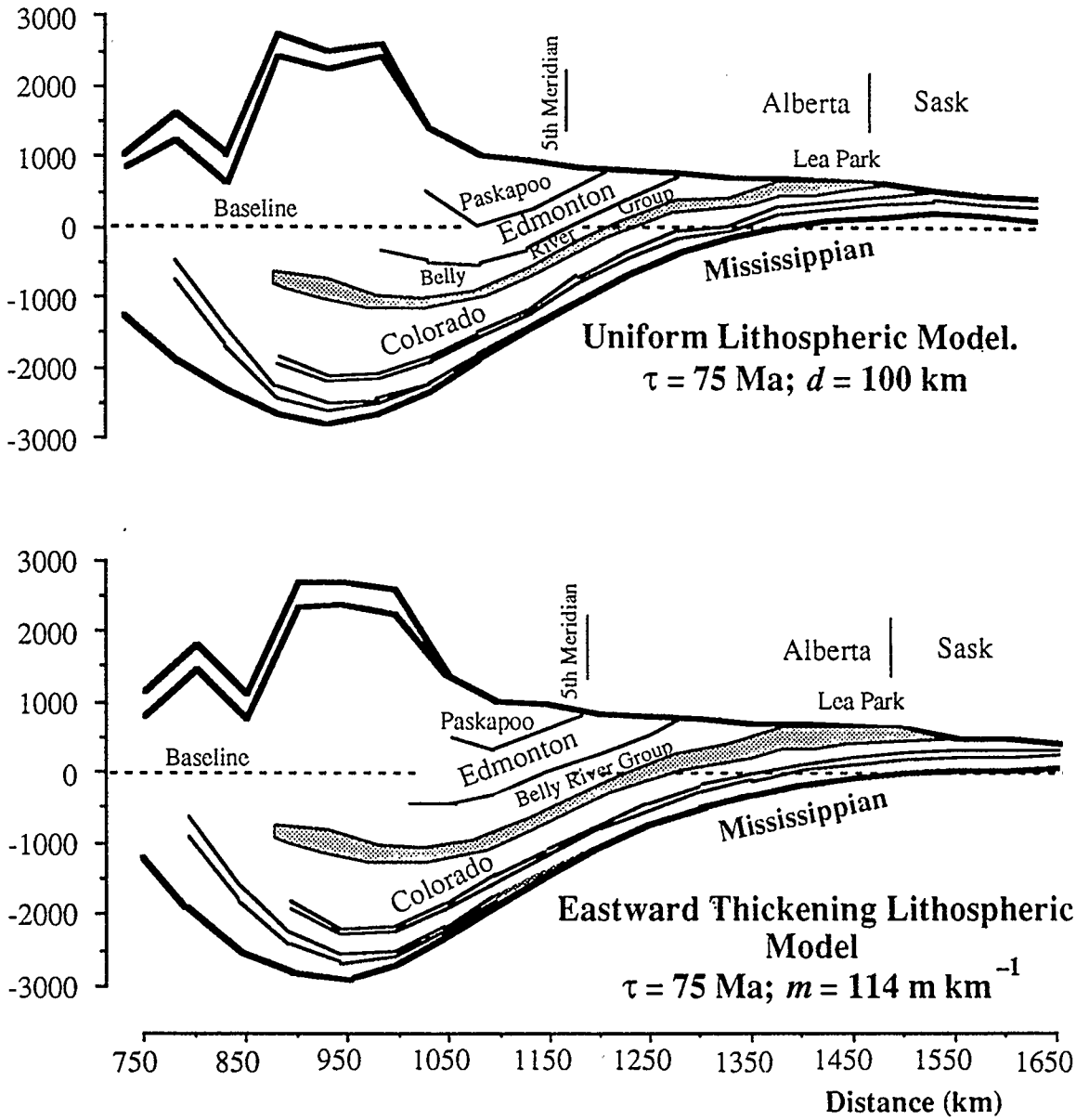

Figure 4.10.1. Mountain load showing the six load columns for $L_6(x,t)$ with densites of 2300 and 2400 kg m^{-3} and the topography produced by joining the mid-points of these load columns. The match with present-day observations was good except for a possible deficiency of ≈1·6 km of sediment in column 3 at x = 850 km. The Lea Park was deposited as far west as $x \approx$ 900 km (shaded).

72 Ma). Not many wells which penetrate these sediment depths (*i.e.* deeper than about 4000 m) are drilled beneath the Rocky Mountains and hence this prediction may be useful in showing how much sediment was likely to have been deposited. The volume of hydrocarbon source rocks that were deposited beneath the Rocky Mountains could then be calculated and, from this estimate, the volume of hydrocarbons yielded could be obtained. (The hydrocarbons that the source-prone rocks yielded would necessarily migrate updip towards the basin). This would give only order-of-magnitude estimates since the RMFTB is actually a series of duplex structures with thrust sheets of Mississippian and older rocks thrust near vertical to the surface.

In these two models, the base of the lithosphere is generally parallel to the modelled Mississippian (*i.e.* the original model baseline). It can be seen from Figure 4.10.1 that the profile of the deformed Mississippian is roughly reflected in the mountain height and erosional surface. Hence it could be argued that by adopting Airy's hypothesis of how isostatic compensation is maintained, the mountains and sediments are compensated by the buoyancy forces arising from the displaced mantle. Airy's hypothesis assumes a series of floating blocks each compensated by buoyancy. The situation is somewhat more complicated here since the stiffness of the lithosphere has to be taken into account too. It is therefore proposed that the depth of compensation of the lithospheric root may be better realized using this type of modelling rather than the simplified Airy hypothesis used in the past.

4.11 Lithospheric Modelling Conclusions

In this chapter, a comprehensive study of the characteristic properties of a cratonic lithosphere was made. The experimental site chosen, the Alberta Foreland Basin, had two distinct advantages: the first was that there is extremely good control in this well studied, mature basin and the second was that we were able to build on existing

work done by Beaumont (1981).

Fundamentally, the procedure incorporated three different inputs, namely the loading history of the Rocky Mountain Fold and Thrust Belt; the parameterized lithospheric model; and the depositional mechanism in the adjacent foredeep. In our procedure we assumed a loading history without assuming any *a priori* knowledge of the flexural model. We consequently predicted a suite of possible lithospheric models. Having determined possible lithospheric models based on the shape of the Mississippian, the next step was to apply a reasonable depositional style. This procedure allowed us to characterize the properties of the lithosphere while taking advantage of the finite element method.

Assuming a viscoelastic rheology, various lithospheric models were developed with some enhancements over Beaumont's (1981) best model. The finite element method was used in *lieu* of thin plate theory; a compressible lithosphere using $\nu = 0{\cdot}25$ was adopted; and the boundary conditions were greatly improved - particularly on the west end of the model, even though the effect of this boundary condition is small. A parameter search was used to systematically study the effects of varying the mean thickness d, relaxation time τ (and therefore viscosity), and the load history $L(x,t)$ for these models.

It was found that our best uniform lithospheric model with $d = 100$ km; $\tau = 75$ Ma and a loading history $L_6(x,t)$ matched the observations reasonably well between 1050 km < x < 1550 km. The units below the Belly River Formation however, still cropped out roughly 90 km too far west when compared to the observed data despite a lateral resolution of 50 km. Beyond $x > 1550$ km the units also showed an eastward dip which could only be removed by assuming an increasing eastward height in the Mississippian paleo-topography. Unless this increase in topography was strictly *east* of $x = 1500$ km, this assumption would push all the younger outcrops further west if the correct thicknesses of the units was maintained. This would mean the outcrop locations of the units would be pushed even *further* west which would result in a worse fit.

The effect of lateral variations in the thickness was then studied by varying the slope m. This model was used to parameterize a single viscoelastic layer with an effective relaxation time τ = 75 Ma (corresponding to an effective viscosity of $\approx 8\times10^{25}$ Pa s) which closely follows this depth profile. A lithospheric model that thickened from 37 km at x = 500 km to about 210 km at x = 2000 km (*i.e.* with a slope of 114 m km^{-1}) was found to best fit the observations. It was shown that by using a reasonable depositional history this model was able to better match current-day observations. The location of the outcrops as well as the dip and thicknesses of the units were in good agreement with observations.

In conclusion, an eastward thickening lithosphere can match the present-day observations of the Alberta Foreland Basin. The eastward thickening lithospheric models also seemed to work better (*i.e.* with fewer assumptions) than the uniform lithospheric models. The two eastward thickening lithospheric models with m = 114 m km^{-1} and 158 m km^{-1} were found to fit the Mississippian data. If the lithosphere thickens

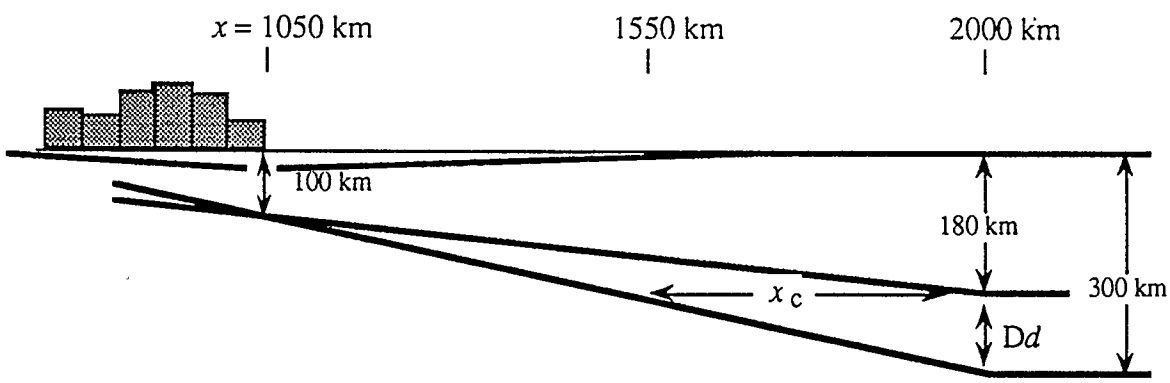

Figure 4.11.1. Sensitivity of the eastward thickening lithospheric models showing the critical distance x_c of thickening and the limits of this thickness with all other parameters constant. The thickest part of the lithosphere is 180 km < d < 300 km with this thickness occurring between 1500 km < x < 2000 km.

linearly eastwards with these slopes then a cratonic lithosphere ranging between 300 km < d < 180 km in thickness must exist beneath the North American Craton starting somewhere between 1500 km ≤ x ≤ 2000 km. This lateral variation in the thickness of the lithosphere having an effective viscosity of 8×10^{25} Pa s implies a deep and cold root below the North American Cratonic plate that penetrates down into the mantle.

North of this line of section BB' lies the Peace River Arch and south of BB' lies the Sweetgrass Arch. At these locations the applied load is different and there is also interference in the Sweetgrass Arch caused by Williston Basin. Hence it should be emphasised that the line of section chosen lies in the undisturbed portion of the craton.

"We cannot direct the wind
but we can adjust the sails"

Anonymous (1990).

5. Discussion and Conclusions

The main thrust of the work done in this study can be divided into two distinct parts. In chapters 2 and 3, the finite element method was compared with simple theoretical continuum mechanical models. It was found that the results compared well with theory. The numerical errors introduced were generally found to be smaller than the geophysical measurement being made. The advantages of the finite element models were that thin plate theory was not assumed and that the models did not neccessarily require uniform lateral properties. In the second part, in chapter 4, several Maxwell-type viscoelastic models were considered for the deformation of a cratonic lithosphere. The Alberta Foreland Basin was used for our model of a typical cratonic lithosphere.

The result of this modelling in chapter 4 shows that cratonic lithospheres having cold deep roots extending to depths greater than 200 km can satisfy the observations. This finding is also corroborated by the seismic and chemical evidence presented in section 4.2. Three-dimensional inversion of surface waves data by Woodhouse and Dziewonski (1984) generally show high velocity perturbations in surface waves travelling beneath shields. The difference in velocities is mainly attributed to the temperature differences between continental and oceanic lithospheres. The chemical composition of colder continental lithospheres also affect velocity and thus propagate surface waves at relatively higher velocities. Upon closer inspection of depth slices of their models M84A and M84C, it was found that the deep cold roots do not extend straight down but rather are offset with increasing depth. The direction of offset at depth corresponds with the direction of movement of the plates.

One implication of this present study therefore, was to postulate a model where continental plates actually *sit* on the denser uppermost mantle. The thick, cold roots of the continental plates are dragged through the asthenosphere and lower mantle as

shown in Figure 5.1.1. This may account for the fact that plates with continents move

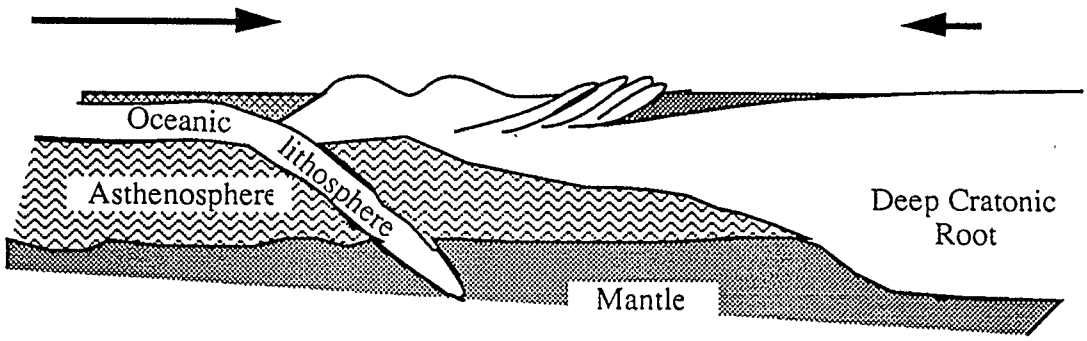

Figure 5.1.1. Schematic of the proposed plate tectonic model showing cratonic lithospheres as they are dragged through the upper mantle while the oceanic lithospheres float on the asthenosphere. Velocities of plates bearing continents are impeded from moving as fast as younger (and thinner) oceanic lithospheres.

at much lower speeds than oceanic plates (with the exception of the Indian Plate). The observation which regards continental lithospheres as a thick plate imbedded within the mantle and the relatively high speed of the Indian Plate warrants further work.

Throughout the evolution of this work, several interesting diversions were encountered and as a result some ideas for important future work were identified. Further work in geodynamics that takes advantage of the finite element formulation could involve several themes such as using the finite element method to:

(i) Investigate the effects of lateral temperature and chemical variations in a uniformly-thick viscoelastic layer overlying a fluid upper mantle. This would be a natural extension of the present work and would not require our assumption that

relates the thickness of the lithosphere to the viscosity profile of the lithosphere.

(ii) Model a stratified lithosphere consisting of an elastic upper lithosphere ($\tau = \infty$) overlying an increasingly less viscous lithosphere with depth. This model is more realistic and does not require the introduction of an *effective* viscosity or relaxation time. This type of a model would be applicable to loads having different characteristic wavelengths since the load would "see" the appropriate depth.

(iii) Include the effects of non-linear rheology in the lithosphere and upper mantle since deformation of rocks in the lithosphere and mantle are better described by a power-law creep. An implication of these types of models would be to have a lithospheric model that is applicable to any load period.

These suggestions for future work are all conducive to using the finite element method since both heat flow and multi-layering can be modelled without much extra effort or any modification to the software. From our dimensional analysis however, it was also found that, for larger loads, the advection of pre-stress and the perturbation due to gravity become increasingly important. Therefore, in order to use the finite element method for such large-scale Earth loads ($\lambda \gg 1000$ km), these additional terms must be incorporated into the finite element code. Hence, it is proposed that the finite element code could be re-written to include these two terms. Finite element codes are traditionally written by engineers where these terms are not necessary and hence they are not included in generic market software.

References

Aubouin, J. (1965). Geosynclines, *Elsevier Press*, New York.

Bally, A.W., P.L. Gordy and G.A. Stewart (1966). Structure, Seismic data, and Orogenic Evolution of the Southern Canadian Rocky Mountains, *Bull. Can. Pet. Geology*, **14**, pp 337-381.

Beaumont, C. (1981). Foreland Basins, *Geophys. J. R. astr. Soc*, **65**, pp 291-329.

Bills, B.G. (1983). Thermoelastic Bending of the Lithosphere: Implications for Basin Subsidence, *Geophys. J. R. astr. Soc.*, **75**, pp 169-200.

Boussinesq, J. (1885). Applications des Potentiels à l'Étude de l'Équilibre et du Mouvement des Solides Élastiques, **508**, Gautier-Villars, Paris.

Braun, J. and C. Beaumont (1990). Contrasting Styles of Lithospheric Extension: Implications for Differences Between the Basin and Range Province and Rifted Continental Margins, *in* Extensional Tectonics and Stratigraphy of the North Atlantic Margins, edited by A.J. Tankard and H.R. Balkwill, *AAPG Mem 46*.

Brotchie, J.F. and R. Sylvester (1969). On Crustal Flexure, *J. Geophys. Res.*, **74**, pp 5240-5252.

Cant D.J. and G.S. Stockmal (1989). The Alberta Foreland Basin: Relationship Between Stratigraphy and Cordilleran Terrane-Accretion Events, *Can. J. Earth Sci.*, **26**, pp 1964-1965.

Cathles, L.M. (1975). The Viscosity of the Earth's Mantle, *Princeton University Press*, Princeton, New Jersey.

Dickinson, W.R. (1976). Sedimentary Basins Developed during Evolution of Mesozoic-Cenozoic Arctrench System in Western North America, *Can J. Earth Sci.*, **13**, pp 1268-1287.

Farrell, W.E. (1972). Determination of the Earth by Surface Loads, *Rev. Geophys. Space Phys.*, **10**, No 3, pp 763-797.

Fulton, R.J. and R.I. Walcott (1975) Lithospheric Flexure as shown by Deformation of Glacial Lake Shorelines in Southern British Columbia, *Geol Soc Amer.*, **142**.

Garner, D.L. and D.L. Turcotte (1984). The Thermal and Mechanical Evolution of the Andarko Basin, *Tectonophysics,* **107**, pp 1-24.

Gussow, W.C. (1962). Regional Geological Cross-section of the Western Canada Sedimentary Cover, *Alberta Soc. Petrol. Geol.*, Calgary, Alberta.

Haq, B.U., J. Hardenbol and P. R. Vail (1987). Mesozoic-Cenozoic Chronostratigraphic Chart, *Science*, vol 235, pp 1156-1167 .

Jordan, T.H. (1978). Composition and Development of the Continental Tectosphere, *Nature*, **vol.** 274, no. 5671, pp 544-548

Jordan, T.H. (1981). Continents as a Chemical Boundary Layer, *Phil. Trans. R. Soc. Lond.*, **A301**, pp 359-373

Kerr, A.D. (1964). Elastic and Viscoelastic Foundation Models, *J. appl. Mech.*, **31**, pp. 491-498

Lamb, H. (1902). On Boussinesq's Problem, *Proceedings* at a meeting held on Feb. 13th, 1902

Lambeck, K and S.M. Nakiboglu (1980). Seamount Loading and Stress in the Ocean Lithosphere, *J. Geophys. Res.*, **85**, no. B11, pp 6403-6418.

McNutt, M.K. and H.W. Menard (1982). Constraints on Yield Strength in the Oceanic Lithosphere Derived From Observations of Flexure, *Geophys. J. R astr. Soc.*, **71**(2), pp 363-394.

Meijer Drees, N.C. (1986). Evaporitic Deposits of Western Canada, *Geological. Survey of Canada*, **85-20**

Nicholls, J., M.Z. Stout, D.W. Fiesinger (1982). Petrologic Variations in Quaternary Volcanic Rocks, British Columbia, and the Nature of the Underlying Upper Mantle, *Contrib Mineral Petrol*, **79**, pp 201-218

Owens, T.J. (1983). Normal Faulting and Flexure in an Elastic Perfectly Plastic Plate, *Tectonophysics,* **93**, pp 129-150.

Park, M.J.M. and G.K. Westbrook (1983). Visco-elastic Modelling of the Lithospheric Sresses Arising from Density Contrasts, *Geophys. J. R. astr. Soc.,* **74**, pp 905-914.

Passey, Q.R. (1981). Upper Mantle Viscosity Derived From the Difference in Rebound of the Provo and Bonneville Shorelines: Lake Bonneville Basin, Utah, *J. Geophys Res.*, **86**, no. B12, pp 11701-11708.

Peltier, W.R. (1974). The Impulse Response of a Maxwell Earth, *Rev.Geophys. Space*

Phys., **12**, no. 4, pp 649-669.

Peltier, W.R. (1983). Constraint on Deep Mantle Viscosity from Lageos Acceleration Data, *Nature*, **304**, pp 434-436.

Peltier, W.R., P. Wu and D.A. Yuen (1981). The Viscosities of the Earth's Mantle, Reprinted from *Geodynamic Series*, **vol 4**. American Geophysical Union

Price, R.A. (1973). Large-Scale Gravitational Flow of Supra-Crustal Rocks, Southern Canadian Rockies, in Gravity and Tectonics, edited by: De Jong, K.A. and Scholten, R.A., pp 491-502.

Price, R.A. and E.W. Mountjoy (1970). The Cordilleran Foreland Thrust and Folded Belt in the Southern Canadian Rockies, *Geol. Soc. Am.* , **vol**. 3, no. 6, pp 404-405.

Ranalli, G. (1987). Rheology of the Earth: Deformation and Flow Processes in Geophysics and Geodynamics, *Allen and Unwin Inc.*, Boston.

Rudkin, R. A. (1964). Geological History of Western Canada, in Lower Cretaceous, chapter 11, edited by: R.G. McCrossan and P. Glaister, *Alberta Soc. of Petrol. Geol.*, Calgary.

Silver, P.G. and W.W. Chan (1988). Implications for Continental Structure and Evolution from Seismic Anisotropy, *Nature*, **335**, pp 34-39.

Sipkin, S.A. and T.H. Jordan (1980). Multiple ScS Traveltimes in the Western Pacific; Implications for Mantle Heterogeneity, *J Geophys. Res.* , vol **85**, no B2, pp 853-861.

Stephenson, R. (1984). Flexural Models of the Continental Lithosphere Based on the Long-term Erosional Decay of Topography, *Geophys. J. R. astr. Soc.*, **77**, pp 385-413.

Turcotte, D.L. and E.R. Oxburgh (1967). Finite Amplitude Convection Cells and Continental Drift, *J. Fluid Mech.*, **28**, pp 24-42.

Turcotte, D.L. and G. Schubert (1981). Geodynamics: Applications of Continuum Physics to Geological Problems, *John Wiley & Sons*, Toronto.

Walcott, R.J. (1970). Flexural Rigidity, Thickness, and Viscosity of the Lithosphere, *J. Geophys. Res.*, **75**, pp 3941-3954.

Wolf, D. (1985). On Boussinesq's Problem for a Maxwell Continua Subject to an External Gravity Field, *Geophys. J. R. astr. Soc*, **80**, pp 275-279.

Woodhouse, J.H. and A.M. Dziewonski (1984). Mapping the Upper Mantle: Three-

Dimensional Modeling of Earth Structure by Inversion of Seismic Waveforms, *J. Geophys. Res.*, **89**, no. B7, pp 5953-5986.

Wu, P. (1978). The Response of a Maxwell Earth to Applied Surface Mass Loads: Glacial Isostatic Adjustment, M.Sc. Thesis, *University of Toronto*, Toronto, Ontario.

Wu, P. and W.R. Peltier (1982). Viscous Gravitational Relaxation, *Geophys. J. R. astr. Soc.*, **70**, pp 435-486.

Wu, P. and W.R. Peltier (1983). Glacial Isostatic Adjustment and the Free Air Gravity Anomaly as a Constraint on Deep Mantle Viscosity, *Geophys. J. R. astr. Soc.*, **74**, pp 377-449.

Wu, P. and W.R. Peltier (1984). Pleistocene Deglaciation and the Earth's Rotation: A New Analysis, *Geophys. J. R. astr. Soc.*, **76**, pp 753-791.

Zienkiewicz, O.C. (1975). Methode der finiten Elemente, 496 S., 214 Abb.; *München*, Wien (Hanser)

Index